An overlooked aquifer in the Netherlands: geothermal potential of the Breda Formation in the Zuiderzee Low

MSc thesis in Geo-Energy Engineering

Freek Smit

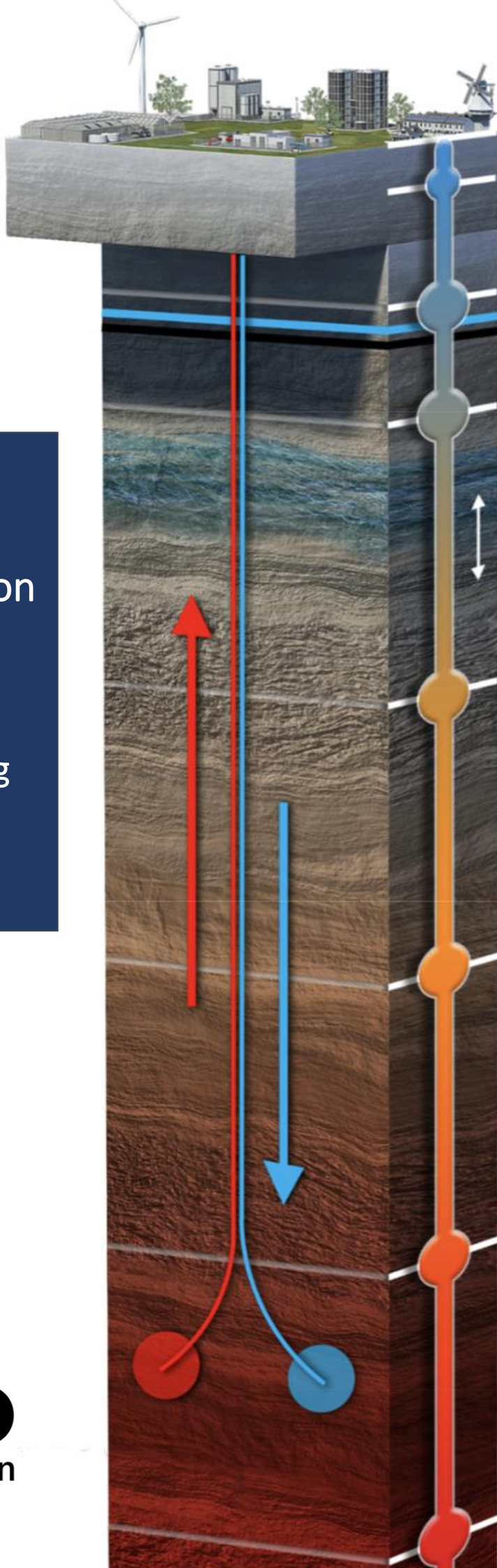

TU Delft
Delft University of Technology

TNO
innovation
for life

An overlooked aquifer in the Netherlands: geothermal potential of the Breda Formation in the Zuiderzee Low

Reservoir characterization, dynamic simulation and legislation in a medium deep aquifer

MSc thesis in Geo-Energy Engineering

by

F.J.J. (Freek) Smit

In partial fulfilment of the requirements for the degree of

Master of Science
In Geo-Energy Engineering

at the Delft University of Technology

This thesis was done in collaboration with the WarmingUP project at TNO

A digital version of this thesis is available at repository TU Delft

Date 15 September, 2022

Thesis committee	Dr. Phil Vardon (Chair)	Supervisor, Delft University of Technology
	Prof. Dr. David Bruhn	Supervisor, Delft University of Technology
	Drs. Hans Veldkamp	Supervisor, TNO
	Dr. Lies Peters	Supervisor, TNO

Abstract

Geothermal energy in the Netherlands is growing in general, however, medium deep geothermal (200 - 1500 m depth) is lagging behind while the potential at these depths could be very high. Development is held back by little geologic knowledge of this interval as well as legislative constraints. Better understanding of the reservoir characteristics and well design in this depth range is necessary in order to accelerate the heat transition away from fossil fuels. The Breda Formation is deemed as one of the most promising formations within the medium depth range. Therefore, this formation, particularly the part found in the Zuiderzee Low (ZZL), is the focus point of this thesis. The reservoir characteristics are determined using newly obtained cutting information, novel biostratigraphic analyses, old and new seismic interpretations and petrophysical log data, eventually leading to a static reservoir model. Consequently, the static model is upscaled and used as input for dynamic simulations in the Harderwijk case study area. The static model provides new thickness, depth, porosity, permeability and transmissivity maps of the Breda Formation in the ZZL. These maps were generated using more data (types) than the current ones present in the REGIS model, and should therefore contain less uncertainty. The dynamic model provides insights into doublet lifetimes and flow rates for three different well trajectories in two possible reservoir scenarios. The horizontal trajectory proved superior in terms of doublet lifetime and flow rate for both reservoir scenarios. Finally, the current Dutch legislative framework covering the medium depth is limiting medium deep geothermal development in the Netherlands. A revision of the 500 m depth boundary separating the Mining and Water Law jurisdictions should be considered if the full potential of the medium depth is to be accessed.

Preface

"Medium deep geothermal has a large potential, but almost nobody bothered to really look at it." This is roughly what my professors told me before the start of my thesis project, almost a year ago in November 2021. At the time I was looking for a thesis subject within the geothermal research field, to complete the master Geo-Energy Engineering at the TU Delft. Ever since I learned about the DAP project I became fascinated by the geothermal subject and I knew I wanted to write my thesis on it. I was immediately excited by the idea of exploring a completely new area, which has always been there, but never before taken serious. I was thrown in the deep, since there haven't been many publications on the subject. I enjoyed the challenge however. Still, I could use some help and luckily for me, Hans and Lies from TNO Utrecht agreed to take me on as an intern.

I wrote this thesis in collaboration with TNO within the WarmingUP[1] project, at the department of Applied Geosciences (AGS) in Utrecht. Here I got full support from Hans Veldkamp, Lies Peters, Sander Houben and everyone within the Geothermal Team and many more in the department of AGS. They made me feel right at home from the start of my internship. I would like to thank all of them for the tremendous help during this project and for the good conversations at the office, coffee corner or during lunch. Special thanks to Hans and Lies, who helped me on a day to day basis, whom I could bother even with the smallest of questions. Also thanks to Sander, who took me on several rides to Zeist to look, feel and taste ancient mud in the Core Sample Storage.

Furthermore, I would like to thank Phil Vardon and David Bruhn, who stood by me from the beginning until the end of this project. Thank you for your advise, council, kind words and critics, since without it I wouldn't have been able to make this thesis a success. Finally, I want to thank my family and friends, who were always there for me during the highs and lows. I enjoyed writing this thesis, and I also hope you enjoy reading it.

Freek Smit
Rotterdam, September 7, 2022

[1]This project is part of the innovation plan WarmingUP. WarmingUP is realized thanks to subsidies from the Rijksdienst voor Ondernemend Nederland (RVO) under the subsidy scheme 'Meerjarig Missiegedreven Innovatie Programma's (MMIP)', with project number TEUE819001

Contents

List of Figures

List of Tables

Acronyms

BOP Blowout Preventer. 4, 95

EMU Early Miocene Unconformity. 12, 25, 26, 41, 43, 62, 64, 90
ESP Electric Submersible Pump. 72, 82

GR Gamma Ray. 23, 28, 29, 31, 62, 64, 68, 82, 94
GRV Gross Rock Volume. 40

HTS High Temperature Storage. 3

LMU Late Miocene Unconformity. 12, 16, 25, 26, 41, 43, 62, 64, 91
LTC Logging Through Casing. 29
LZT Lauwerszee Trough. 10, 11, 93

MD Measured Depth. v, 20, 21, 23, 43, 64, 75
MMU Mid-Miocene Unconformity. 12, 20, 25, 26, 43, 62, 64, 68, 91
MWD Measurement While Drilling. 29

NLOG Netherlands Oil and Gas Portal. 6, 15, 16, 19, 25, 32, 33
NSB North Sea Basin. 10

RVG Ruhr Valley Graben. 10–12, 15

TVD True Vertical Depth. 5, 69, 70, 72, 75, 89, 90

UTES Underground Thermal Energy Storage. 1

VT Voorne Trough. 10, 11

XRD X-Ray Diffraction. 62

ZZL Zuiderzee Low. 10, 11, 14, 15, 17, 19, 20, 23, 25, 28, 29, 34, 38, 41, 60, 61, 63, 65, 66, 68–70, 85, 89, 90, 92–94

Chapter 1

Introduction

1.1 General background

Geothermal energy originates from heat coming out of the subsurface. In general, the temperature in the subsurface rises with roughly 3 °C per 100 m in the Netherlands. This geothermal gradient is induced by heat radiating out from the Earth's core. Water is situated in subsurface aquifers which is heated by the hot rocks. This water can be produced by drilling wells into the aquifer. The hot water is brought up via the production well. Once at the surface, the heat can be extracted from the water and used for heating (green)houses or in industrial processes. After extracting the heat, the cooled water is reinjected back via a second well into the same aquifer from whence it came. Here the water is reheated by the rocks before being produced again. This system of one producer and one injector well is called a doublet.

The geothermal energy industry in the Netherlands has been growing in recent years. Where in 2020 there were 24 operating geothermal doublets and 40 more in development, in 2021 this increased to 31 operating doublets and 70 more projects in development (Geothermie NL, 2022). From these, only the Zevenbergen and Mijnwater Heerlen project extract hot water from relatively shallow formations. 'Shallow formations' in this sense are regarded as formations situated roughly between 200 to 1500 m depth, with corresponding reservoir temperatures between 15 and 65 ^{o}C. Since using the word 'shallow' could be confusing with respect to Underground Thermal Energy Storage (UTES) applications, and 'deep' could refer to conventional geothermal, the term 'medium deep' or 'medium depth' is adopted from now on to refer to the 200 to 1500 m depth interval.

Medium deep geothermal has a large potential, as shown in Figure 1.1. Still, this heat source has largely been overlooked up until now. In light of the current climate change and the geopolitical situation surrounding fossil fuels, medium deep geothermal development could provide much needed impulses to accelerate the heat transition.

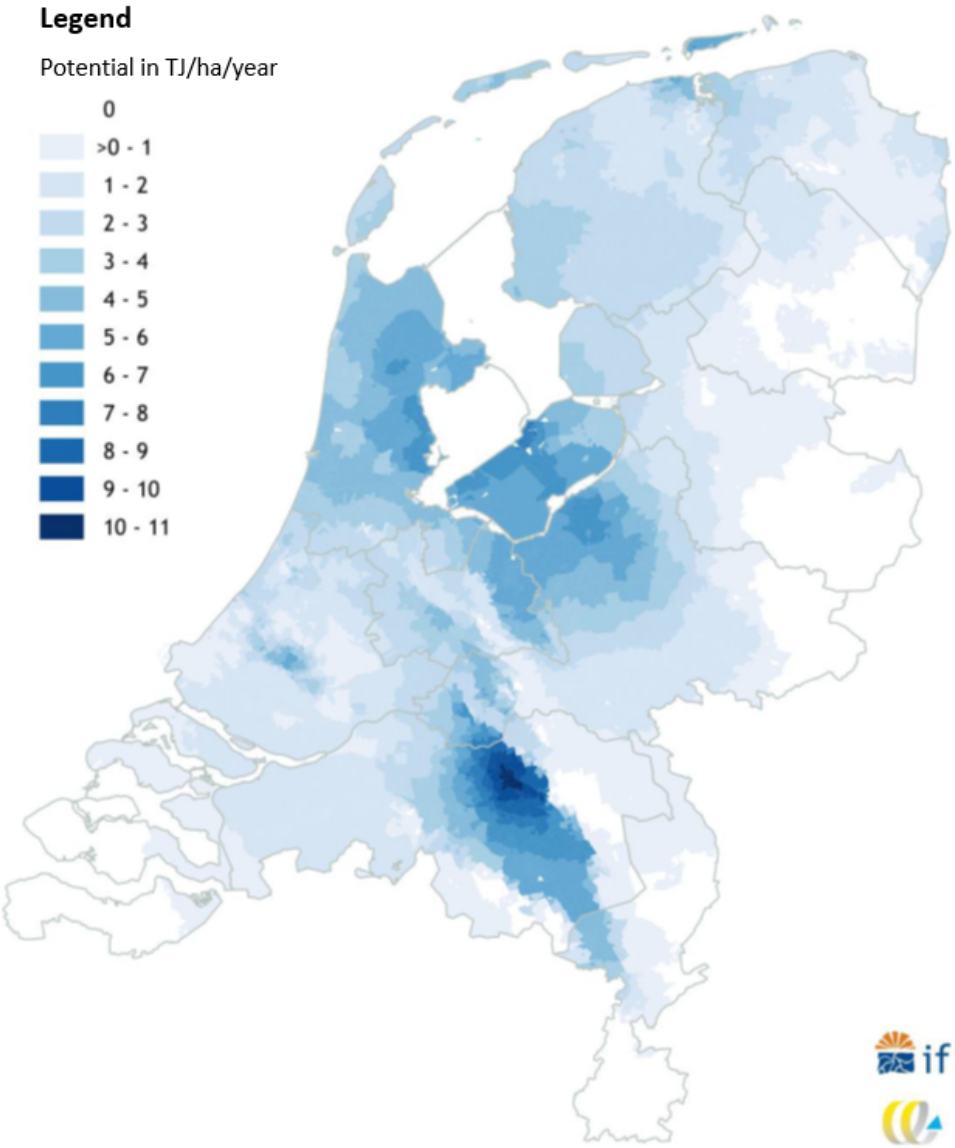

Fig. 1.1: Medium deep geothermal potential map of the subsurface of the Netherlands (Schepers et al., 2018)

1.2 Problem statement

Medium deep geothermal projects are lagging behind in the recent spur of geothermal growth. This is noteworthy since the technical potential for this geothermal type is estimated at about 229 PJ/year for the Netherlands, which is 37% of the total heat demand (Schepers et al., 2018). The temperatures from these medium deep sources are ideal to feed into low-temperature heating networks, which are much more energy efficient compared to the current dominant high-temperature variant (Van Vliet et al., 2016). In the future, medium deep aquifers could be utilized not only as source, but also as storage capacity in heat networks known as *smart thermal grids* (Schepers et al., 2018). Lastly, drilling shallower wells will save a lot in capital expenditures.

Despite the high potential and low investment costs, medium deep geothermal has largely been overlooked until recently. This disinterest is mainly due to the little geologic knowledge on medium deep formations as well as legislative constraints. New geologic understanding of these formations is necessary to accelerate the heat transition away from fossil fuels. In the following sections, the main barriers for medium depth geothermal development are elaborated.

Reservoir characterization

Potential medium deep (200 - 1500 m depth) reservoirs are still very much underexplored in the Netherlands. These formations have historically been neglected by the oil and gas industry because they usually don't contain any significant hydrocarbon reserves. Additionally, medium deep reservoirs are generally too deep and saline for the drinking water sector. The medium interval falls in between these fairly well characterized upper 200 m and deep hydrocarbon baring formations. To illustrate this further, TNO manages two subsurface models: DGM Deep and REGIS. The DGM Deep model is the basis for the ThermoGIS application (TNO, 2022d) and includes interpreted seismic data and well data for formations up to the Upper North Sea (NU) Group. Some potential medium deep reservoirs are part of this group, such as the Oosterhout and Breda formations, but these are not included in the DGM Deep model. Moreover, the shallow seismic data used for this model is often noisy, making the interpretations of the shallowest formations disputable. The REGIS model includes the NU group, however this model is based on horizontal correlation of shallow wells, without the inclusion of seismic interpretations. The inaccuracies are especially prevalent in the deepest formations (Breda and Oosterhout formations) in the REGIS model, since most shallow wells have a TD less than 500 m. The medium depth interval overlaps partly with the bottom of the REGIS model and top of the DGM Deep model, which are the least trusted parts of the models. The medium depth could be characterized as a 'grey area'.

Literature on this interval is limited. Prior studies focused on high temperature storage (HTS) applications (e.g. Arntz et al., 2020), and on reservoir characterization and seismic

interpretation of the Brussels Sand member (BSM), a promising medium deep geothermal reservoir (De Haan et al., 2020; Geel & Foeken, 2021). Geel and Foeken (2021) found that conventional petrophysical techniques are not always applicable in this depth range, due to the (almost) absence of core measurements and well tests (used for calibration), disturbances of (gamma ray) logs due to logging through casing and potassium drilling mud. Moreover, the well log data-density is relatively low compared to deeper formations. Seismic interpretation and petrophysical analyses must be conducted on the other underexplored medium deep formations in the Netherlands to further enhance knowledge on the potential of medium deep geothermal. From literature, prime targets are the Oosterhout and Breda formations. These two formations have no prior in depth studies on their reservoir characteristics and are also not included yet in ThermoGIS. The Breda Formation is older and therefore situated deeper (see Figure 1.3), with higher formation temperatures. This formation will be the main target for this thesis. The choice between Oosterhout and Breda as focus for this work is further elaborated in section 1.4.

Well design

The well design for medium deep wells differs from deep wells in completion, surface set-up (BOP, wellhead), configuration and sometimes trajectory. Completion standards for geothermal wells are formalized in a Code of Practice (CoP), published by Geothermie NL (2020). The CoP is applicable to wells ranging from 500 to 4000 m depth and is suited for very saline formation waters. However, since medium deep wells are commonly drilled within shallow to medium deep reservoirs, possibly even above 500 m depth, it is questionable to what extend this CoP is applicable to all medium deep operations. Moreover, according to De Kruijf (2019), shallower aquifers are less saline and therefore less corrosive.

A blowout preventer (BOP) is required for all drilling operations below 500 m depth, as the chance of encountering oil and gas in combination with regions of high pressure increases with depth. If it is absolutely certain that an area does not contain hydrocarbons up to a particular depth, safety measures like a BOP could be replaced by cheaper alternatives (Hellebrand et al., 2012). Most oil and gas in the Dutch subsurface is found at depths between 1000 and 3000 m, but in some places also shallow gas is present. EBN mapped shallow gas pockets in the Dutch offshore (Van den Boogaard & Hoetz, 2012), which is an ongoing endeavor within the GEODE program. No efforts on mapping onshore shallow gas plays have been initialized yet.

The well configuration and trajectory for medium deep geothermal wells also differs from conventional, deeper wells. Drilling the production and injection well is usually done at the same site, to mitigate costs and nuisance. Because the reservoir is shallow, strong deviated wells must be drilled to gain sufficient step-out. This is necessary to extend the doublet's lifetime and prevent early cold water break through. In Zevenbergen, Visser & Smit Hanab used an inclined wellhead when drilling the injection well in the BSM, such that deviation could start at the surface already (Schepers et al., 2018). Another reason

for choosing inclined or horizontal wells is the larger screen length within the reservoir. This increases the possible maximum flow rate and could make uneconomic (thin) aquifers interesting for development. However, the project in Zevenbergen currently experiences lower than expected flow rates. More research is needed on the effect of horizontal wells on geothermal production.

Legislation

Current Dutch legislation states that the boundary between the Water and Mining law is situated at 500 m TVD. Some potential aquifers cross this boundary. For example, the BSM is a potential aquifer for medium deep applications (De Haan et al., 2020; Geel & Foeken, 2021). Its depth in the Netherlands ranges from about 200 to 1200 m depth. At some locations, this member crosses the 500 m boundary. These 'overlap regions' are roughly indicated on Figure 1.2. For these regions, both the Water and Mining law would apply, making the exploitation of these parts of the BSM extra challenging. Also illustrative is the recent drilling of the 'DAP monitoring well', where the total depth (TD) is 499 m.

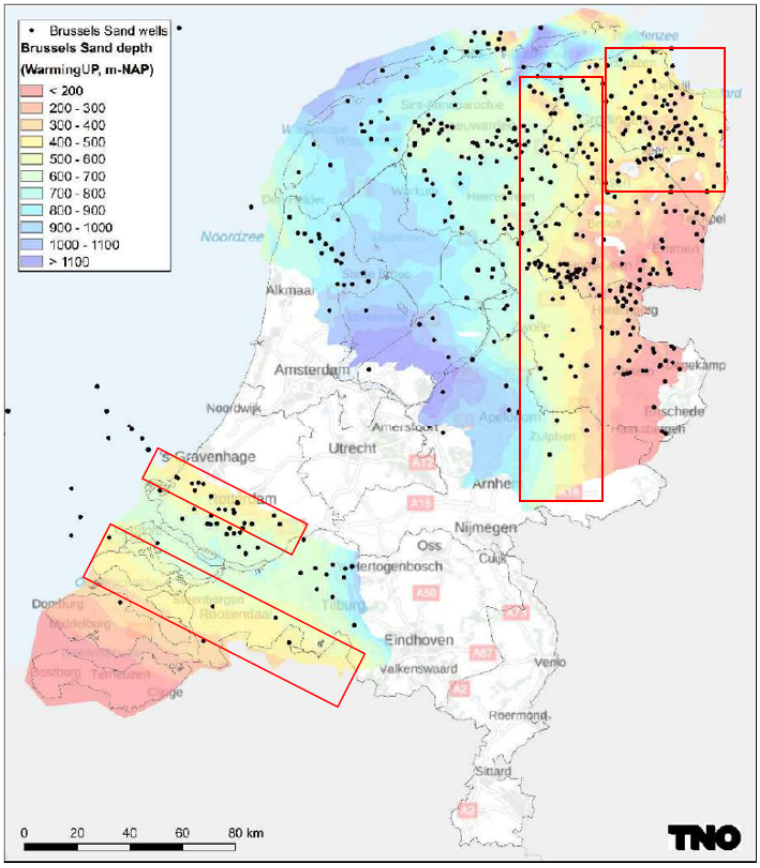

Fig. 1.2: Top depth map of the Brussels Sand member in the Netherlands. Overlap regions where both the Water Law and Mining Law would apply are roughly indicated by the red boxes (after De Haan et al., 2020)

1.3 Research questions & approach

Following from the previous section are three main themes which comprise the current obstacles for medium deep geothermal development. The themes are reservoir characterization, well design and legislation. The following research questions and sub-questions are derived from these themes:

1. What are the reservoir characteristics of the Breda Formation?
    - Where are the high potential areas?
    - How good are the current (seismic) interpretations of the bounding surfaces of the Breda Formation, and can these be improved using new and/or old (seismic) data?
    - Are the existing well log data within the Breda Formation sufficient for creating a static reservoir model?
    - If a static model can be created, what are the potential production rates from the reservoir?
2. What is the optimal well design for medium deep wells?
    - What are the optimal well configurations for the Breda Formation specifically and medium deep geothermal in general?
    - What is the salinity of the formation water in the Breda Formation?
3. How is the current Dutch legislation for medium deep geothermal defined and how does this enable or limit medium geothermal development?
    - How do the Dutch rules compare with other EU countries?

To answer these questions, the initial focus is placed on characterizing the Breda Formation and finding a focus area based on Tertiary depocenters. Seismic and well log data are available on NLOG, which are assembled, evaluated, corrected and interpreted in order to determined whether a static reservoir model can be created. Additionally, new data was required to support and calibrate the calculated petrophysical values from the well logs. These were acquired by analysing cuttings from a selection of wells within the focus area which have suitable well logs. Interpretations of the bounding horizons, which have never been interpreted before in this area, are realized on new and old seismic data to define the top and bottom of the static model. In order to correlate the wells in this area, new biostratigraphic data are acquired. Once a static reservoir model is created, dynamic simulations are conducted to determine the doublet lifetime, flow rates and optimal well design. Lastly, the legislative rules of the Netherlands regarding medium deep geothermal are elaborated, as well as the implications on geothermal development. A comparison with other EU countries is also provided.

1.4 Introducing the Breda Formation

On national scale, the most promising medium deep reservoirs are the Oosterhout Formation, Breda Formation and Brussels Sand Member (BSM) (Hellebrand et al., 2012). The BSM was recently studied by De Haan et al. (2020) and Geel and Foeken (2021). This formation is now included in the ThermoGIS application (TNO, 2022d). The Oosterhout and Breda formations both remain underexplored from a reservoir characterization perspective and are therefore not yet included in ThermoGIS. Since incorporating both the Oosterhout and Breda formations into this study would be too time consuming, one of the two is chosen. The Breda Formation is older than the Oosterhout Formation and therefore situated deeper, as shown in Figure 1.3. This implies that water temperature should be higher in the Breda Formation. Using the TNO REGIS database, Hellebrand et al. (2012) composed a thickness and base depth map of the Oosterhout and Breda Formations (see Figure 1.4 and Figure 1.5). These maps are derived only from shallow well data and are therefore not very accurate. Nonetheless, these do provide some insight and are therefore used in deciding between the two formations. The net thicknesses are roughly comparable, however not always at the same locations. The Breda Formation seems to have a better overlap between largest depth and largest thickness, especially in the south-east and middle Netherlands (see Figure 1.4). Based on these maps and the REGIS cross section in Figure 1.3, the focus is directed towards the most promising formation in terms of geothermal potential, being the Breda Formation.

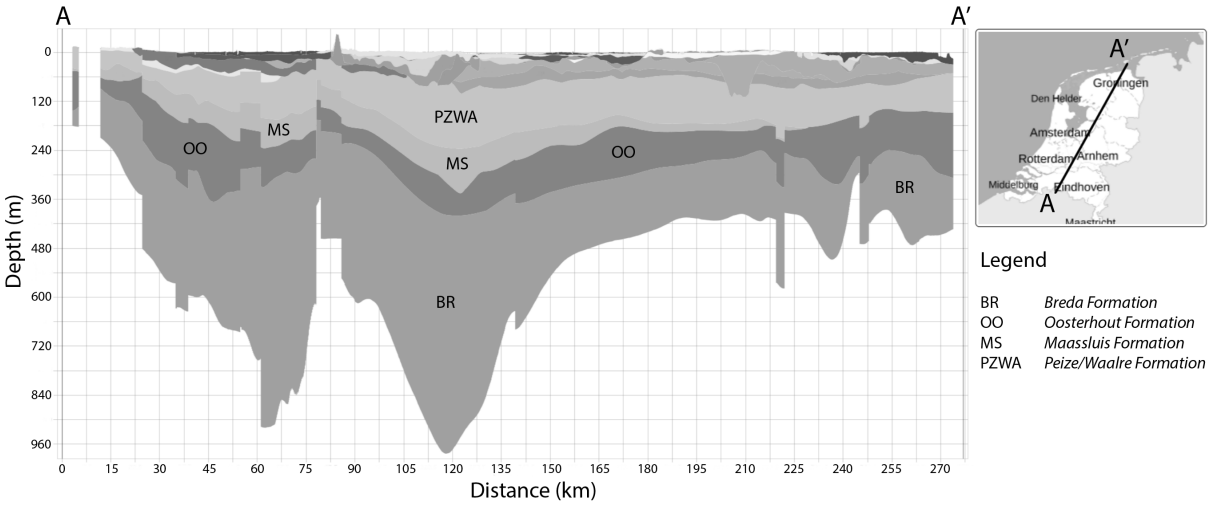

Fig. 1.3: Cross section through the Netherlands showing the NU Group formations, based on the REGIS model (TNO, 2022c)

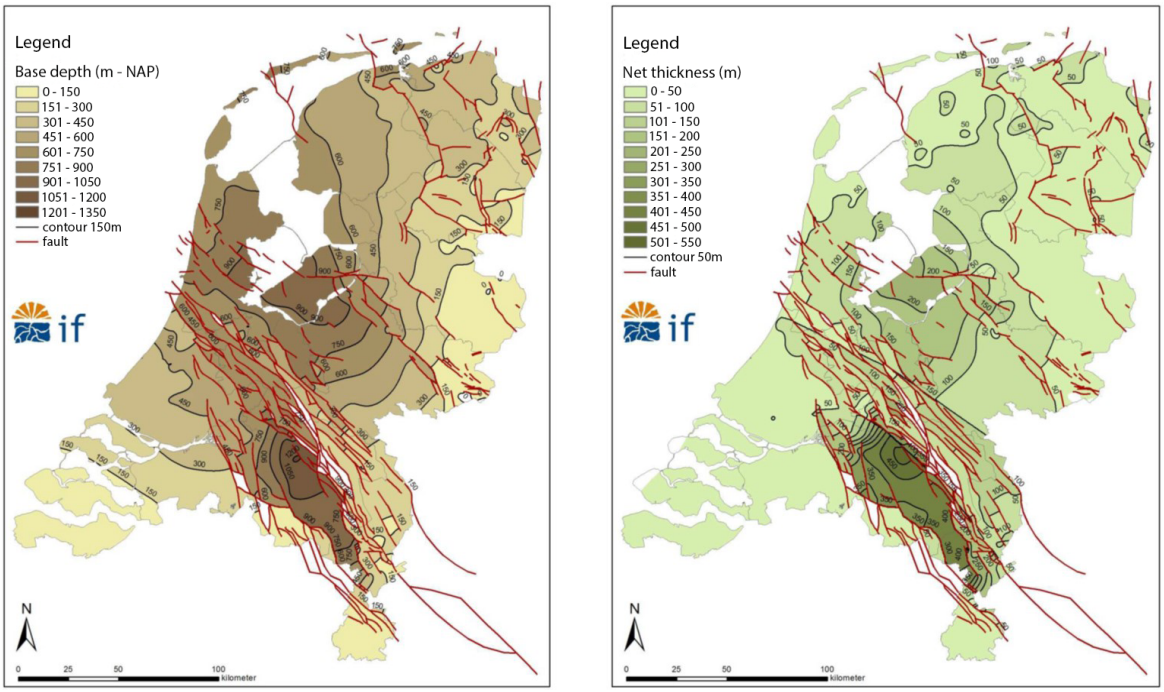

(a) Base depth map **(b)** Net thickness map

Fig. 1.4: Maps Breda Formation (after Hellebrand et al., 2012)

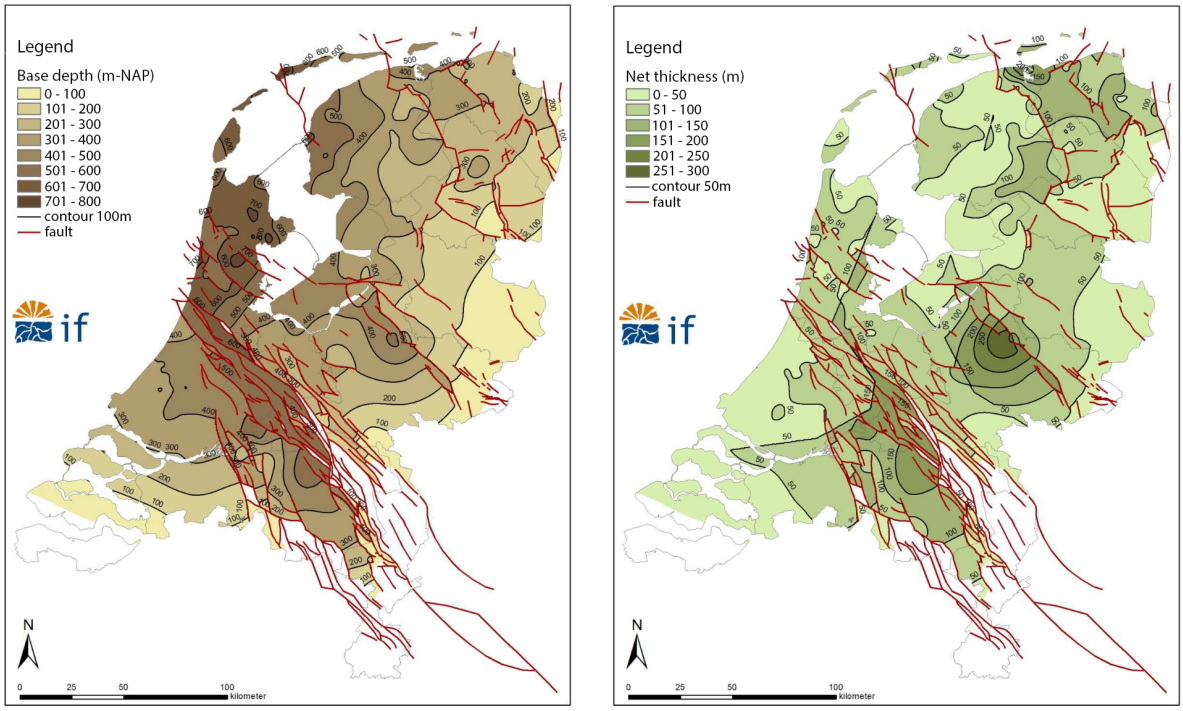

(a) Base depth map **(b)** Net thickness map

Fig. 1.5: Maps Oosterhout Formation (after Hellebrand et al., 2012)

1.4.1 Geologic background

The sediments of the Breda Formation were deposited from Late Oligocene to Early Pliocene, so mostly during the Miocene (23 to 5.3 million years ago). The base depth ranges from 0 up to about 1350 m depth (Figure 1.4a) with thickness ranging from 1 to 700 m (Figure 1.4b). During time of deposition, sediments were transported by fluvial systems from the Fennoscandian Shield, Baltic Platform and Alpine area (see Figure 1.6), whence they were deposited in a predominantly (shallow) marine environment (Munsterman & Brinkhuis, 2004; Munsterman et al., 2020; Slupik & Janse, 2008). Here the sediments were arranged mainly as foreset and bottomset beds (clinoforms) in an extensive prograding shelf-delta system. Martinius (2017) describes the architecture of deltaic foresets using the Roda Sandstone Member (RSM) as outcrop analogue. The RSM deposits could be regarded as analogue for the Breda Formation, since the depositional environments are similar (both deltaic). The RSM is already widely used as analogue for multiple oil fields off the coast of Norway. Martinius shows how heterogeneities in such a delta lobe deposit can form barriers for fluid flow, which are important factors for geomodelling and reservoir engineering. Heterogeneities in a deltaic depositional environment occur from the largest scale of switching delta lobes (10's of km wide), to cemented horizons between clinoforms (km scale) to mud drapes in tidal bedforms (m - dm scale) (Martinius, 2017). Incorporating all these heterogeneities in a static geomodel, especially the small scale ones, is very difficult. Still it is important to be aware of the possible presence of these flow barriers from a production point of view.

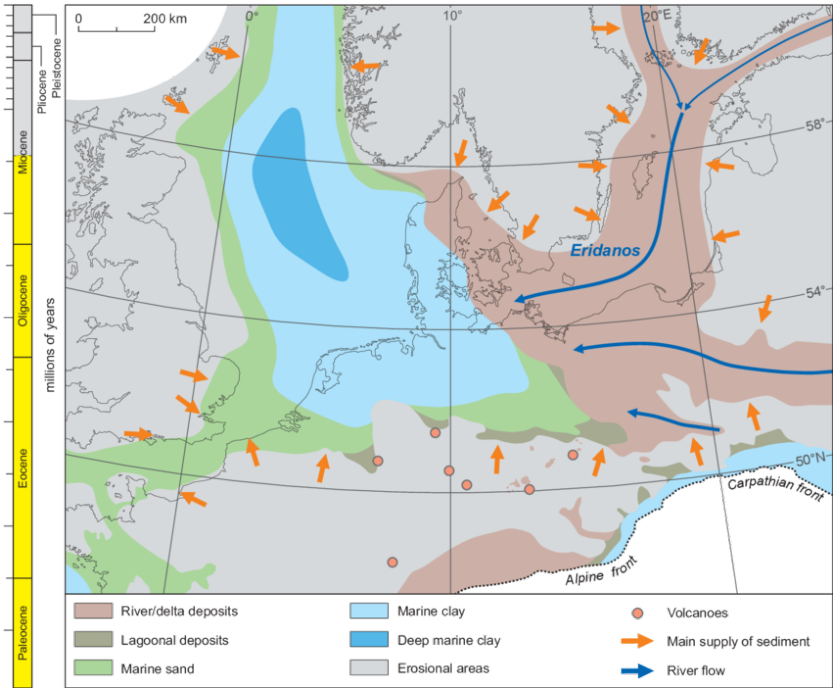

Fig. 1.6: Palaeogeography and fluvial systems during the Mid-Miocene (Gibbard & Lewin, 2016)

The Breda formation can be found almost everywhere in the subsurface of the Netherlands. As stated before, the formation varies largely in thickness. Hellebrand et al. (2012) created a thickness map of the Breda formation on national scale, based on REGIS data. In Figure 1.4b it can be seen that the Breda is between 0-50 and 50-100 m thick in most parts of the Netherlands. It is significantly thicker in some areas. These thick successions can be traced back to Tertiary depocenters. The depocenters that were active in the Netherlands during the Tertiary are the Lauwerszee Trough (LZT), Zuiderzee Low (ZZL), Voorne Trough (VT) and Ruhr Valley Graben (RVG) (see Figure 1.7).

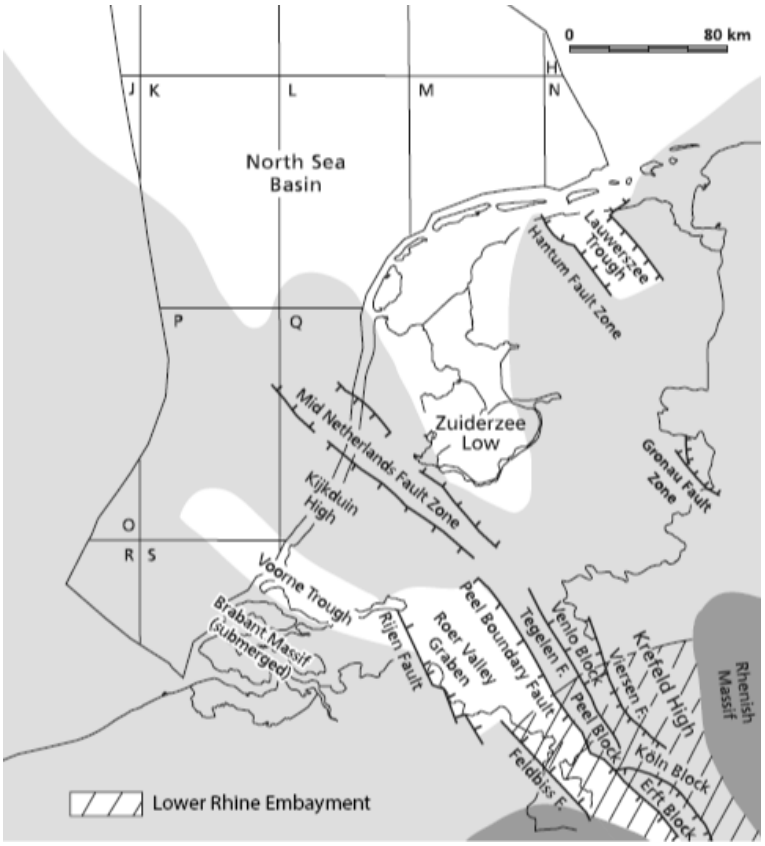

Fig. 1.7: Structural elements and basins in the Netherlands during the Tertiary. White parts represent low areas (basins), where the Breda Formation is thickest (Wong et al., 2007)

The RVG and LZT development is associated with Late Jurassic basinal development. Both basins originate from increased heat flow, magmatic activity and extensional faulting during the Late Kimmerian (Herngreen & Wong, 2007). Starting in the Late Oligocene, strong subsidence began to take place in the RVG (Geluk et al., 1994), leading to the development of a nearshore depocenter here (Munsterman & Deckers, 2022). This process led to 100's of meters increase in accommodation space, therefore the Breda Formation is relatively thick here. The ZZL developed as an additional depocenter during the Late Miocene (Munsterman & Brinkhuis, 2004), leading also to significant accommodation space. During the Late Miocene and Pliocene, the depocenter shifted from the ZZL towards the North Sea Basin (NSB) as the paleo-Rhine delta continued its NW progra-

dation. It is therefore expected that the Breda Formation in the ZZL builds out towards the North Sea, possibly as clinoform deposits. A prodelta depocenter was maintained in the RVG (Geluk et al., 1994; Munsterman & Brinkhuis, 2004), adding to the thickness of the Breda Formation here. The VT was formed during a minor rifting phase in the Late Paleocene (Wong et al., 2007). This basin was no longer active as depocenter from the Early Oligocene onwards (Zagwijn, 1989), and therefore the Breda Formation is relatively thin in this basin.

The sediments can be characterized by alternating silty clay, silts and very fine- to moderately fine-grained sands (105-210 μm) with frequent high glauconitic and/or calcite content (Munsterman et al., 2020; TNO, 2022a). In some locations, thin peat/lignite beds can be found. In the NDN-120 well, the Miocene succession consists of a (at least) 130 m thick clayey sand package. The clay beds are laminated with thickness up to a few mm (Coenen, 1974). The base of the Breda Formation quite often contains high amounts of glauconite, which became the method of determining the location of the base of this formation. The Breda Formation overlies either the Veldhoven Formation in the south and middle Netherlands, or the Rupel Formation in the north. In the ZZL the transition into the Veldhoven Formation is defined by a shift from light coloured to darker glauconitic sands. In the LZT the transition into the Rupel Formation is easier to determine since the Rupel Formation doesn't contain glauconite (TNO-GDN, 2022c). In some locations, like in the RVG and on the Peel/Venlo Block, the lower boundary is hard to recognize due to a gradual transition zone (Munsterman & Brinkhuis, 2004). In most of the Netherlands, the Breda Formation is overlain by the Oosterhout Formation (see Figure 1.3). The transition from Oosterhout to Breda is characterized by a decrease in calcareous content (shells) and an increase in mica content. However, the Breda Formation can also contain some shell fragments, especially close to the upper transition zone. Towards the southeast, the Oosterhout Formation is pinching out and consequently the Breda Formation in the Venlo/Peel block is overlain by the Kieseloolite Formation (Munsterman et al., 2020).

As mentioned before, glauconite is abundantly present in the Breda Formation. Glauconite minerals are formed in areas with a low sediment accumulation rate, in open to shallow marine environments, at the outer shelf to upper slope (Hesse & Schacht, 2011; Velde, 2014). Also, some examples of glauconite presence in lacustrine environments are known (Hesse & Schacht, 2011). The formation process continues when buried at a few decimeter depth. The entire process takes around a million years to finish, under oxic to suboxic circumstances (Hesse & Schacht, 2011; Velde, 2014). The diagenesis of glauconite includes the replacement of smectite clays with potassium in appropriate porous substrates with a wide compositional variation (Hesse & Schacht, 2011). It is this relative enrichment in potassium that is responsible for sometimes large 'clay effects' on gamma ray logs, which could lead to mistaking a glauconite rich sandstone for a shale layer (Kennedy, 2015).

Earlier efforts on mapping the Breda Formation were based on horizontal correlation between shallow (drinking water) wells, without including seismic interpretations. Figure 1.3, Figure 1.4 and Figure 1.5 are all based on the shallow well database REGIS. Munsterman et al. (2020) provided an updated stratigraphic framework for the Breda Formation in the RVG and adjacent blocks, based on seismic interpretations. They separate the formation into two units (see Figure 1.8). Unit 1 comprises the bottom part of the Breda Formation. The base of Unit 1 in the RVG and Campine block is defined by the Early Miocene Unconformity (EMU). Unit 2 overlies Unit 1. The units are separated by a major hiatus called the Mid-Miocene Unconformity (MMU), which is not only present in the RVG but in the Peel/Venlo block as well. The top of Unit 2 in the RVG and Campine block is defined by the Late Miocene Unconformity (LMU).

According to Munsterman et al. (2020) the two new units which make up the Breda Formation show unique (seismic) characteristics and should therefore receive their own lithological name. Unit 1 and 2 were assigned the names 'Groote Heide (GH) Formation' and 'Diessen Formation', respectively. During this thesis it is investigated to what extent these new definitions are applicable to other parts of the Breda Formation.

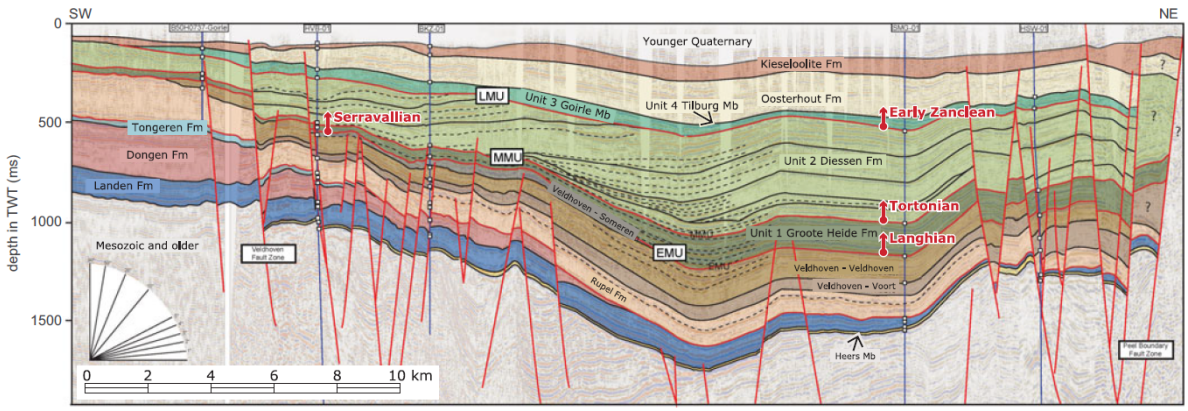

Fig. 1.8: Geological interpretation of a southwest-northeast seismic line through the RVG from Goirle to Heeswijk, with the newly proposed units and corresponding names (Munsterman et al., 2020)

Over- and underburden

Information on the over- and underburden of the Breda Formation is vital when exploring the geothermal reservoir capabilities of the formation. A sealing top and bottom layer is necessary in order to prevent any unwanted induced flow into under- or overlying strata.

Overlying the Breda Formation in most part of the Netherlands are sediments of the Pliocene Oosterhout formation, as stated before. The stratigraphic nomenclature provides a general definition for this formation stating very fine to very coarse sands (105-420 µm) with some clay and shells (TNO-GDN, 2022b). The local composition is relatively unknown, since very limited literature is dedicated to this formation. One exception is a

report by Coenen (1974), which describes the geological findings in the NDN-120 well. A chemical company wanted to utilize this well to dispose waste water in the Miocene sand package. The purpose of the survey was to characterize the potential sealing Pliocene layer situated above the Miocene interval. The geological survey shows that the Miocene interval is overlain by a clay dominated 112 m thick Pleisto-Pliocene succession with laminated clay layers. The majority of clay layers observed were roughly 1 cm thick, while six larger layers were found with a total thickness of 22.5 m. The clay layers are correlated with a similar succession found in the WSP-01 well. Coenen (1974) concludes that the laminated clay layers most likely continue laterally over a larger area, at least up to WSP-01. Further quantitative data on the lateral extent of the clay layers is not provided.

The underburden consists of the clay-rich Veldhoven and Rupel formations, from top to bottom (TNO-GDN, 2022a, 2022c). More literature is available on the local composition of these formations compared to the Oosterhout Formation (e.g. Munsterman and Deckers, 2022). In well Doornspijk-02 these formations are 96 and 64 m thick, respectively (TNO-GDN, 2022a, 2022c). From a reservoir perspective, these formations likely form a sealing bottom boundary for the Breda Formation reservoir.

Chapter 2

Reservoir characterization

As stated before, the current available mapping and characterization of the Breda Formation in the REGIS model is not sufficient and most likely inaccurate. This is illustrated further by the REGIS interpretation of the Breda sand thickness, shown in Figure 2.1. The figure suggests that no sand is present in the ZZL, and the entire Breda succession should consist of clay. This assumption is likely faulty, since a cutting analysis shows that fine grained sand is in fact present in two wells towards the North (see section 2.1.2). Furthermore, the DGM Deep model only contains the base of the Breda Formation. The geothermal industry wants to expand their options into the medium deep domain, thus better reservoir characterization of the medium deep reservoirs are necessary. In this chapter, the methods used in this thesis to map and characterize the Breda Formation can be found, as well as the results and key take-away points.

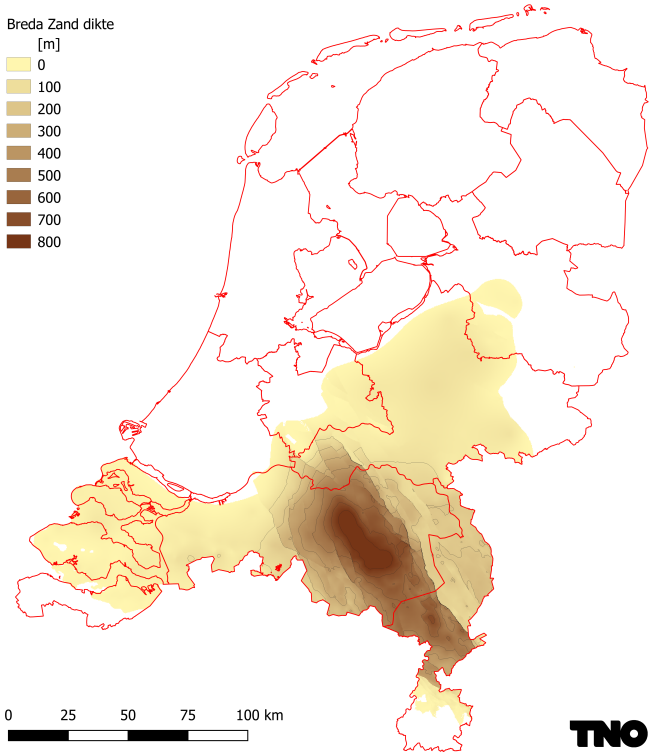

Fig. 2.1: Current interpretation of the sand thickness in the REGIS model. Notice how the sand stops towards the North in this interpretation

2.1 Method

In this section, the methods used to map the Breda Formation and characterize its reservoir properties are discussed. New and old data are assembled and utilized in order to obtain novel interpretations of the reservoir extend and petrophysical characteristics, eventually leading to a static reservoir model.

2.1.1 Data availability and regional focus

Due to time constraints, it was not feasible to incorporate the whole extend of the Breda Formation in this study. Instead, the focus is directed to a few regions with the hypothetically highest geothermal potential. In section 1.4.1, four Tertiary depocenters were identified (see Figure 1.7). The following table summarizes all data available per basin.

Tab. 2.1: Available data per Tertiary depocenter

Depocenter	'Deep' wells (NLOG)	'Shallow' wells (REGIS)	Seismic data type
Lauwerszee Trough	36	3	3D (full coverage)
Zuiderzee Low	31	3	2D & 3D (Noord-Holland)
Voorne Trough	2	0	2D (low density)
Ruhr Valley Graben	7	+- 40	2D

From these four basins, Zuiderzee Low (ZZL) is selected as region of interest for this thesis. This depocenter was chosen since no prior studies on the Miocene interval have been undertaken, the basin has a relatively high well density with decent log suits, sufficient seismic data are available in the area and, according to REGIS, the Breda Formation is quite thick here (see Figure 2.2). The Ruhr Valley Graben was not further investigated here because a study on the stratigraphic framework for the Miocene in the RVG has recently been published by Munsterman et al. (2020). Additionally, TNO is currently working on a new reservoir characterization study in the RVG. Furthermore, the Breda Formation in the Voorne Trough is <15 m thick, according to end-slip interpretations in wells HVS-01 and OVE-01 (TNO, 2022b). This basin was mainly active as depocenter during the early Paleocene, while the Breda Formation was mainly deposited during the Miocene (as discussed in section 1.4.1). Furthermore, the data density in the VT is low. Due to the minor thickness and data density, the VT is not considered a region of interest.

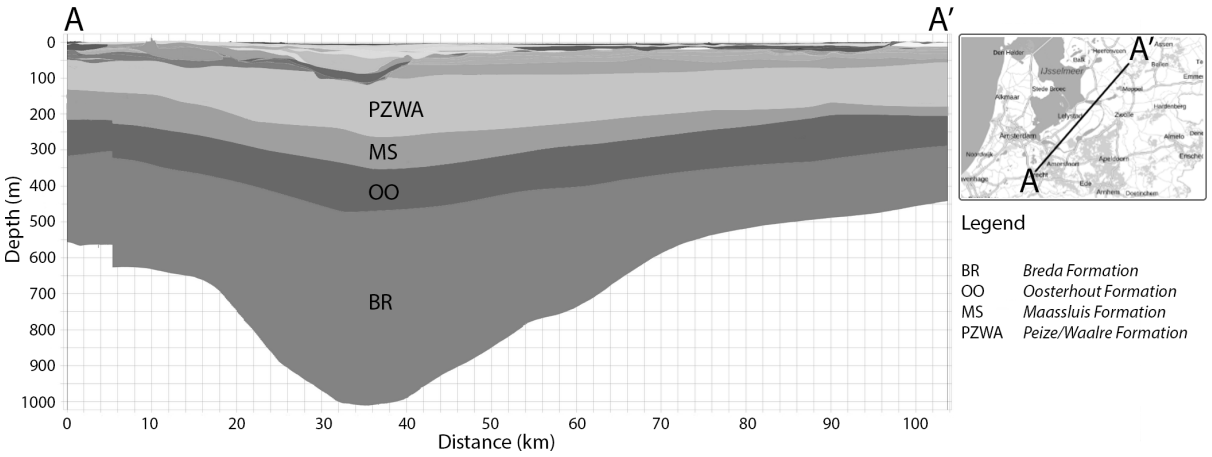

Fig. 2.2: Cross section through Flevoland showing the NU Group formations, based on the REGIS model (TNO, 2022c)

Initially, the Breda Formation in the LZT was also included in this thesis. This trough was active as depocenter during the Miocene (see section 1.4.1), 36 deep wells were drilled through the Breda and 3D seismic cubes cover the entire extend of the basin. In the initial stage of this thesis, the cubes were used to identify the Breda Formation in this area, resulting in novel total thickness and depth maps (top and base). Still, this basin was excluded from further analysis due to the following observations:

- The seismic quality in the shallow part of the 3D cubes is poor. Especially the top reflector (LMU) is very hard to recognize and disappears quite often.
- The produced thickness map shows relatively low thickness onshore, and highest thickness offshore, which makes the formation less interesting for geothermal developments.
- No biostratigraphic data are available for the medium deep interval.
- The log suits in the medium deep domain are limited. Only 3 wells contain a porosity log.
- The majority of gamma ray logs are (heavily) influenced by either logging through casing or by potassium-rich drilling muds.

Zuiderzee Low data availability

For this thesis, 31 'deep' wells are used located in the ZZL, which can be found on NLOG (TNO, 2022b). The majority of these wells were drilled by the hydrocarbon industry. Most hydrocarbon reservoirs are located much deeper than the shallow Breda Formation, hence the reason why the companies acquired only limited (log) data from this interval. Table 2.2 shows the available data per well in the ZZL. In Figure 2.4 the wellhead locations are shown.

Additionally, TNO maintains a large 'shallow' wells database (REGIS). These wells were mainly drilled by the drinking water industry and have a TD of a few hundred meters

(deeper aquifers are often too saline). Wells within this database are no deeper than 500 m due to mining law regulations. Still, many (partially) penetrate the Breda Formation in locations where the formation is situated close to the surface. Some have a basic log suite, as well as detailed lithological information describing sand to clay ratio, grain sizes and shell and glauconite content. Figure 2.3 shows all shallow wells which penetrate the Breda Formation, including lithology types. Noticeable is the anisotropic spread of the wells. This can be explained by variations in the top depth of the formation. Table 2.3 lists the shallow wells located close to the ZZL.

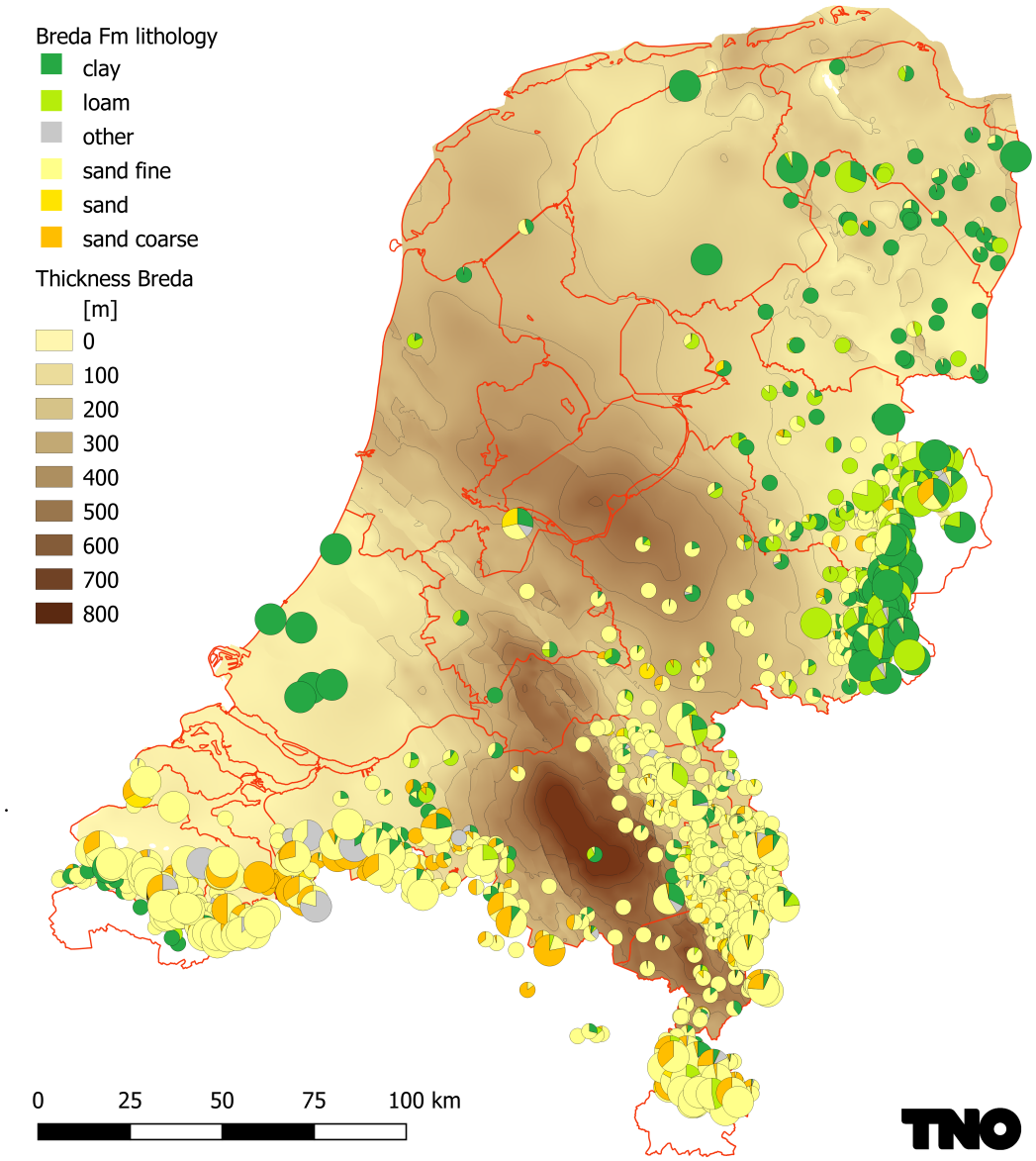

Fig. 2.3: Breda Formation thickness map (REGIS) showing all shallow wells which penetrate the formation. Lithology percentages found in each well are indicated (TNO, 2022c)

Tab. 2.2: Selected 'deep' wells in the ZZL with available data from the Breda formation. The recorded mud is the type used while drilling through the Breda Formation

Name	Spud year	Available logs	Mud type	Biostratigraphy
ADK-GT-01	2017	GR	Unknown	Yes
ADK-GT-02	2018	GR	Unknown	
ADK-GT-03	2018	GR	Unknown	
ADK-GT-04	2018	GR	Unknown	
ALE-01	1976	GR, RHOB, NPHI	Gypsicum mud	
BLA-01	1982	GR, DT,	KCl polymer	Yes
DRO-01	1965	GR, DT	Chemgel Spersene	
EPE-01	1971	GR, DT, RHOB	XC polymer salt mud	
HOK-02	1964	GR	FWM	
KGB-01	1987	GR	Spud mud	
KKP-GT-01	2011	GR	Water based	
KRD-01	1978	GR, DT, SP, ILD, RHOB, NPHI	Polymer mud	
LEL-01	1970	GR, DT	XC polymer	
LSM-01	1977	GR, DT, RHOB, NPHI	FWM	Yes
LTG-01	2004	GR	KCl polymer	
MDM-GT-02	2013	GR	KCl-Glycol polymer	
MDM-GT-03	2013	GR	KCl-Glycol polymer	
MDM-GT-04	2014	GR	KCl-Glycol polymer	
MDM-GT-06-S2	2017	GR	Unknown	
MID-101	1964	GR, DT	FWM	
MID-201	1980	GR, DT	FWB	
MKN-01	1983	GR	FWM	
MKO-01	1986	GR	KLIM	
NAG-01	1970	GR, DT	Bentonite	
NDN-120	1974	GR, DT, RHOB (upper part)	Starch Perfectamyl	
OFL-01	1965	GR, DT	FWM	Yes
RST-01	1976	GR, DT, RHOB	FWM	
SLD-01	1964	GR, DT	Bentonite	
WBMS-01	1993	GR	KMG	
WSP-01	1970	GR, DT, SP, RHOB	XC polymer	
ZEW-01	1965	GR, DT (part)	Bentonite	

Tab. 2.3: Selected 'shallow' wells in the ZZL which partially penetrate the Breda Formation (TD within the formation)

Name	Available logs	Grain size description	Shell content description	Glauconite content description
B32F0113	None	Yes	Yes	Yes
B32G0137	GR, SP	Yes	No	Yes
B32H0227	GR, SP	Yes	Yes	Yes

Cuttings from various wells are available in the TNO Central Core Sample Storage in Zeist. Cuttings are pieces of the formation rock brought up from the borehole by the drilling fluid during drilling. Usually cutting samples are taken every 5 or 10 meters. These samples can be analysed for dating (biostratigraphy), mineral composition and grain size estimation. Cuttings come in washed and unwashed form, both having their respective up- and downsides. Washed cuttings are cleansed from any residual drilling mud, however the finest fraction of the original formation material is lost in the process. Unwashed cuttings embody all original rock material, however the residual drilling mud contaminates the sample. While writing this thesis, cuttings from wells BLA-01, LSM-01 and OFL-01 are sampled for biostratigraphic interpretation (Houben, 2022). Additionally, cuttings from wells ADK-GT-01 and KRD-01 are inspected under the microscope to determine grain sizes, shell content and glauconite surface percentage. The cutting analysis is elaborated in section 2.1.2.

Most of the seismic data in the ZZL area consist of 2D seismic lines. 3D seismic cubes are available near Slootdorp and in the Beemster. The lines and cubes can be retrieved from NLOG. Additionally, within the SCAN (Seismische Campagne Aardwarmte Nederland) project many new 2D lines were published, as well as some old reprocessed lines (Van Lochem et al., 2019a, 2019b). Figure 2.4 shows the seismic lines and cubes that were used for mapping the Breda Formation in the ZZL.

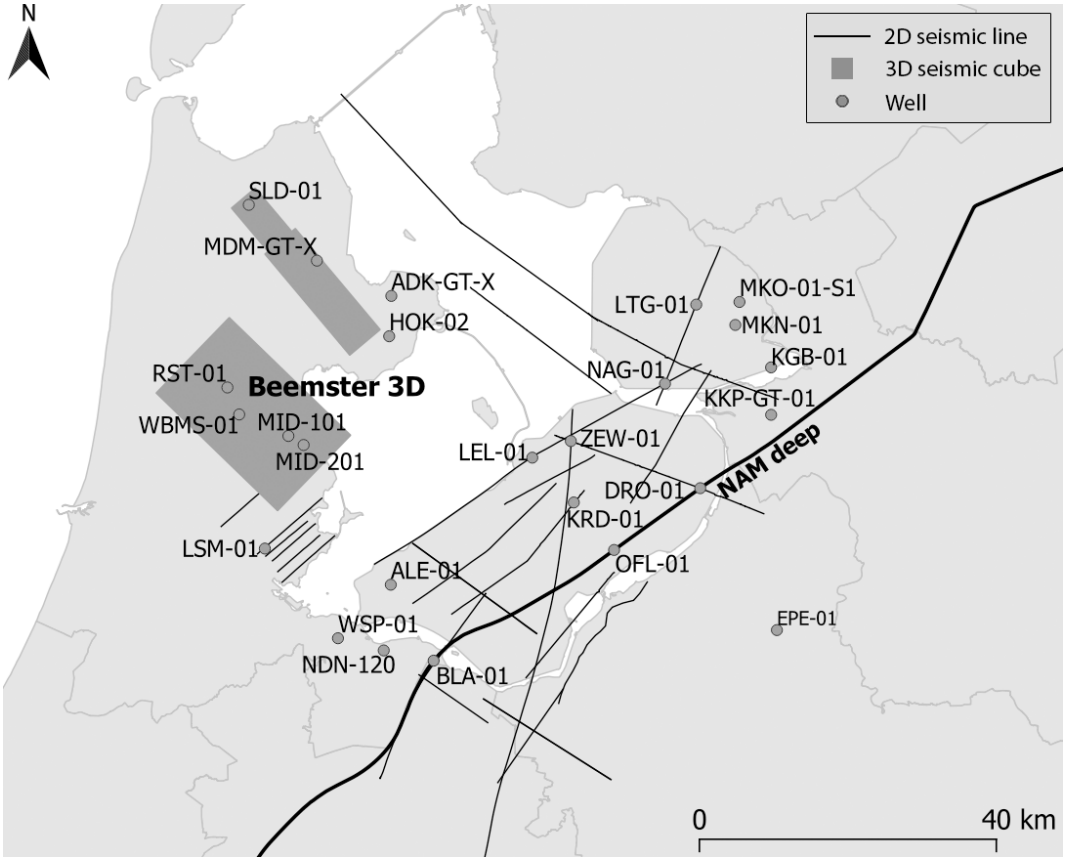

Fig. 2.4: Map showing the seismic lines/cubes and wells used for this thesis

2.1.2 Cutting analysis

As mentioned in the previous section, cuttings from various wells are available at the TNO Central Core Sample Storage. While writing this thesis, a biostratigraphic study on cutting samples from BLA-01, LSM-01 and OFL-01 wells was done within the WarmingUP project (Houben, 2022). More on the biostratigraphic study and corresponding well correlation can be found in section 2.1.3.

Apart from biostratigraphy, cuttings from ADK-GT-01 and KRD-01 were analysed for this thesis. This was deemed important after establishing a repeating pattern in the gamma ray log in each well within the ZZL. Above the MMU, a re-occurring relatively high gamma ray interval can be noticed (see Figure 2.5). Initially this interval could be interpretated as a clay layer, however in section 1.4.1 it is mentioned that the Breda Formation can contain high amounts of glauconite. This mineral can have a significant effect on the gamma ray tool, similar to clay minerals (Asquith et al., 2004). Therefore, cuttings are analysed to find out whether this phenomenon was caused by glauconite, clay or a combination of both. Furthermore, the cuttings are important because other parameters can be derived from the samples, namely shell content, grain size, sphericity and sorting. These parameters are important for stratigraphic correlation and permeability calculation.

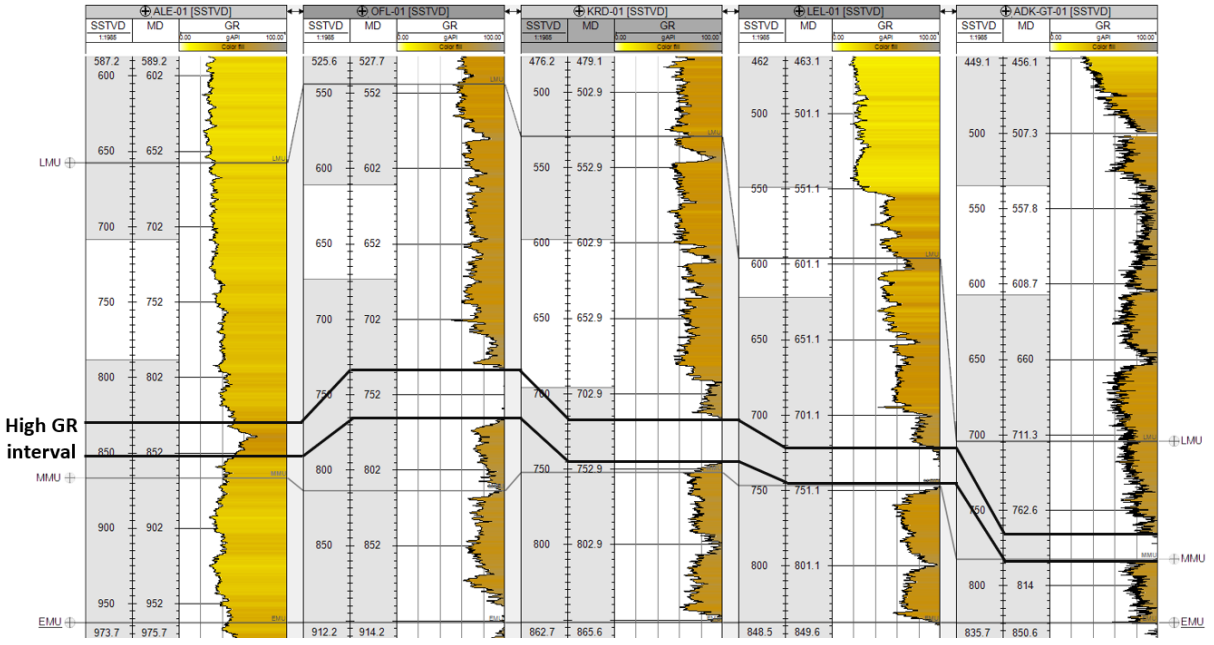

Fig. 2.5: Selection of wells from ZZL area where the high gamma ray interval is indicated

ADK-GT-01

Cuttings from the ADK-GT-01 well are collected every 5 m MD. The cuttings from this well are washed and sorted in a fine and coarse fraction (see Appendix A). The coarse

fraction contains mostly clasts of smaller, clumped grains which are not suited for grain analysis if not crushed. Therefore only the fine fraction is examined further.

The Breda interval in this well is situated roughly between 710 and 840 m MD. Therefore, cuttings from depths 640 to 860 m MD were analysed. This was done by making microscope photos. 31 images were shot in total with either 5 or 10 m intervals. A sample frequency of every 5 meters is only retained in the 'high gamma ray' interval.

The glauconite surface percentage can be determined via image processing. The surface percentage provides an indication of the glauconite fraction at a specific depth. The Fiji software by ImageJ is used for this purpose. The workflow is relatively simple and similar for each image: first the RGB color range for glauconite minerals in the specific image must be determined. A color threshold is then applied for this color range. This results in the software selecting only the glauconite grains, if done correctly. Finally, a binary image is created where the pixels within the color threshold are assigned a value of 1 (white), and all others a value of 0 (black). Subsequently, one can calculate the fraction of the white pixels relative to the total amount of pixels in the image. This fraction corresponds to the surface percentage of glauconite minerals in the sample. As example, the resulting binary image for cuttings from 680 and 780 m MD are shown in Figure 2.6. The outcomes for all 31 images are plotted in Figure 2.16 in the Results section. The shell content is also included in this chart, which were visually estimated from the samples (see Appendix A for an image of all samples).

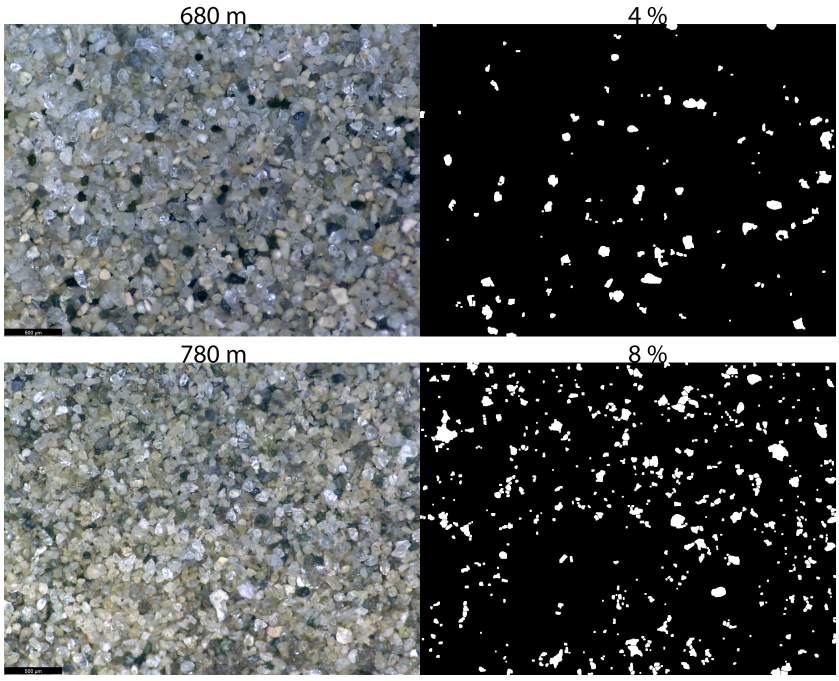

Fig. 2.6: Glauconite can be visually recognized as (dark) green grains (left images). Glauconite surface percentage can be calculated from binary images (right images). A useful chart for visual estimation can be found in Appendix A.

The grain sizes from the ADK-GT-01 cuttings are calculated in a similar fashion, using the Fiji software. The workflow is defined as follows: find a RGB color range which incorporates as many grains as possible, while leaving out the pore spaces. The color threshold can then be applied for this range. Again a binary image is created. The watershed plugin is then applied to undo unwanted clumping. This plugin conducts watershed segmentation on the image using flooding simulations as proposed by Soille and Vincent (1990). The Feret diameter is then calculated for each grain. As example, the workflow for cutting sample 780 is shown in Figure 2.7. The same process is applied to cuttings from depth 710 to 840 m with 10 m increments. The results for all analysed cuttings are shown together in Figure 2.17 in the Results section.

Lastly, the sphericity and sorting is approximated based on the cutting images. Using a chart by Mahmoudi et al. (2015) (see Appendix A, Figure A.3), the general sphericity and grain sorting can be determined. The results are shown in section 2.2. The effects on permeability of the grain size, sphericity and sorting from the ADK-GT-01 well are further discussed in the Permeability subsection in the Petrophysics section (section 2.1.5).

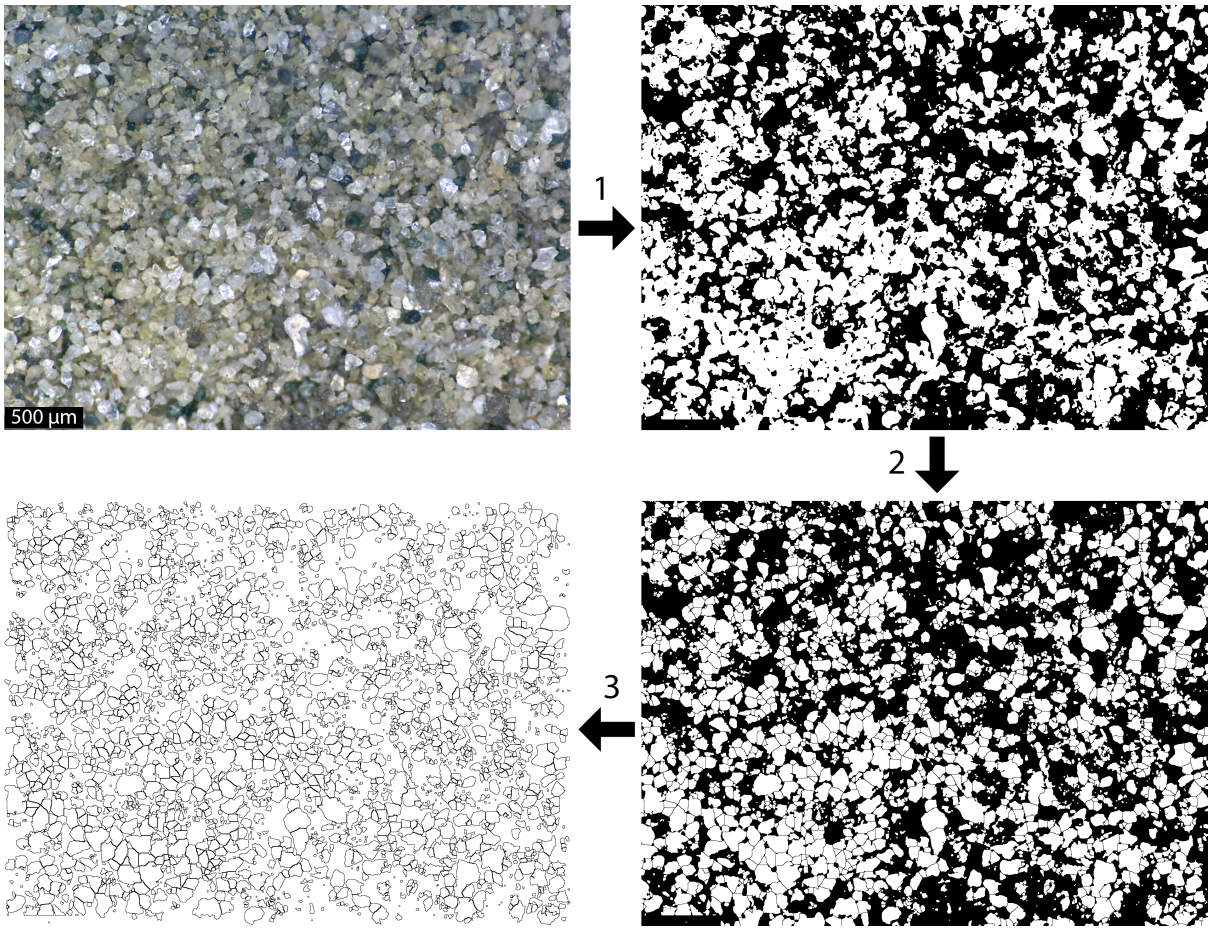

Fig. 2.7: Grain size determination workflow for ADK-GT-01 cuttings from 780 m depth. 1: Binary image creation from original image. 2: Watershed algorithm. 3: Identifying grains and calculating Feret diameter for each grain

KRD-01

Due to time constraints, the cuttings from the KRD-01 well were analysed less carefully. These cuttings are unwashed, and therefore the finest fraction is still present. From these samples it can be determined whether the cuttings contain a clay fraction in the high GR interval. Three sample depths are selected: 670, 740 and 760 m MD. 740 m MD is situated at the center of the high GR interval, while 670 and 760 m MD should be above and below the interval, respectively (see Figure 2.5). The samples were inspected at the Central Core Sample Storage by hand (making wet and feeling for sand/clay presence, tasting for sand particles) and observed under the microscope (see Appendix B). Sample 670 contains fine sand with little to no clay. Sample 740 consists of more clay, while a silty sand fraction is also present. The color of this sample is darker compared to 670. Finally, sample 760 is characterized as fine sand again. The color is lighter than sample 740 and similar to 670. All samples contain mica. The glauconite and shell content could not be determined.

2.1.3 Well correlation

Correlations between wells is done via an iterative process of matching well log patterns and connecting seismic horizons between two wells. Ideally this workflow is supplemented by biostratigraphic information.

Biostratigraphy is the correlation and identification of strata based on their fossil content. Biostratigraphic units, or zones, are strata with unique fossil material (Lucas, 2021). Modern biostratigraphic interpretations provide the most reliable way of recognizing and correlating stratigraphic units between wells. Moreover, it helps determine the thickness of the targeted formation in a specific well. For the Breda Formation, it also helps distinguish between the internal GH and Diessen formations. No biostratigraphic information was available for the Breda Formation in the ZZL at the start of this thesis. Therefore, Houben (2022) analysed cuttings to determine the chronostratigraphy in the BLA-01, LSM-01 and OFL-01 wells (see Figure 2.8). His research is part of the WarmingUP project. The resulting correlation between the three wells is shown in Figure 2.9.

Fig. 2.8: Locations of the studied wells

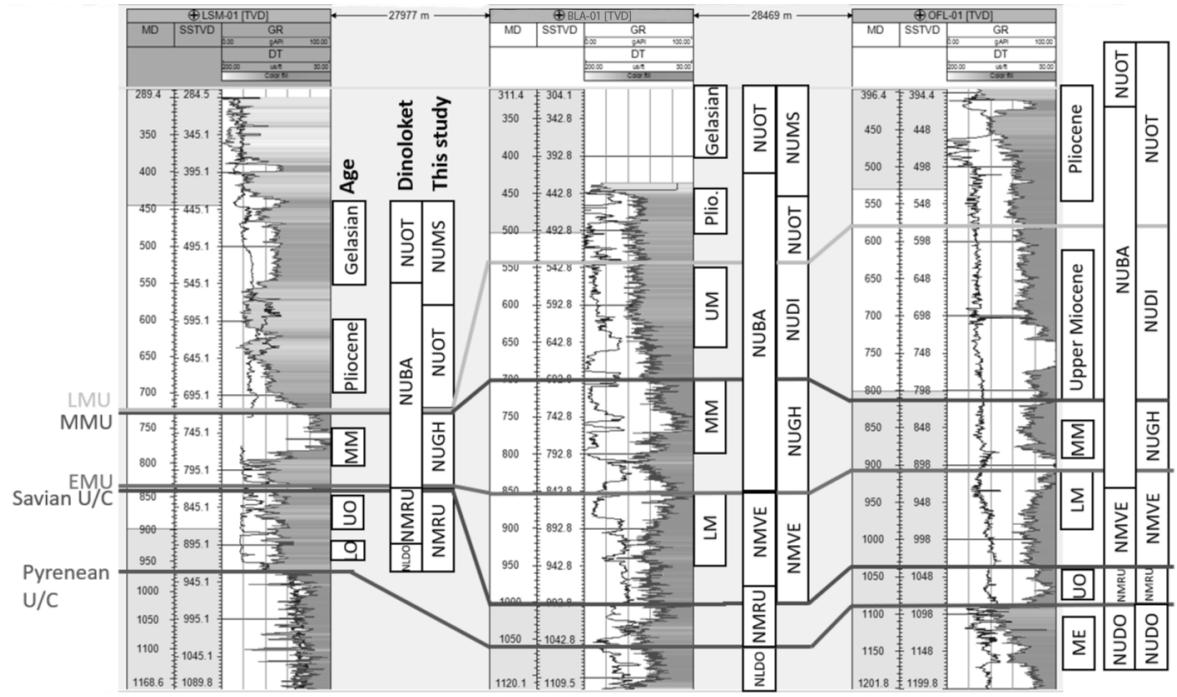

Fig. 2.9: Chronostratigraphic interpretation and corresponding well correlation for the studied wells in the ZZL. LO = Lower Oligocene, UO = Upper Oligocene, LM = Lower Miocene, MM = Middle Miocene, UM = Upper Miocene. NLDO = Dongen Formation, NMRU = Rupel Fm., NUBA = Breda Fm., NUDI = Diessen Fm., NUGH = Groote Heide Fm., NUOT = Oosterhout Fm., NUMS = Maassluis Fm. (Houben, 2022)

2.1.4 Seismic interpretation

As stated before, the REGIS model currently contains the only mapping of the Breda Formation (TNO, 2022c). However, the model is based on horizontal correlations between shallow wells, which have a very low data density in the ZZL (see Figure 2.3), and does not include seismic interpretations. In order to get a better insight in the lateral extent and thickness of the Breda Formation in the ZZL, evaluating seismic data provides the best opportunity to do so. As mentioned before in section 2.1.1, quite some seismic data are available in this region (see Figure 2.4). However, the MMU (middle) and LMU (top) have never been interpreted before in this area. Therefore, novel interpretations for these horizons are made during this thesis on all seismic lines and cubes shown in Figure 2.4. The Petrel software is used for this purpose.

The seismic data can be downloaded from the Netherlands Oil and Gas (NLOG) Portal website (TNO, 2022b). The data come in already processed format (sorted, stacked, migrated etc.). The elevation is still indicated in time, which has to be converted to depth such that the wells can be correlated to the seismics. The Velmod 3.1 open-source velocity model is used for this purpose. Velmod 3.1 can also be acquired via NLOG (TNO, 2022b).

The EMU corresponds to the base of the Upper North-Sea Group (NU), which is already incorporated in the national DGM Deep model. DGM Deep is a subsurface model on national scale developed by TNO. It includes 135 3D seismic cubes (covering almost 100,000 km^2), 577,000 km 2D seismic lines and about 5800 wells (TNO, 2019). This model does not include interpretations of the MMU and LMU yet. After evaluation, the EMU interpretation in DGM Deep proved sufficient on most seismic lines, albeit with some small corrections. The MMU and LMU are not yet included in DGM Deep. The LMU is often hard to recognize due to bad seismic quality in the shallow domain. Repeatedly, the LMU reflector couldn't be traced over the entire seismic section, leaving some distances to interpolation. In Figure 2.10, the 'SCAN42' seismic line is shown where the uncertainty encountered while interpreting the LMU is displayed.

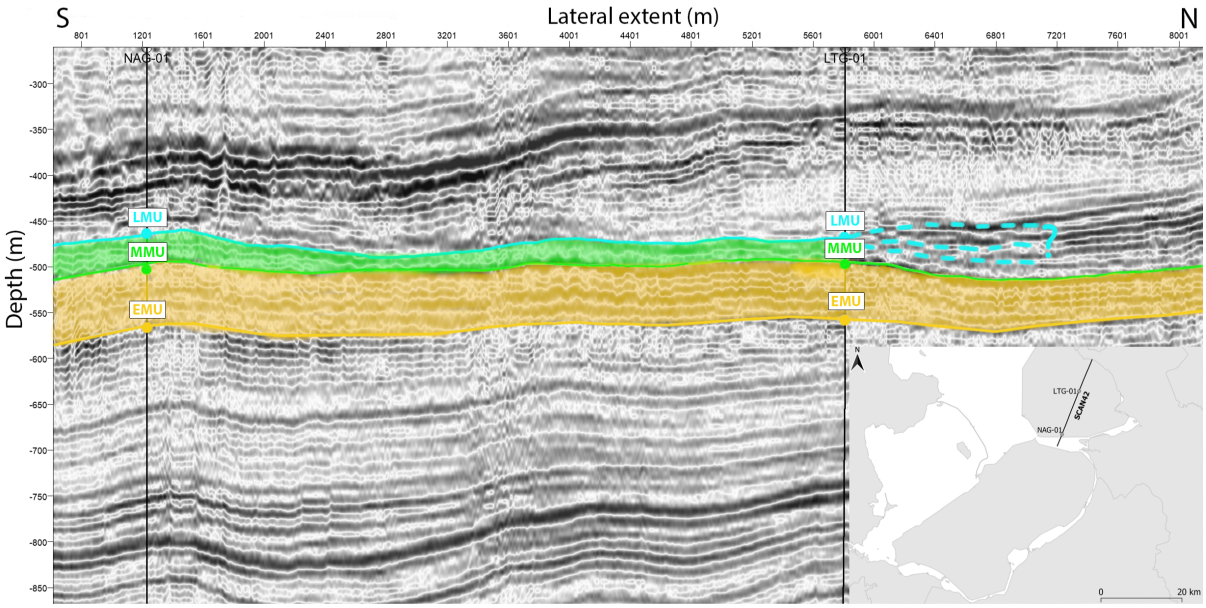

Fig. 2.10: SCAN 42 seismic line intersecting wells NAG-01 and LTG-01, with EMU, MMU and LMU interpreted. The Diessen Formation is shown in green, the Groote Heide Formation in orange. Due to bad seismic quality in the shallow domain, the LMU is sometimes hard to interpret, as shown in the figure

Based on a combination of biostratigraphy, well log patterns and the previously interpreted NU base from the DGM Deep model, reflectors were selected which most likely represent the EMU, MMU and LMU stratigraphic horizons. Additionally, since the horizons are unconformities this could sometimes be seen on the seismic images in the form of onlap or toplap. Figure 2.11 shows the 'NAM deep' seismic line, reprocessed within the SCAN project, with interpreted EMU, MMU and LMU. In the figure, onlapping reflectors on the EMU, MMU and LMU can be seen, clearly indicating the unconformable nature of these horizons.

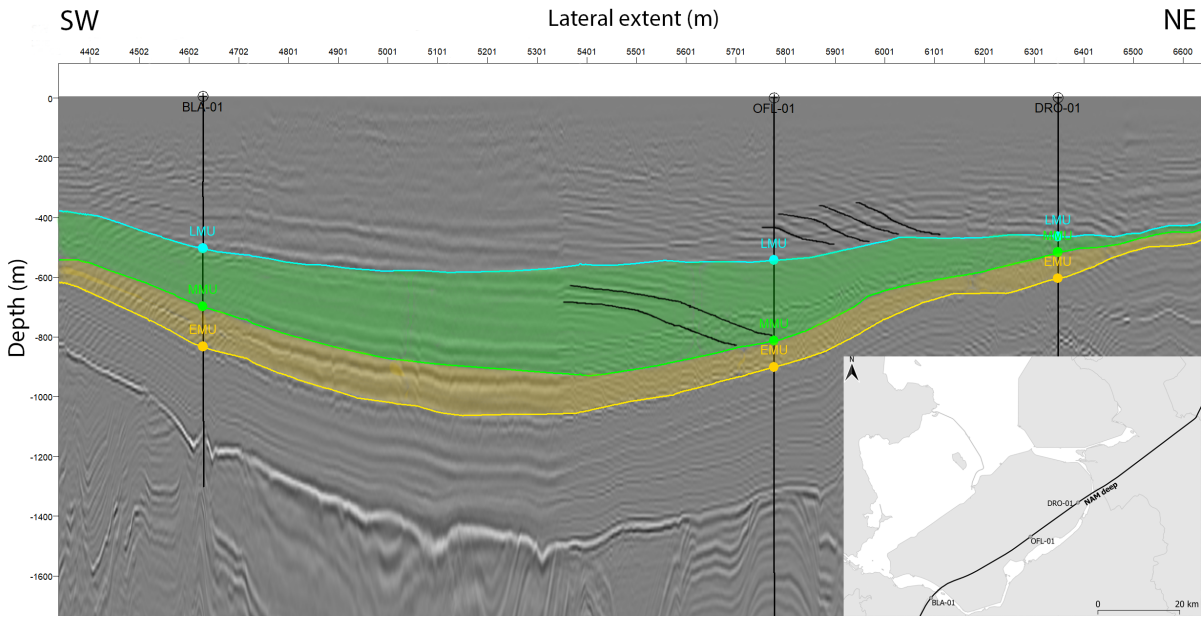

Fig. 2.11: NAM Deep seismic line intersecting wells BLA-01, OFL-01 and DRO-01, with EMU, MMU and LMU interpreted. The Diessen Formation is shown in green, the Groote Heide Formation in orange. Dipping reflectors which onlap onto the LMU and MMU can be noticed, indicated in black

Lastly, from the interpretations three 3D depth-surfaces are generated (see Results section: section 2.2). The build-in convergent algorithm in Petrel is used to interpolate between the seismic interpretations. The lateral extent of the surfaces is delimited by a polygon, whose geometry is based on the basin margins. The basin seems to continue towards Apeldoorn in the SE, however the seismic data become dispersed and of low quality in this area, hence the boundary is placed here. The surfaces show the depth variations of the three horizons. By consequently subtracting the bottom horizons from the overlying ones, three thickness maps are generated, showing the Diessen, GH and total thickness. Additionally, the generated surfaces are used as boundaries for the static reservoir model.

2.1.5 Petrophysics

Analysing well log data provides one of the best methods to make predictions on the reservoir potential of the Breda Formation. Fortunately, multiple wells have been drilled through the Breda succession, shown in Table 2.2. Despite the fact that some logs were acquired in the Breda interval, to our knowledge these petrophysical data have never been analysed so far.

Modern and standardized petrophysical methods primarily focus on deep, hydrocarbon bearing formations. Few prior petrophysical studies on unconsolidated, shallow formations are aimed at shallow gas-saturated sediments in general (e.g. Bokarev et al., 2021; Buckley and Cottee, 2017) or more specifically at shallow gas in the Dutch offshore (e.g. Sens, 2010; Ten Veen et al., 2013). Only Geel and Foeken (2021) performed an extensive petrophysical evaluation of the onshore shallow Brussels Sand Member (BSM) for geothermal exploitation. Even though the Breda Formation and BSM both appertain to the 'medium deep interval', they are not the same. The main differences are higher glauconite content in the Breda Formation, low permeability streaks in the BSM and the larger burial depth of the BSM. Also, the log data availability in the BSM is larger compared to the Breda. Furthermore, in many cases the well log data in shallow formations are disturbed due to mud type and/or logging through casing. This is especially influential on gamma ray logs. The available data sets are sparse, since for most wells only limited logs were ran through 'uninteresting' shallow formations. Most wells are also quite old, being drilled in the 60s, 70s and 80s. Moreover, no core measurements are available to calibrate petrophysically derived porosity and permeability. Cores were rarely acquired due to low interest in shallow formations and also the difficulty of coring loose sediments.

In this section, the methods used to perform the petrophysical study on the Breda Formation in the ZZL are discussed, as well as the corrections and calibration which had to be made on the disturbed data sets. Key rock properties such as clay volume, porosity, permeability and net sand are calculated, eventually leading to a static reservoir model. All petrophysical calculations are performed in Python. The Python scripts can be found in Appendix D.

Gamma ray correction and clay volume

As seen in Table 2.2, the majority of the logs acquired in the ZZL were gamma ray (GR) logs. GR logs are used to define lithologies and correlate zones by measuring the natural radioactivity in formations. Carbonate rock and 'clean' sandstones (sandstones with limited shale content) have low radioactive material concentrations and therefore provide low gamma ray measurements. Shales on the other hand contain an abundance of radioactive elements, which makes the gamma ray log response increase as shale content increases. Potassium feldspars, micas, glauconite and/or uranium-rich fluids also emit gamma rays and could be present in the matrix of a 'clean' sandstone (Asquith et al.,

2004), which results in a high apparent API reading from the GR tool. As described in section 1.4.1 and shown in section 2.1.2, the Breda Formation contains an abundance of glauconite minerals.

Other factors that have a large influence on the GR response are drilling mud type, borehole size, (ec-)centered tools, logging through casing (LTC) and the logging method (wireline or MWD) (Geel et al., 2022). Corrections for borehole size and (ec-)centered tools are usually carried out by the service company, however disturbances due to drilling mud and LTC are more challenging.

Tertiary formations in the ZZL are largely unconsolidated and contain large portions of soft, shaley layers, causing instability in the wellbore during drilling (Geel & Foeken, 2021). Drilling companies try to counterbalance these instabilities by implanting the casing as soon as possible. Wireline logging through the casing is then done afterwards, since MWD was rarely used in older wells. LTC has a detrimental effect on the GR response, since the rays recorded originate not from the formation but from the completion cement (Geel & Foeken, 2021). Wells where LTC was done are the KGB-01, LTG-01 and MKO-01. Well logs from these three wells are excluded from the petrophysical analysis since no correction is possible on them. Another method drillers use to maintain stability is injecting dense drilling fluids, like KCl polymer mud. Potassium-muds contain a radioactive isotope that emits gamma rays, contributing to the GR tool response (Cox & Raymer, 1977). The GR tool, however, does still measure the formation's own GR emission. Assuming the potassium-mud has a homogeneous effect on the GR along the borehole, a correction can be applied to filter out this effect, which should result in a more realistic GR reading.

The GR correction workflow used here is as follows. Table 2.2 shows the drilling mud used per well. From this table, 'trusted' wells are selected with non-potassium drilling mud and open-hole logging, acting as reference wells. Other wells with a disturbed GR log in the vicinity of the reference well can then be calibrated towards the trusted GR reading. This is done by matching the 100% sand point in the disturbed GR with the 100% sand point of the reference GR log, effectively scaling down all values in the disturbed log. The same is done for the 100% shale point. The assumption here is that no significant facies changes occur laterally. Usually, lateral facies alternations are limited in shallow marine environments, like the ZZL during the Miocene. Still, to reduce the risk reference wells are selected close to corrected wells. Figure 2.12 shows the GR log in BLA-01 before and after correction, calibrated towards the trusted GR log in ALE-01. Table 2.4 shows the reference well per region, as well as the corrected wells.

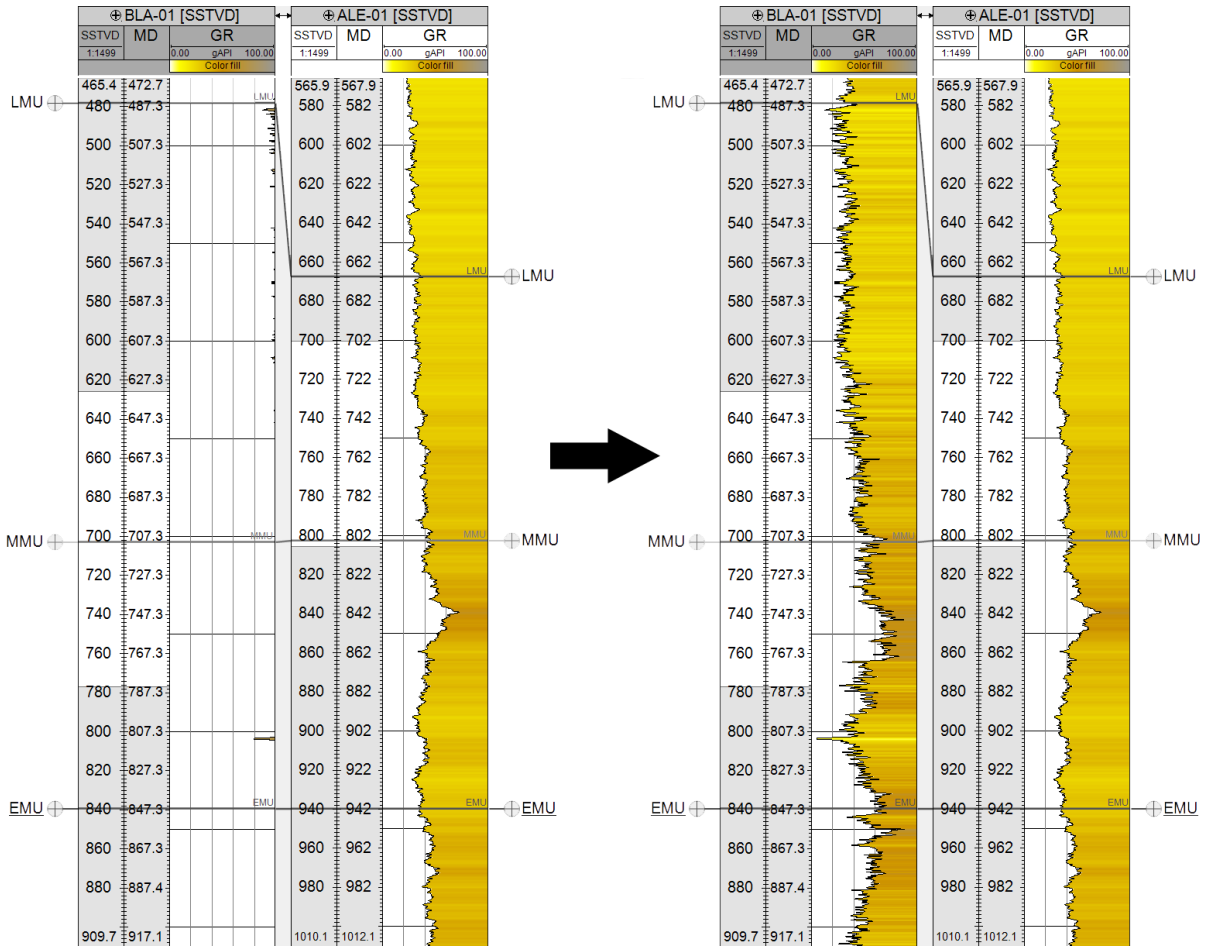

Fig. 2.12: Uncorrected GR in BLA-01 (left) and corrected GR (right), alongside trusted ALE-01 well. Note that the raw GR values in BLA-01 are mostly higher than 100 API

Tab. 2.4: Reference wells with a trusted GR log per region in the ZZL. Other wells within this region which have a disturbed GR log response are calibrated towards the trusted well

Region	Trusted reference well	Corrected well(s)
Flevoland south / Gooi	ALE-01	BLA-01
Slootdorp	SLD-01/HOK-02	MDM-GT-X, ADK-GT-X
Beemster	MID-101	WBMS-01

Clay volume
From the (corrected) GR logs, the clay volume (V_{cl}) can be derived. First, the linear Gamma Ray Index (I_{GR}) can be calculated as follows:

$$I_{GR} = \frac{GR_{log} - GR_{min}}{GR_{max} - GR_{min}} \tag{2.1}$$

where GR_{log} = the measured values from the (corrected) gamma ray log (API units), GR_{min} = the minimum GR or clean sandstone value and GR_{max} = the maximum GR or pure shale value.

Quite often a non-linear relation to correct for over-estimated clay volume is used to obtain the V_{cl} from the I_{GR}. The most used non-linear empirical corrections include the Larionov models for old and Tertiary rocks (1969), Stieber (1970) and Clavier (1971) model. Moreover, Heslop (1974) advocates to use the linear variant (I_{GR}) directly, since he demonstrated that the GR response to clay content of clastic rocks is linear for most clay minerals (Geel & Foeken, 2021). To find the optimal V_{cl} model, a sensitivity analysis can be done. By applying a range of cutoffs on the V_{cl} and plotting these against the equivalent net sand column, the 'elbow point' can be found (Geoloil, 2012). This point provides a fairly good estimation of the cutoff value that should be used. Standard V_{cl} cutoffs lie between 20% and 35%. If the elbow point indicates a cutoff value larger than 35%, the chosen V_{cl} model is most likely too 'pessimistic' (Geoloil, 2012). The 4 mentioned models and linear I_{GR} are applied to the NDN-120 well together with some cutoffs ranging from 10% to 75%. NDN-120 is chosen as demonstration well since this well has the most complete dataset (lithofacies, GR and density log, well test permeability). The results are shown in Figure 2.26 in the Results section.

The clay volume, and therefore the chosen V_{cl} model, affects the permeability. Since the (well test) permeability of the NDN-120 well is known, this provides an additional way of determining the optimal V_{cl} model. More on this matter will be discussed in the Permeability section of this chapter. Lastly, the V_{cl} cutoff value from the chosen model can be used to calculate the net sand value. More on this subject can be found in the section on net sand further on in this chapter.

Drilling mud salinity

The salinity of the drilling mud is an important factor when calculating the porosity from well logs. The density porosity and Wyllie porosity require knowledge of the mud salinity to estimate the fluid density (ρ_{fl}) and fluid transit time (DT_{fl}), respectively. The mud filtrate can be taken as the 'fluid' component in these equations, due to the limited depth of investigation of the logging equipment. The maximum investigation depth of various logs is shown in Figure 2.13. As a result, the equipment primarily records the infiltrated zone where the mud filtrate replaced the original formation water.

Table 2.5 shows the salinity values per well. The data shown in this table can be retrieved from NLOG (TNO, 2022b).

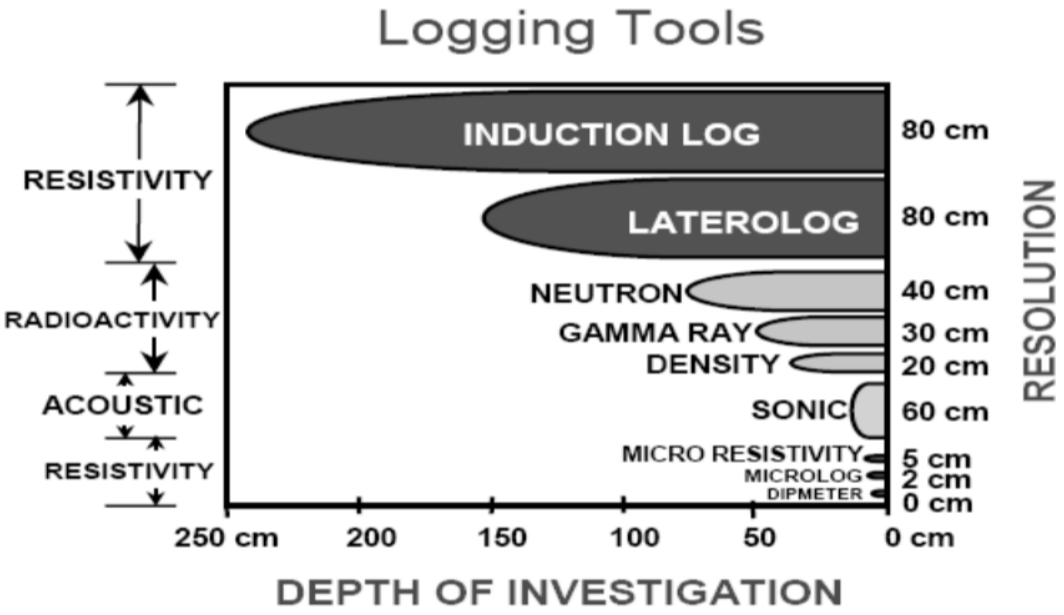

Fig. 2.13: Resolution of various logging tools (Bond et al., 2010)

Tab. 2.5: Wells with a porosity log tool (density/neutron/sonic). If salinity is known, other values are not applicable (NA). Salinity calculated from R_{mf} and T_f are indicated in *italic*

Well	Mud salinity (ppm)	Mud filtrate resistivity R_{mf} (Ohm.m)	Formation temperature T_f (°C)
ALE-01	1,000	NA	NA
BLA-01	114,000	NA	NA
DRO-01	*18,247*	0.36	19
EPE-01	190,000	NA	NA
KRD-01	900	NA	NA
LEL-01	3,000	NA	NA
LSM-01	*7,192*	1.01	13
MID-101	*4,805*	1.20	21
MID-201	*15,620*	0.45	16
NAG-01	3,000	NA	NA
NDN-120	-	-	-
OFL-01	*21,330*	0.33	17
RST-01	*14,200*	0.51	15
SLD-01	*11,085*	0.62	16
WSP-01	0	NA	NA
ZEW-01	-	-	-

Values for drilling mud salinity per well are usually documented in weekly drilling reports, retrievable on NLOG (TNO, 2022b). Not all drilling operators recorded the salinity however, or only documented the salinity in deeper parts of the well. In these cases the mud salinity can be calculated using the mud filtrate resistivity (R_{mf}) and formation temperature (T_f) (Benedictus, 2007). If documented, the R_{mf} and T_f value can also be found in the drilling reports. The resistivity equation is defined as follows (Akinsete & Adekoya, 2016):

$$R_w = \left[0.0123 + \frac{3647.5}{c_w^{0.955}}\right] \frac{82}{1.8T_f + 39} \tag{2.2}$$

which can be rearranged to solve for the salinity:

$$C_w^{0.955} = \frac{166164}{R_w T_f + 21.6667 R_w - 0.560333} \tag{2.3}$$

where C_w = salt concentration (ppm), $R_w = R_{mf}$ = the mud filtrate resistivity (Ohm.m) and T_f = formation temperature (°C).

Once the salinity is known, the corresponding fluid density or fluid transit time can be approximated. Table 2.6 relates the salinity values to fluid density and fluid transit time, based on publications by Lyons (2010) for fluid density and Carmichael (1982) for fluid transit time. For wells NDN-120 and ZEW-01, neither mud salinity nor filtrate resistivity and formation temperature were documented. For these wells, fresh drilling fluids are assumed to be conservative.

Tab. 2.6: Table used to approximate the fluid density (after Lyons, 2010) and fluid transit time (after Carmichael, 1982) from drilling mud salinity values

Mud salinity (ppm)	ρ_{fl} (g/cm^3)	DT_{fl} (µs/ft)
0-50,000	1.0	218-213
50,000-100,000	1.03	213-208
100,000-150,000	1.07	208-200
150,000-200,000	1.11	200-189
200,000-250,000	1.15	189-180
250,000-300,00	1.19	180

Porosity

Porosity is that portion of a rock that is not occupied by solid material. It's defined as the percentage of the total volume taken up by pore space, ranging between 0 and 1 (Nimmo, 2013). Effective porosity is the portion of total volume only including interconnected pores which aren't isolated by solid particles.

A porosity tool was used in 15 wells within the Breda formation in the ZZL area (see Table 2.5). Well logs from which porosity can be calculated are the sonic, density and neutron logs. Most preferably, a density-neutron log pair is used. If a neutron log is absent, the porosity is calculated from the density log only. When both the neutron and density logs are not acquired, the sonic log is used. All available logs per well are listed in Table 2.2.

Porosity from density log
In the ZZL, 6 wells contain a (partially complete) density log (see Table 2.2). From these measurements, a porosity estimate can be calculated:

$$\phi_\rho = \frac{\rho_{ma} - \rho_b}{\rho_{ma} - \rho_{fl}} \tag{2.4}$$

where ϕ_ρ = density porosity (cm^3/cm^3), ρ_{ma} = matrix density which is initially guessed at 2.65 g/cm^3 (quartz density), ρ_b = measured bulk density from the log (g/cm^3) and ρ_{fl} = fluid density (g/cm^3).

When the clay volume is known, a clay correction term can be added to Equation 2.4 to determine the effective porosity:

$$\phi^e_\rho = \frac{\rho_{ma} - \rho_b}{\rho_{ma} - \rho_{fl}} - V_{cl}.\frac{\rho_{ma} - \rho_{sh}}{\rho_{ma} - \rho_{fl}} \tag{2.5}$$

where ρ_{sh} = shale density (g/cm^3), which can be determined from the density log in the underlying shale formation.

Porosity from density-neutron log pair
A more reliable method for determining the total and effective porosity is by combining the density log with a neutron porosity log. Three wells in the ZZL have such a full log suite (see Table 2.2). First the density porosity must be calculated, using Equation 2.4. The density porosity, bulk density and neutron porosity are then plotted on the left y-axis, right y-axis and x-axis respectively (see Figure 2.14). Consequently, the dry clay point, wet clay point and corresponding lines are added following the procedure used by Kurtz (2013). A correction for clay content is applied to all points by subtracting the V_{cl} from the original density and neutron porosity, multiplied by the wet clay point:

$$\phi_{\rho,\text{clay corrected}} = \phi_\rho - V_{cl}(\phi_{\rho-\text{ wetclay}}) \tag{2.6}$$

$$\phi_{N,\text{clay corrected}} = \phi_N - V_{cl}(\phi_{N-\text{ wetclay}}) \tag{2.7}$$

where ϕ_N = neutron porosity (m^3/m^3). Points which end up above the clean quartz line after correction are influenced by the 'gas effect'. These points are corrected by projecting them onto the clean quartz line along a line with a slope of 0.667 (Kurtz, 2013). By then projecting each (clay & gas corrected) point parallel to the wet clay fraction line on to the clean quartz line, the effective porosity can be determined.

After evaluation, the data from the LSM-01 well are not included in this study. The caliper log from this well shows sections with unusually large borehole diameters in the Breda Formation interval. This phenomenon indicates borehole washouts. Washouts can occur during drilling when drilling through soft or unconsolidated formations. Running a neutron-density log suite through such an interval is problematic, since the maximum investigation depth of the neutron and density tool is roughly 75 and 40 cm, respectively (Bond et al., 2010). Therefore, in a washed out zone the logs will measure only the drilling mud instead of the actual formation, resulting in unusable measurements (Ugborugbo & Rao, 2009).

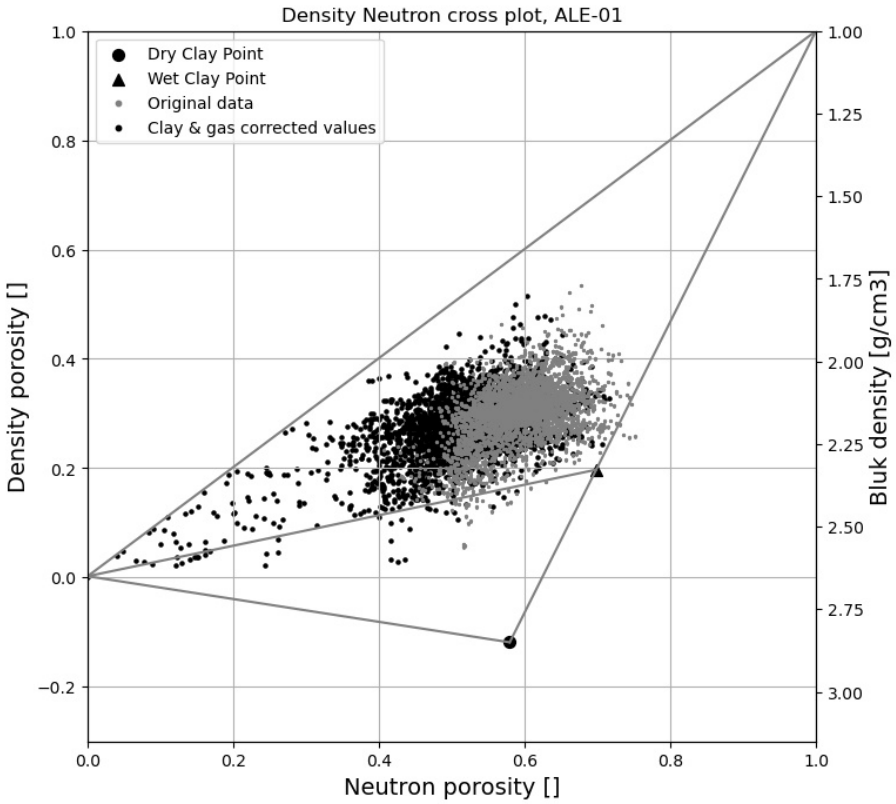

Fig. 2.14: Density-Neutron cross plot from ALE-01

Porosity from sonic log

As shown in Table 2.2, most wells don't have a density or neutron log. However, 9 of them do have a sonic log from which the porosity may be estimated. Wyllie et al. (1956) proposed a time-average formula for this purpose:

$$\phi_{son} = \frac{DT - DT_{ma}}{DT_{fl} - DT_{ma}} \tag{2.8}$$

where ϕ_{son} = Wyllie (sonic) porosity (m^3/m^3), DT = transit time measurements from the log (µs/ft), DT_{ma} = matrix transit time for which the standard quartz value of 56

μs/ft is used (Geel & Foeken, 2021) and DT_{fl} = fluid transit time (μs/ft).
Similar to Equation 2.5, an additional term can be added to account for the clay content:

$$\phi^e_{son} = \frac{DT - DT_{ma}}{DT_{fl} - DT_{ma}} - V_{cl}.\frac{DT_{sh} - DT_{ma}}{DT_{fl} - DT_{ma}} \tag{2.9}$$

where DT_{sh} = shale transit time (μs/ft) which can be determined from the sonic log in the underlying shale formation.
The Wyllie formula tends to overestimate the porosity in unconsolidated formations due to longer transit times, compared to consolidated formations (Schlumberger, 1989). The compaction factor (C_p) can be used to correct for this. C_p is estimated by dividing DT_{sh} by the transit time of compacted shale (Equation 2.11).

$$\phi^e_{son} = \left(\frac{DT - DT_{ma}}{DT_{fl} - DT_{ma}} - V_{cl}.\frac{DT_{sh} - DT_{ma}}{DT_{fl} - DT_{ma}}\right).\frac{1}{C_p} \tag{2.10}$$

$$C_p = \frac{DT_{sh}}{DT_{csh}} \tag{2.11}$$

where DT_{csh} = compacted shale transit time, which is equal to 100 μs/ft (Geel & Foeken, 2021).

Porosity validation and correction

Unfortunately, no core porosity measurements are available in the Breda Formation. Therefore porosity from well logs can't be directly validated. The only way of roughly validating the well log porosity is by comparing it to values from literature. This way any outliers can be identified and removed. Taheri et al. (2017) lists a few different authors who calculated porosity in random packings of spherical particles, representing unconsolidated homogeneous sands, generated by computer simulation algorithms. The highest simulated porosity was 48% by Scott (1960). This value is taken as the absolute maximum allowed porosity from the well logs, after all corrections are applied (clay volume, compaction, gas effect). Any value higher than this is considered as flawed and is excluded from the model. As an example, in Figure 2.15 porosity values of up to 75% are filtered out in the WSP-01 well. Furthermore, any porosity value below 0.0% is set back to 0%.

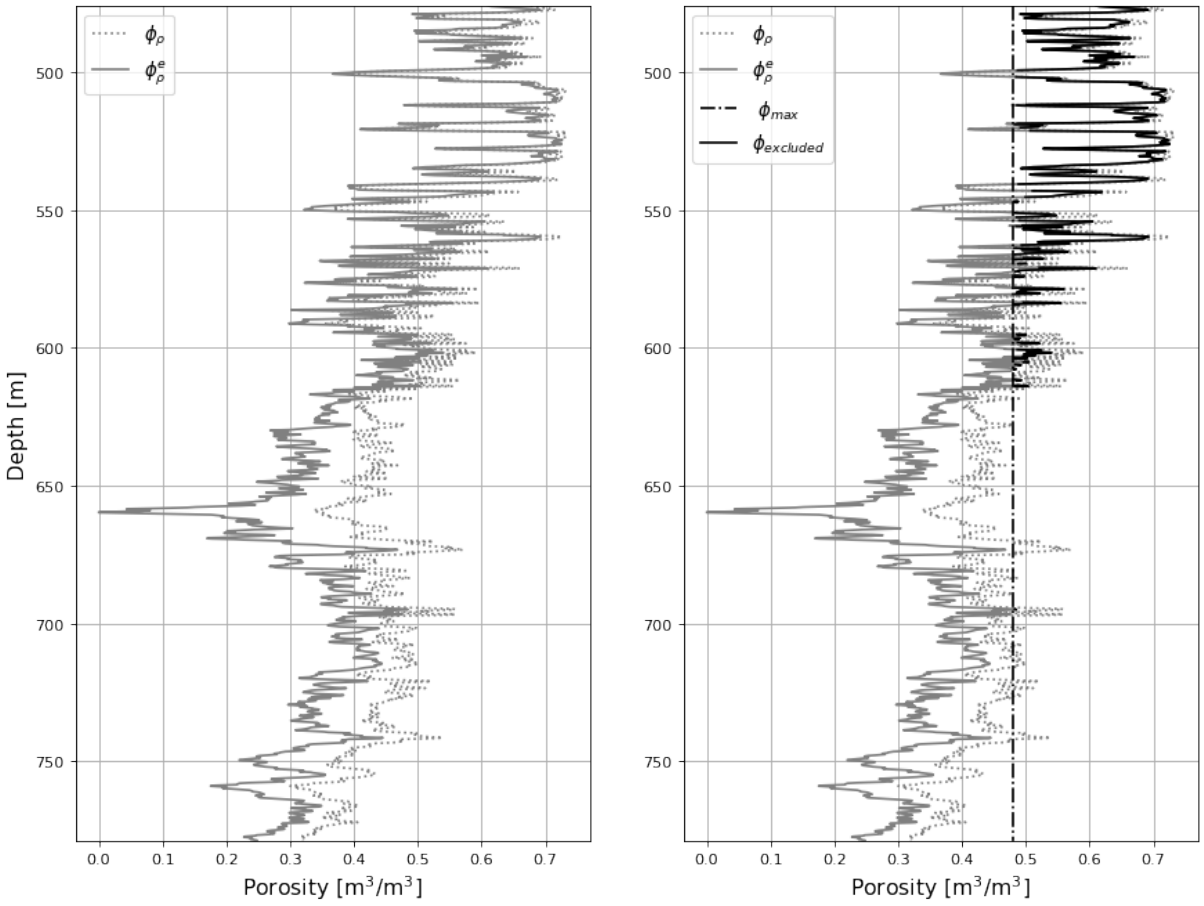

(a) Unfiltered effective porosity **(b)** Filtered effective porosity

Fig. 2.15: Porosity calculated from density log in WSP-01

Permeability

Permeability is a measure of how easily a fluid can flow through a certain medium. This property is usually derived from porosity and grain size, sometimes including other parameters as well. Many permeability equations exist, all with different strengths and weaknesses. In the *Permeability validation* section below, selected permeability equations are tested on the NDN-120 well. From this analysis, the Kozeny-Carman (K-C) equation (Equation 2.12) appears as best-suited for this well, based on the known well test permeability. A couple of assumptions are considered for this equation: The porous medium consists of a bundle of capillary tubes, all with equal length. Flow of fluid is Darcian and the fluid is Newtonian and incompressible. Lastly, velocity components normal to the tube axes are not taken into account (Taheri et al., 2017).

$$\kappa_{\text{K-C}} = \psi_{\text{s}}^2 \frac{\phi^3 D_{\text{p}}^2}{150(1-\phi)^2} \tag{2.12}$$

where D_p = grain diameter (m), ϕ = porosity (m^3/m^3) and ψ_s = grain sphericity. Sphericity is measured between 1 and 0, where 1 stands for a perfect sphere.

The sphericity of sand grain in a porous medium is an important factor for fluid flow. Angular grains are more likely to prohibit flow by blocking off pore throats, since multiple points of contact with other grains are possible. In contrast, a perfect spherical grain can only have one point of contact with a neighbouring grain, leaving more open space for fluid flow. The data on sphericity for the Breda Formation are very limited. Slupik and Janse (2008) mention a general (sub-)angular trend in the Colijnsplaat borehole in the province of Zeeland, however this is quite far away from the area of interest. Sediments found in the ZZL could have traveled a longer distance, making them more spherical. In the cutting analysis section (section 2.1.2), sphericity determined for grains found in the ADK-GT-01 cuttings has a value between 0.5 - 0.7 (see section 2.2.1). Furthermore, Rorato et al. (2019) tested two rock specimens: one with larger, well rounded grains and one with smaller, angular shaped grains. The latter (Hostun specimen) is chosen as analogue for the Breda Formation, since this specimen seems to resemble the grains from the cutting analysis. The average operational sphericity is therefore assumed to be 0.58.

A few records of grain diameter (D_p) are available. The sand median was recorded in 3 wells penetrating the Breda Formation in the ZZL. Additionally, cuttings are analysed for this thesis from the ADK-GT-01 well, as shown in section 2.1.2. The available grain size data are summarized in Table 2.7. All recorded values are plotted versus depth, shown in the Results section (see Figure 2.28). The average sand median line shown in Figure 2.28b is used as input for D_p in Equation 2.12.

Tab. 2.7: Sand median values from the Breda Formation

Well	Depth (m)	Sand median (μm)	Classification	Source
NDN-120	398-548	125-75	Fine to very fine	RGD (1974)
BKN-01	401-436	70	Very fine	Deelder (1977)
HIL-01	430-451	80	Very fine	Deelder (1977)
ADK-GT-01	690-840	74-50	Very fine	Cutting analysis (section 2.1.2)

Permeability validation and sensitivity analysis
Usually, permeability calculated from well logs is validated by lab-derived measurements on cores and cuttings. Since these kinds of measurements are not available, the next best option is using well test permeability. Only one well test was done on the Breda interval, in the NDN-120 well. The recorded permeability was 270-290 mD over a 400-500 m depth interval (Deelder, 1977).

Kuanyu Lin (2021) compared multiple permeability determination methods applied on cuttings samples from the Brussels Sand member. From this study, the Alyamani & Sen (1993), van Baaren (1979), Barr (2001), Kozeny (1927) and Krumbein & Monk (1943) equations came out as best methods for all permeability intervals. Alyamani & Sen and Krumbein & Monk relate permeability solely to grain size measurements. These two equation are not used in this situation, since abundant and accurate grain size measurements are infrequent in the Breda Formation. The remaining three equations relate permeability to grain size as well as porosity:

$$\kappa_{\text{Baaren}} = 10 \times d_{dom}^2 \times C^{-3.64} \times (m + 3.64) \times \phi^{m+3.64} \tag{2.13}$$

$$\kappa_{\text{Barr}} = \frac{1}{(36)5C_s^2} \times \frac{\phi^3}{(1-\phi)^2} \times d_{10}^2 \tag{2.14}$$

$$\kappa_{\text{Kozeny}} = 5.53 \times d_{10}^2 \times \frac{\phi^3}{(1-\phi)^2} \tag{2.15}$$

where d_{dom} = dominant grain size (μm) in formation, m = cementation factor (1.4 for unconsolidated formations), C_s^2 = sphericity factor (1 for spherical grains and 1.35 for angular grains), d_{10} = grain size (μm) corresponding to 10% of smallest grain sizes in formation and C = sorting factor (0.7 for well sorted grains). Well sorted grains are assumed based on the cutting analysis (section 2.1.2).

Since the NDN-120 well is the only well with a reference well test permeability, the permeability in this well is calculated via the mentioned methods to verify the optimal one. Furthermore, in the clay volume section, a few different V_{cl} models are applied to the

GR log from the NDN-120 well. These models also need to be taken into consideration, since the permeability is sensitive to the V_{cl} and therefore the chosen model. The Larionov Tertiary and Stieber models both result in a reasonable V_{cl} cutoff. Therefore, the permeability is calculated using these two models for each of the four permeability methods, resulting in a total of 8 permeability 'candidates' (see Figure 2.27). The mean permeability and standard deviation per method and model are shown in Table 2.8.

The combination which is on average the closest to the well test permeability and has the lowest standard deviation, is applied to all other wells with porosity logs to calculate the permeability. Which one this is, is shown in the Results section (section 2.2.3).

Net sand

Net sand, net to gross or net reservoir, in terms of geothermal exploitation is defined as the portion of the gross rock volume (GRV) that contains produceable water. It can be calculated by applying cutoffs on the clay volume and porosity. From the clay volume and permeability sections it could be determined that the Stieber model with a V_{cl} cutoff of 35% should be applied to NDN-120 well (see section 2.2.3). This workflow is then extrapolated to all 15 wells with porosity logs. The resulting cutoff point is shown in Figure 2.29 and Figure 2.30.

The next step is determining the porosity cutoff. An increasing cutoff value is applied to the calculated effective porosity of all 15 wells. Simultaneously, the V_{cl} cutoff of 35% is still enforced. Therefore, the net sand value on the y-axis will not start at 100% for 0% cutoff (see Figure 2.31). Again, the elbow point can be found, showing the porosity cutoff value.

Transmissivity

The transmissivity is the combination of permeability and net thickness. Transmissivity is convenient to determine since it provides a combined 2D map view of these important properties. It is calculated by multiplying the permeability by the total thickness and net to gross. The unit of transmissivity is therefore defined as Dm (Darcy multiplied by meter). See section 2.2.3 for the resulting map.

2.1.6 Static model

A static geomodel is the numerical representation of a geologic body, usually consisting of 3D grid cells. The geometry of the geomodel is defined by the top and bottom surfaces (LMU and EMU). Each grid cell can be populated with petrophysically derived reservoir properties:porosity, permeability and net sand.

Well log upscaling

The vertical resolution of well logs is about 1 to 80 cm (see Figure 2.13), while the typical vertical length of a grid cell in a geomodel is one or two orders of magnitude larger. To populate the static model with petrophysical properties, the values must be 'upscaled' by averaging over the cell height. Clearly, a lot of detail will be lost in the upscaling process, however for computational purposes this is a necessary step. Sub-units Diessen and Groote Heide are each vertically subdivided in 5 grid cells. Arithmetic averaging is used to upscale the porosity, permeability and net sand values within one cell.

3D interpolation

The next step in the static model building workflow is interpolation between upscaled well logs. For this purpose, kriging interpolation is used. Kriging is a spatial interpolation method that estimates the value of a variable over a continuous geographic field using a small number of sampled data points. The points close to the place of interest are given greater weight than those farther away when calculating the kriging weights. First the covariance is determined spatially of the sampled points by fitting a variogram. Secondly, weights resulting from the covariance are utilized to interpolate values spatially for unsampled locations. This interpolation method returns a 'heat map' style output, which is sufficient if the data density is low (as is the case in the ZZL).

2.2 Results

In this section, the results from the reservoir characterization study can be found, mostly in the form of maps and figures.

2.2.1 Results cutting analysis

The general sphericity from the ADK-GT-01 cutting samples is determined to be between 0.5 and 0.7. The grains are well sorted. Figure 2.16 shows the glauconite and shell contents of every sample taken in the ADK-GT-01 well, as well as the 'high GR interval'. Trend lines are fitted through the data points.

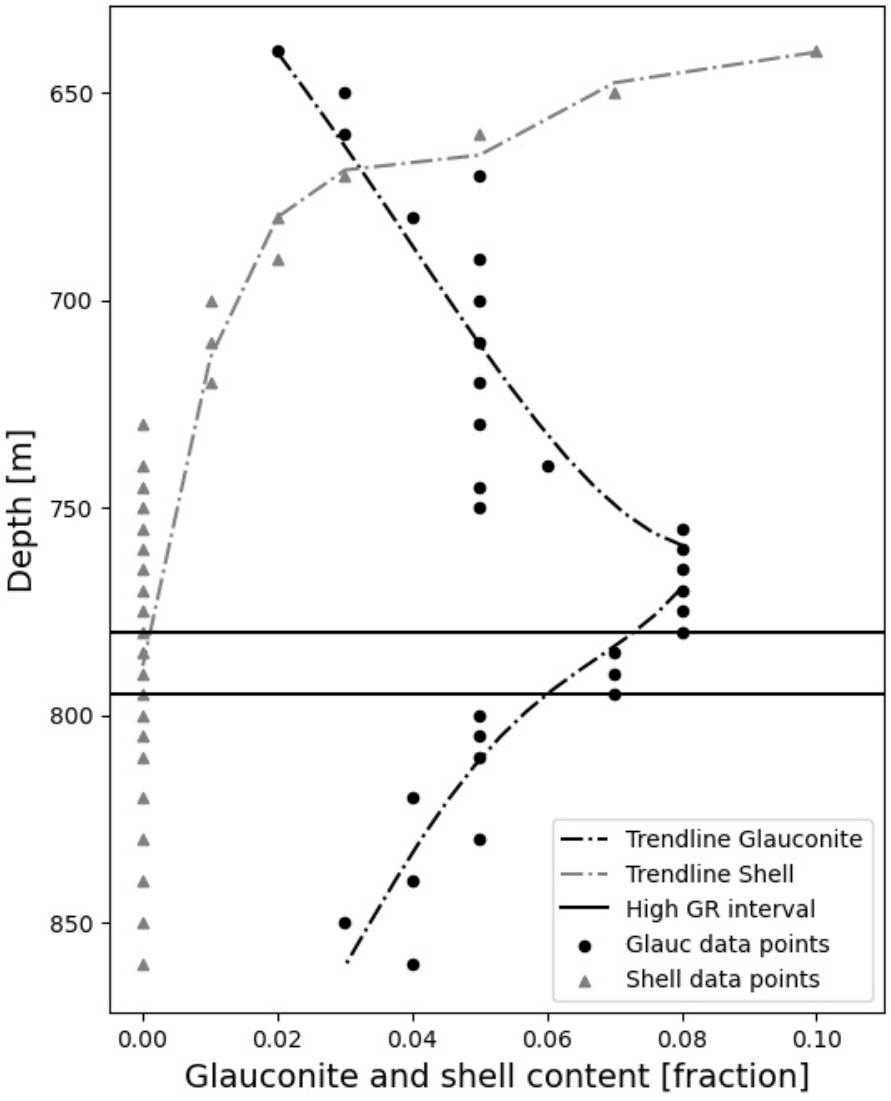

Fig. 2.16: Glauconite and shell content from ADK-GT-01 cuttings, plotted versus depth

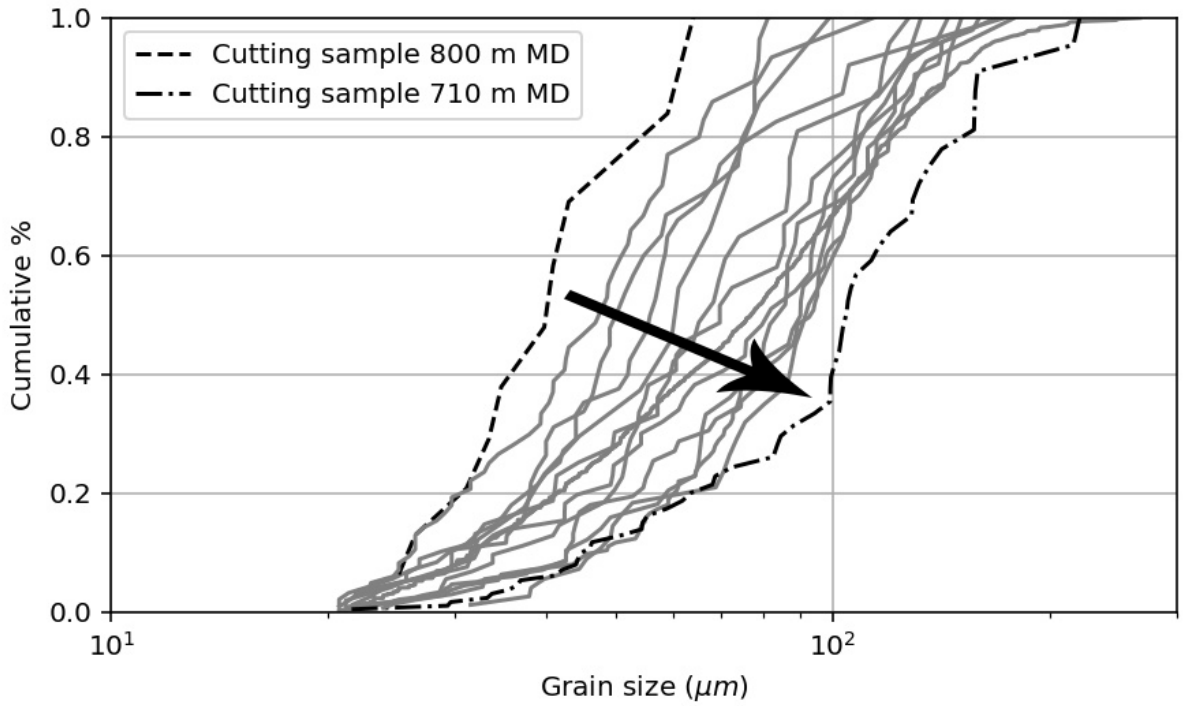

Fig. 2.17: Grain size distribution from ADK-GT-01 cuttings between 710 and 840 m MD, shown at every 10 m. The arrow indicates the average increase in grain size towards the top

2.2.2 Results seismic interpretation

The results from the seismic interpretation study are shown alongside current interpretations in the REGIS model.

When put in sequence from old to young, the depth maps of the EMU, MMU and LMU show a migration of the deepest part towards the NW. This phenomenon indicates that the coast line was building out and the depocenter migrated towards the NW during time of deposition. This discovery is in compliance with the earlier mentioned statements (see section 1.4.1) by Geluk et al. (1994) and Munsterman and Brinkhuis (2004) on the NW progradation of the paleo-Rhine delta and consequent movement of the depocenter towards the North Sea Basin.

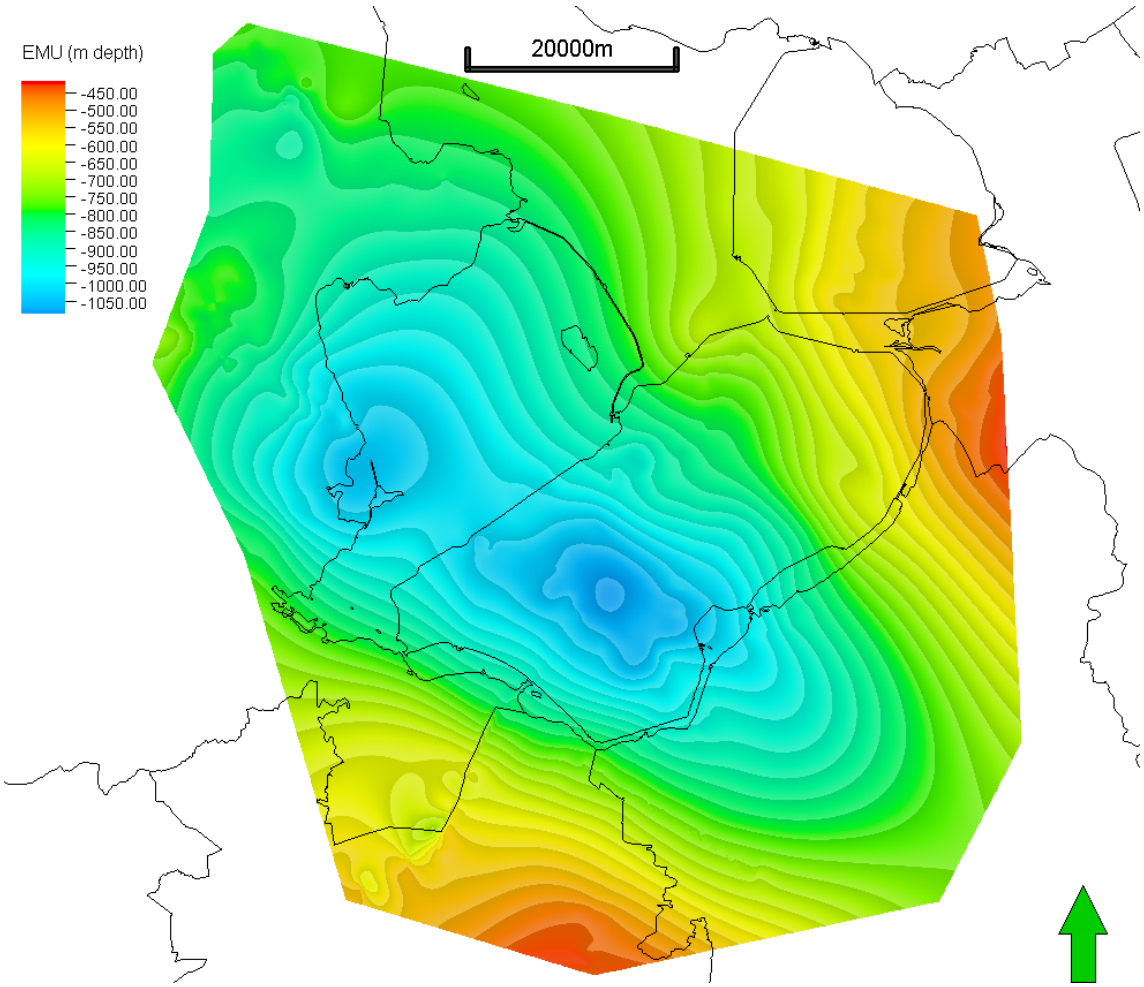

Fig. 2.18: Base of the Breda Formation, corresponding to the Early Miocene Unconformity

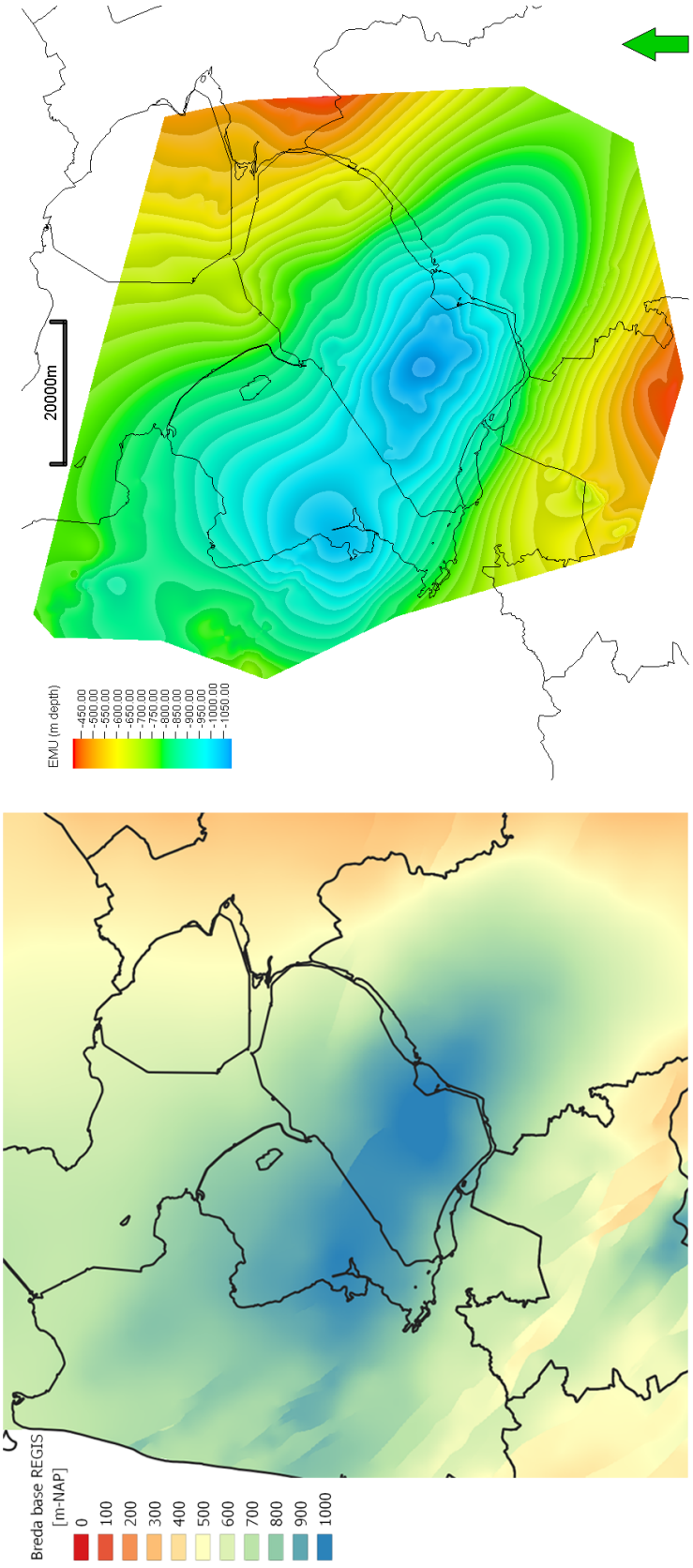

Fig. 2.19: Base of the Breda Formation in the REGIS model next to the resulting EMU surface from this study

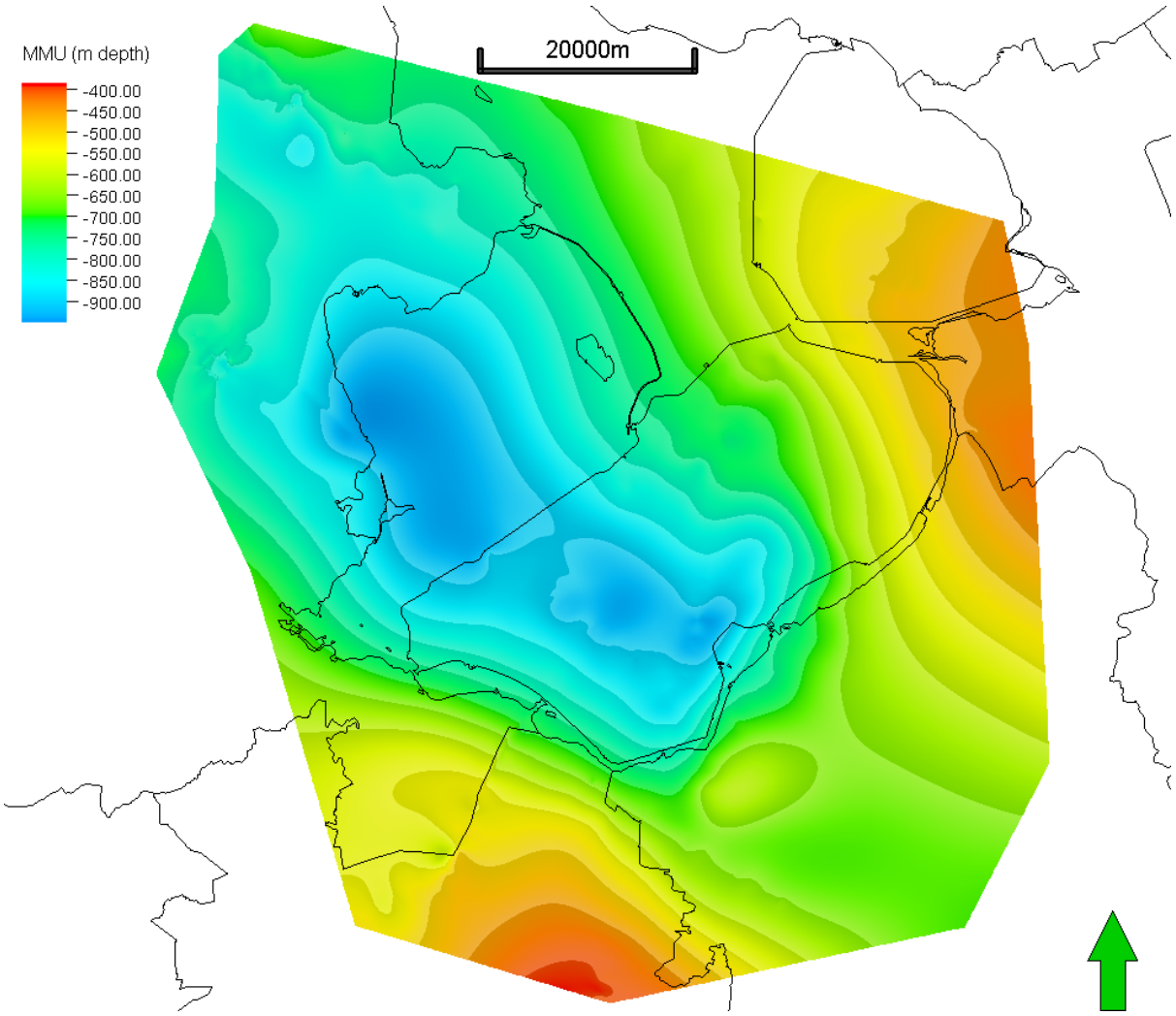

Fig. 2.20: Mid-Miocene unconformity separating the Breda Formation into Diessen and GH

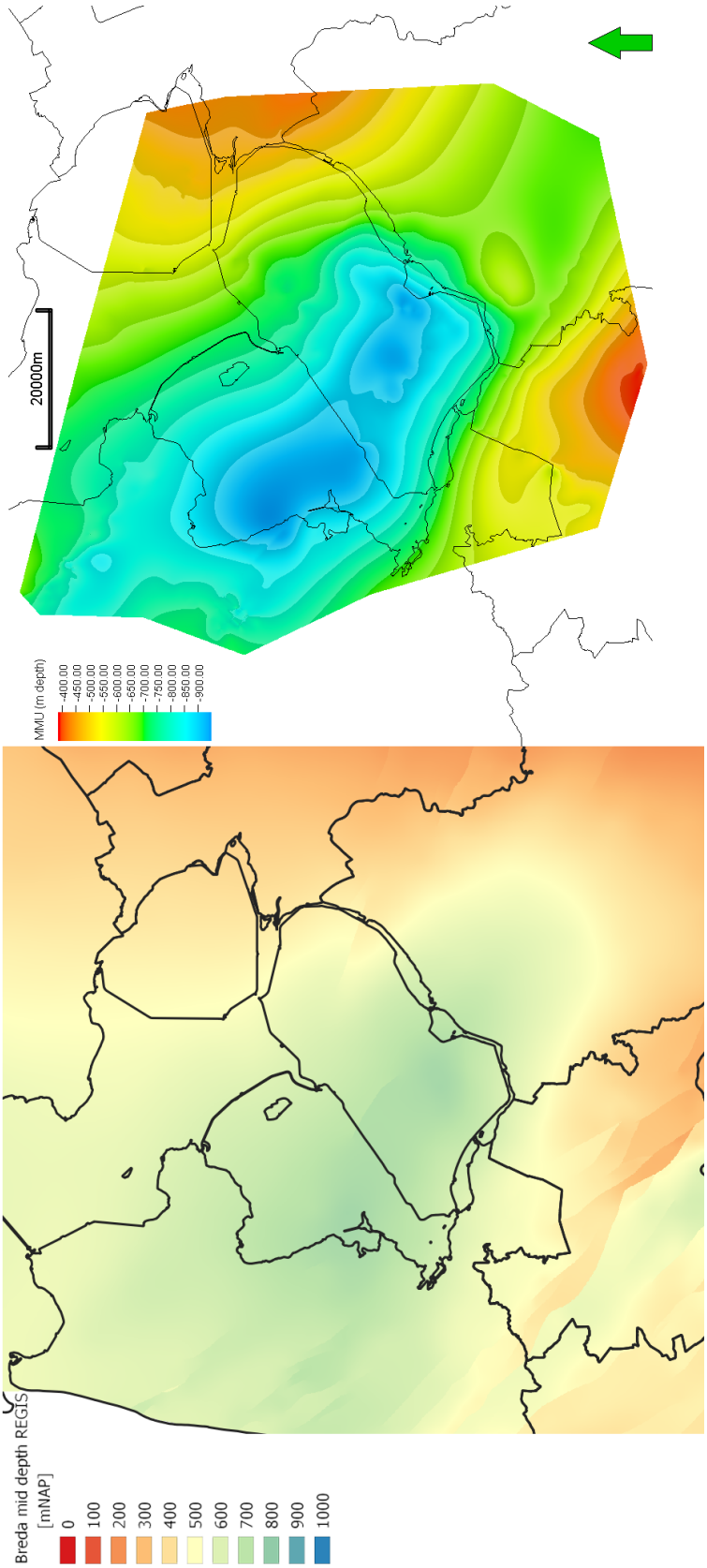

Fig. 2.21: Middle of the Breda Formation (separating Diessen and GH) in the REGIS model next to the resulting MMU surface from this study

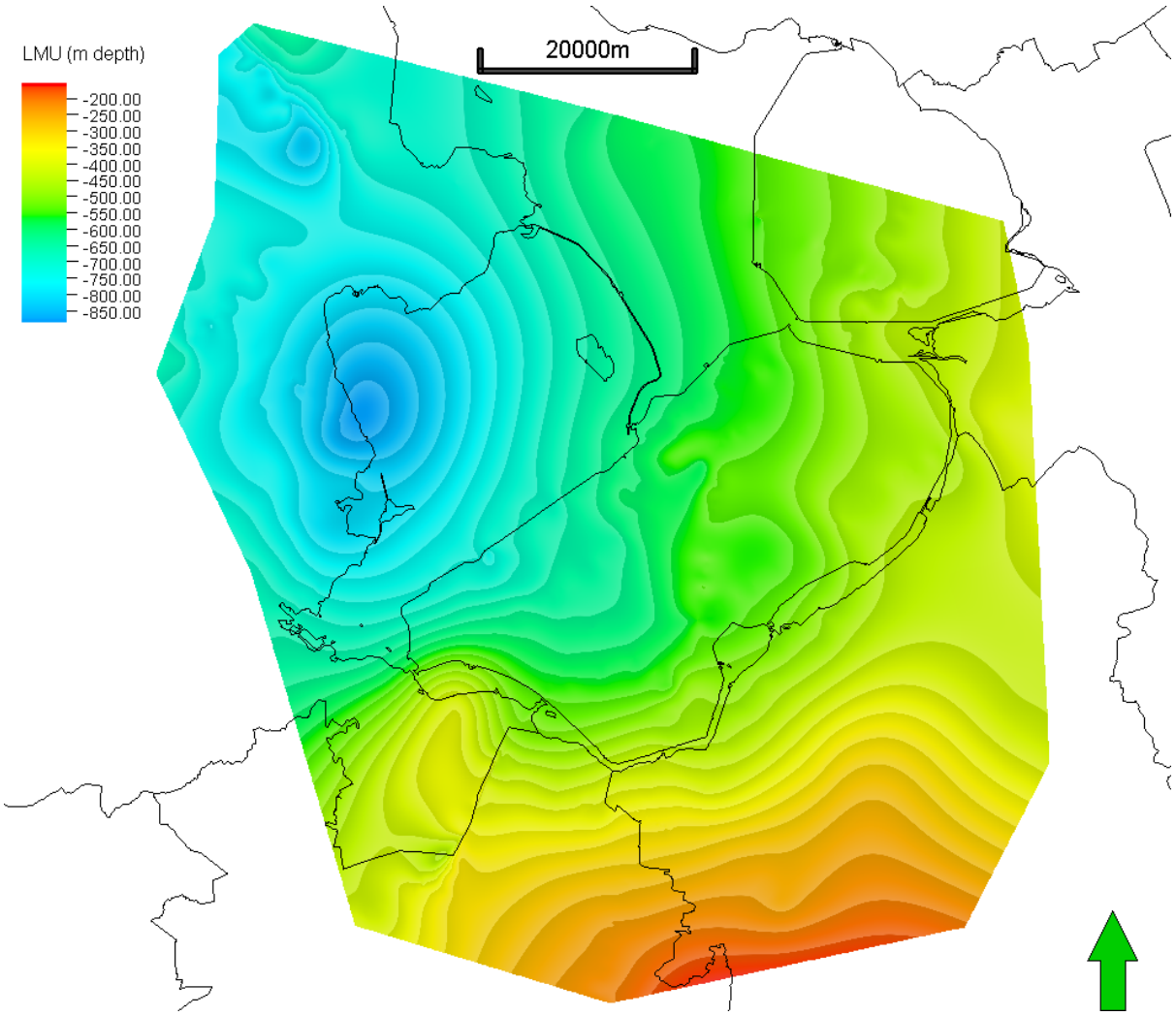

Fig. 2.22: Top of the Breda Formation, corresponding to the Late Miocene Unconformity

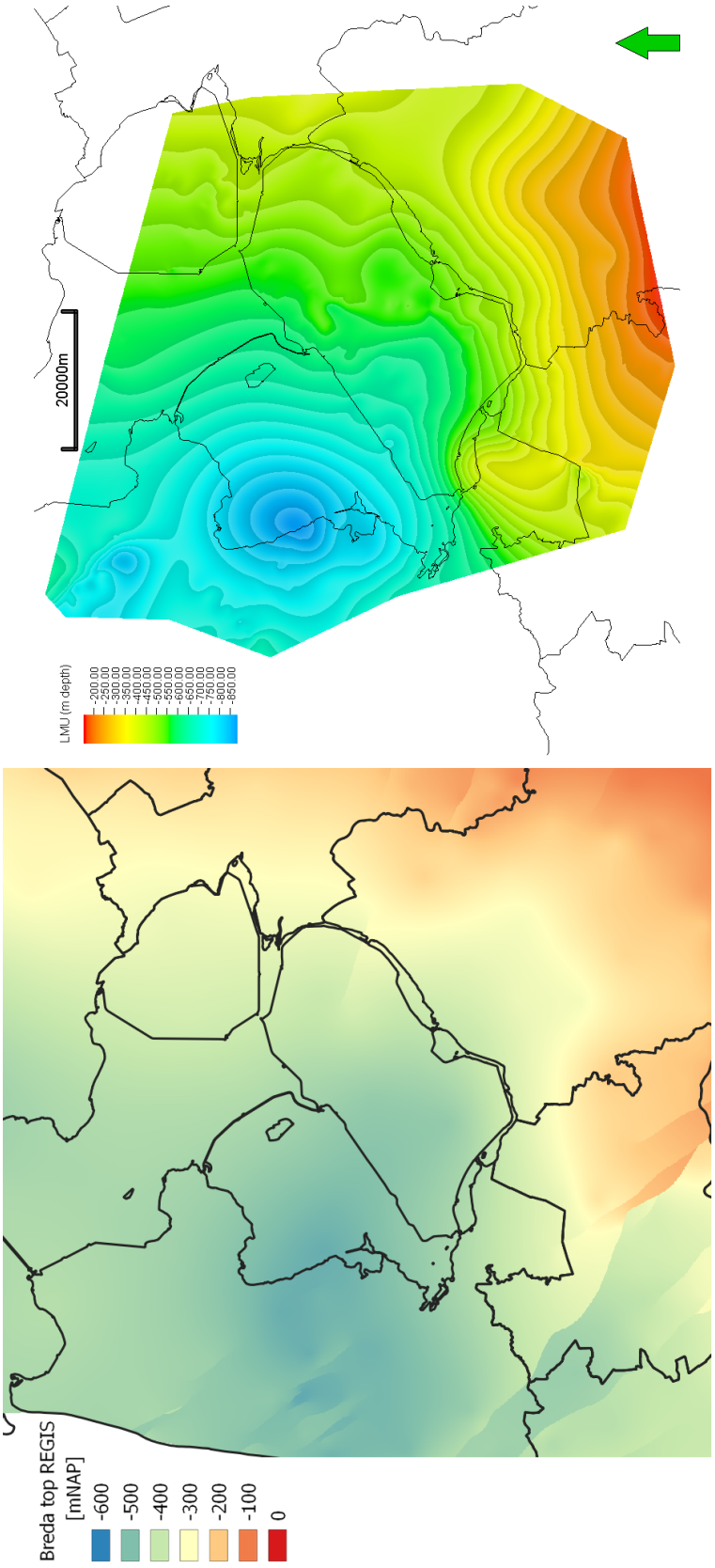

Fig. 2.23: Top of the Breda Formation in the REGIS model next to the resulting LMU surface from this study

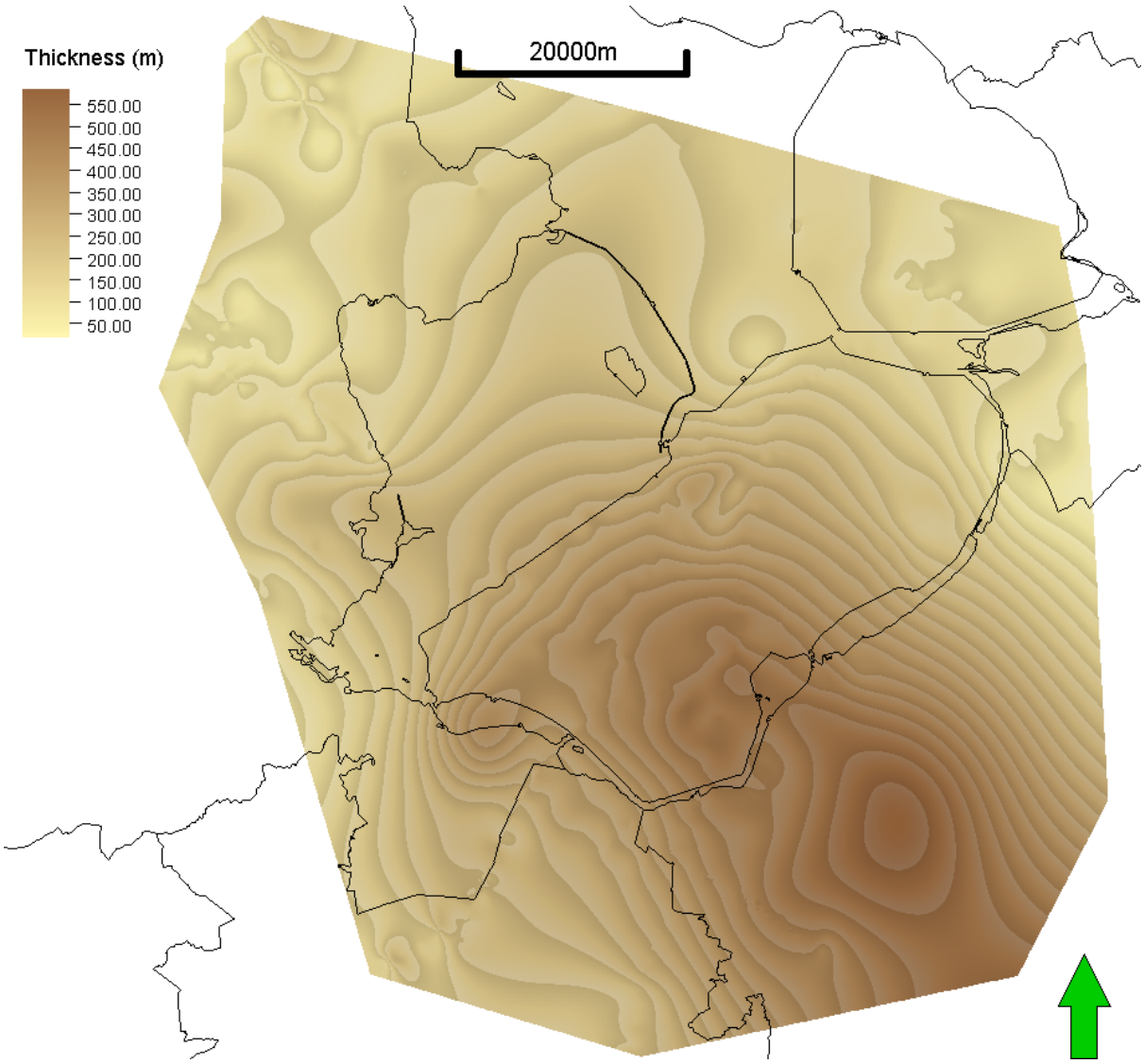

Fig. 2.24: Total thickness of the Breda Formation in the ZZL

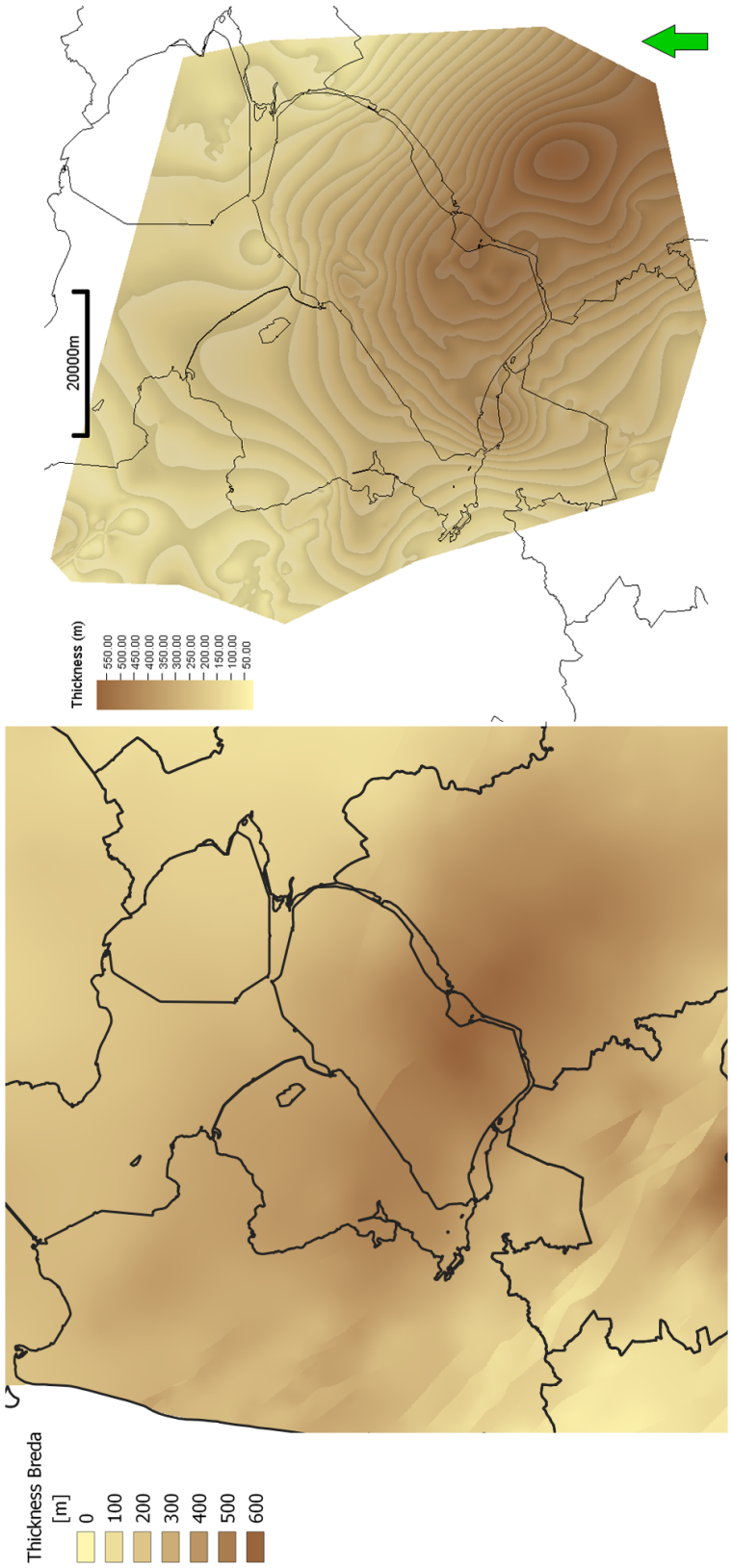

Fig. 2.25: Total thickness of the Breda Formation in the REGIS model next to the resulting thickness from this study

2.2.3 Results petrophysics

Figure 2.26 shows the net sand value for various clay models with increasing V_{cl} cutoffs for the NDN-120 well. As can be noticed from the figure, the models which show an elbow point within the previously mentioned standard range of 20% to 35% are the Larionov Tertiary and Stieber models, both sitting roughly at 35%. The Clavier and Larionov old have an elbow point at roughly 50%, while the linear model goes up to 65%.

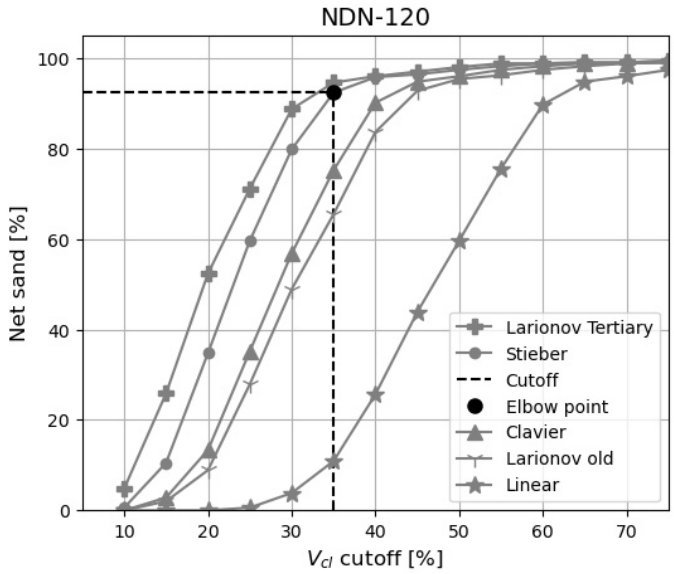

Fig. 2.26: Various clay volume models applied to the GR log of the NDN-120 well. As an example, the elbow point and corresponding cutoff for the Stieber model is shown

Table 2.8 and Figure 2.27 show that the Kozeny-Carman method with Stieber model is on average the closest to the well test permeability and has the lowest standard deviation. This combination is therefore applied to all other wells with porosity logs to calculate the permeability. The other combinations (largely) overestimate the permeability on average and also have larger standard deviations.

Tab. 2.8: Mean permeability values and standard deviation for four methods, using two V_{cl} models as input (NDN-120 well). The well test permeability is taken from Deelder (1977)

NDN-120		Larionov Tertiary model		Stieber model	
	Unit	Mean	Stdev	Mean	Stdev
Kozeny-Carman	mD	696	382	597	336
van Baaren	mD	2243	1543	1834	1313
Barr	mD	1725	946	1479	833
Kozeny	mD	1229	630	1054	557
Well test	mD	280			

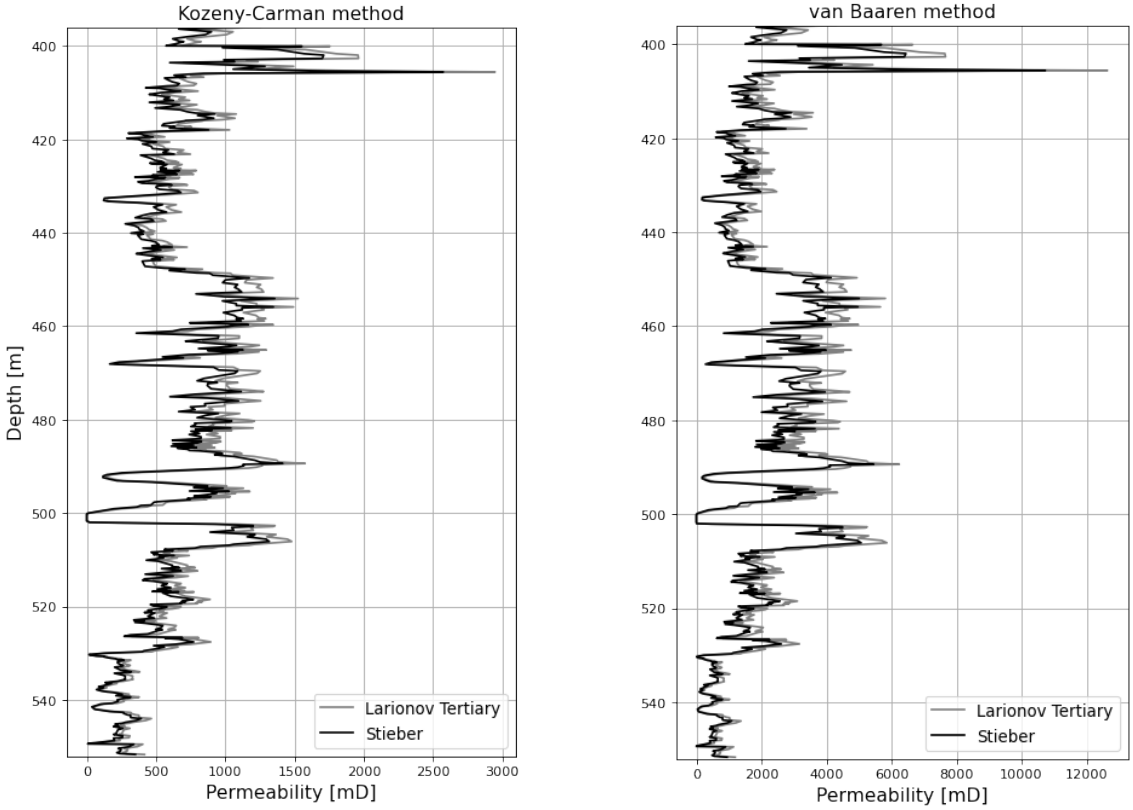

(a) Kozeny-Carman permeability **(b)** van Baaren permeability

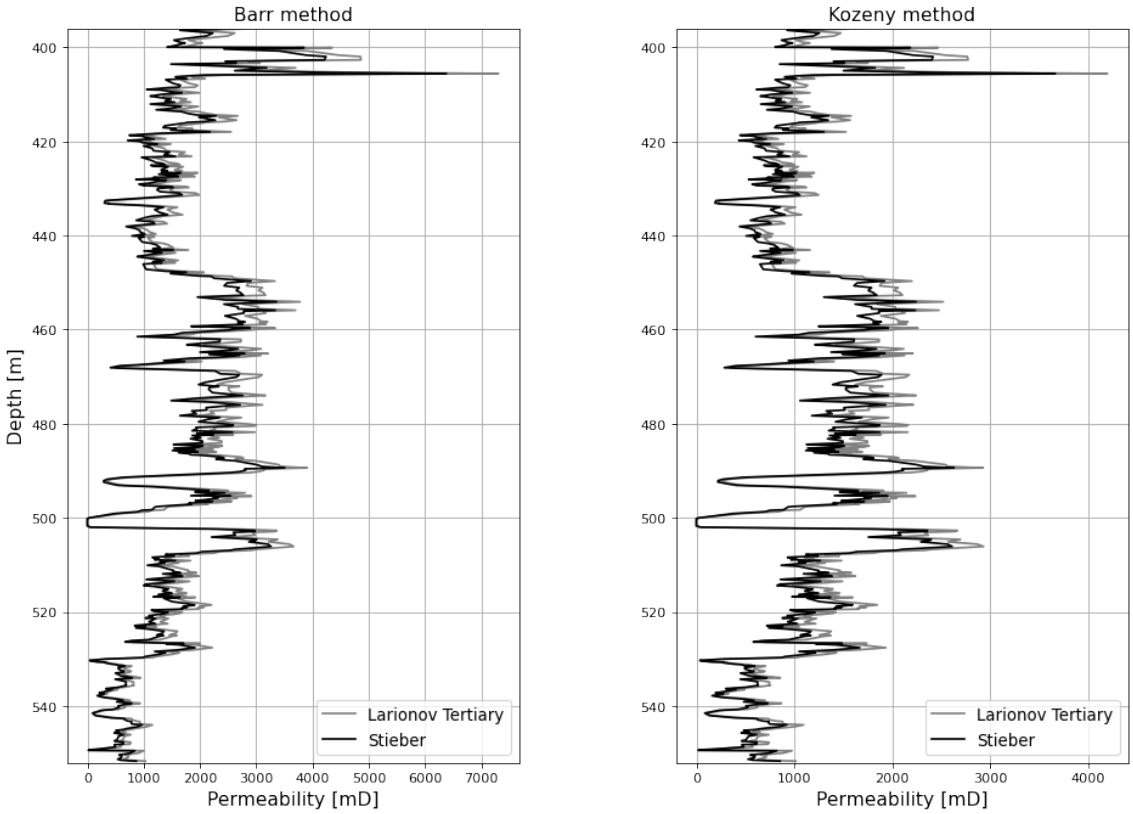

(c) Barr permeability **(d)** Kozeny permeability

Fig. 2.27: NDN-120 permeability calculated using four methods and two clay volume models

The recorded sand median values are plotted versus depth, shown in Figure 2.28. The average sand median line shows an average grain size increase going upward.

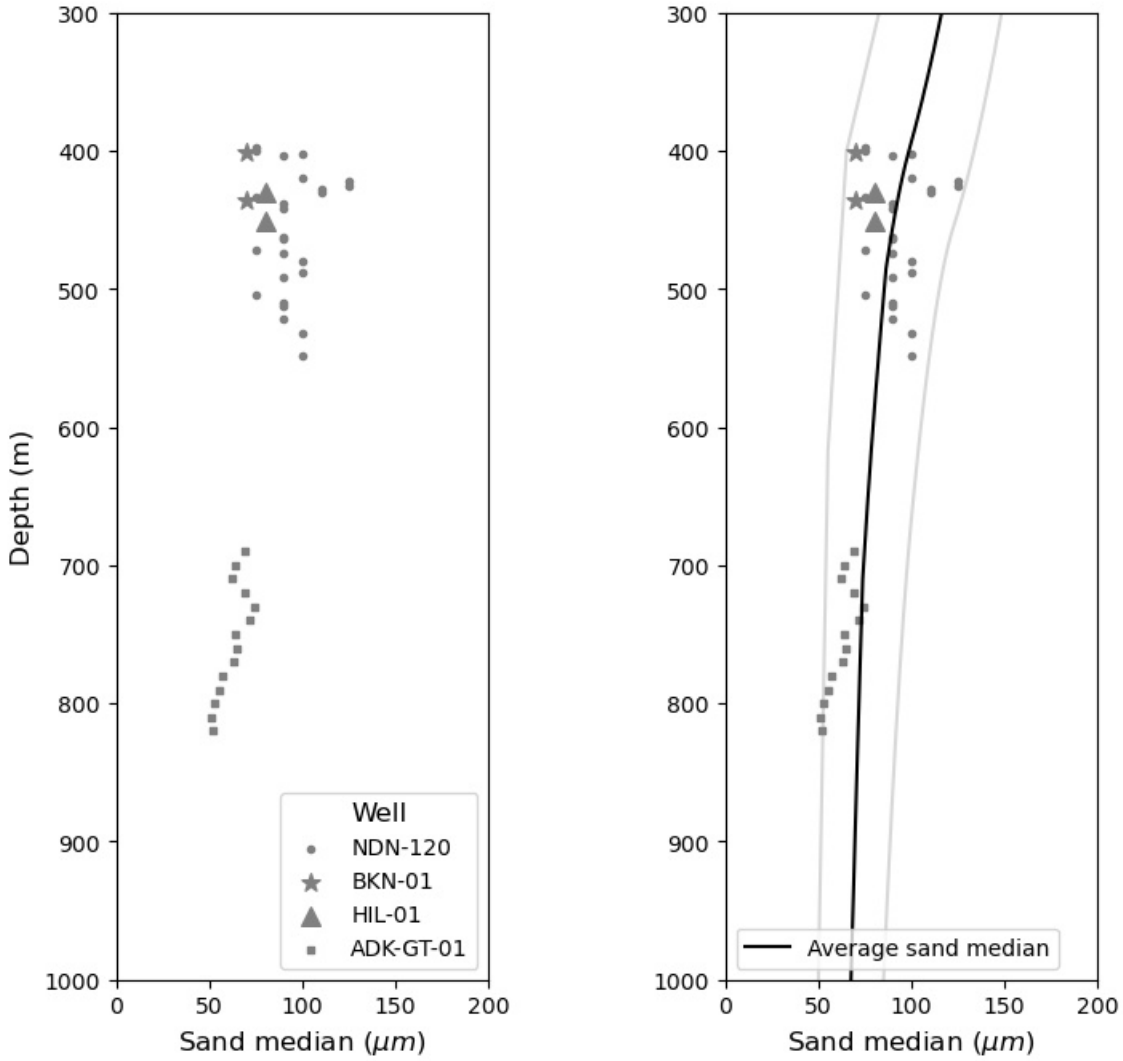

(a) Original sand median data from wells in the ZZL area

(b) Average sand median line fitted through data points, including upper and lower limit

Fig. 2.28: Measured sand median values in the Breda Formation (from Table 2.7)

Figure 2.29 shows the average net sand values for increasing V_{cl} cutoffs in all 15 wells with a porosity log. The same general trend can be noticed as shown in Figure 2.26 for the NDN-120 well only, resulting in a similar elbow point and corresponding cutoff value. The histogram in Figure 2.30 shows the distribution of the clay volume values in all these wells and the cutoff line. All values right of the line will be excluded from the net sand value.

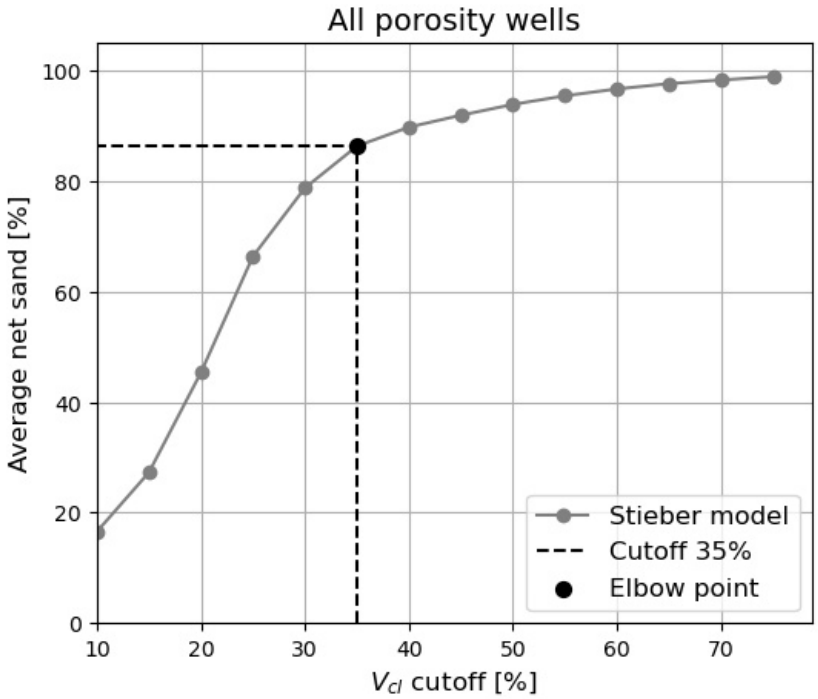

Fig. 2.29: Average clay volume trend for all 15 wells with a porosity log. A similar elbow point as in Figure 2.26 is observed

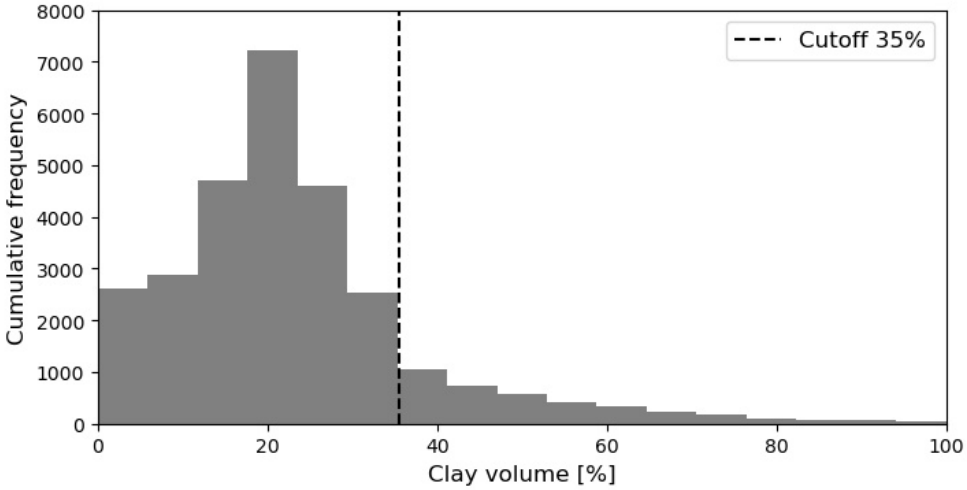

Fig. 2.30: Histogram plot displaying the clay volume distribution in all 15 wells with a porosity log. The chosen cutoff value of 35% is shown

Figure 2.31 shows the average net sand value for increasing porosity cutoffs. A porosity cutoff of 15% can be noticed at the elbow point, which is taken as the general porosity cutoff value for all wells within the ZZL. The histogram in Figure 2.32 shows the distribution of the porosity values, as well as the cutoff line. The values left of the line are not included in the net sand.

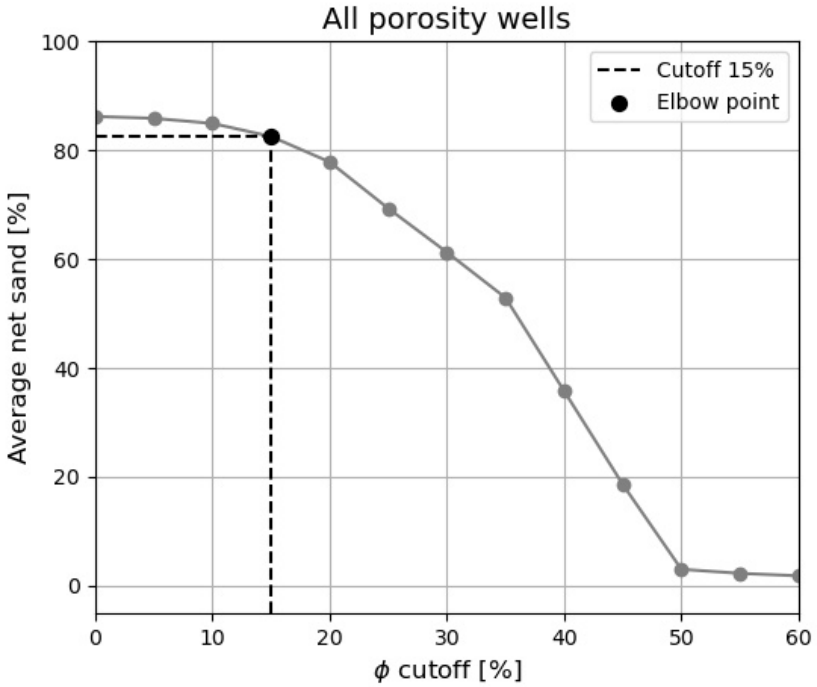

Fig. 2.31: Average effective porosity trend for all 15 wells with a porosity log. The elbow point and corresponding cutoff value are shown

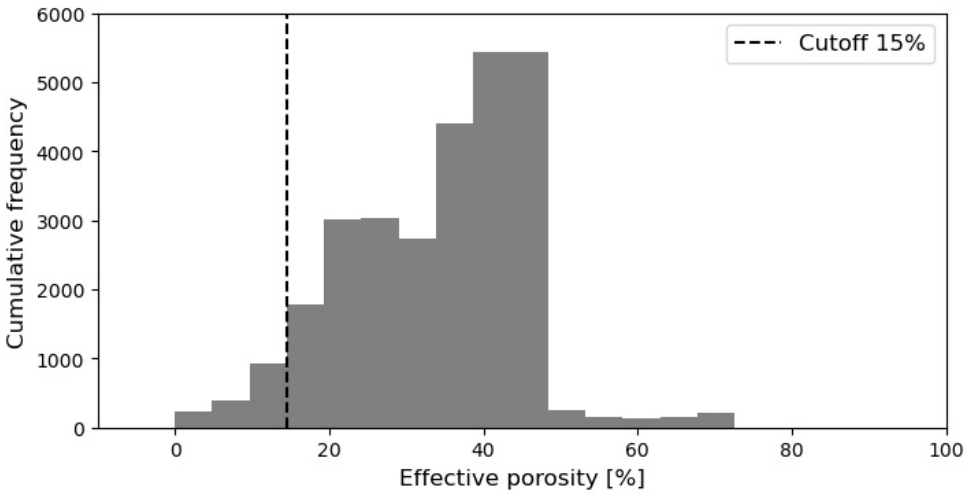

Fig. 2.32: Histogram plot displaying the effective porosity distribution in all 15 wells with a porosity log. The chosen cutoff value of 15% is shown

As stated before, porosity was evaluated for 15 wells. Three types of porosity logs are present: density, density-neutron pair and sonic log. From one well of each type, the resulting porosity, permeability and net sand log is displayed. See Figure 2.4 for the locations of these wells.

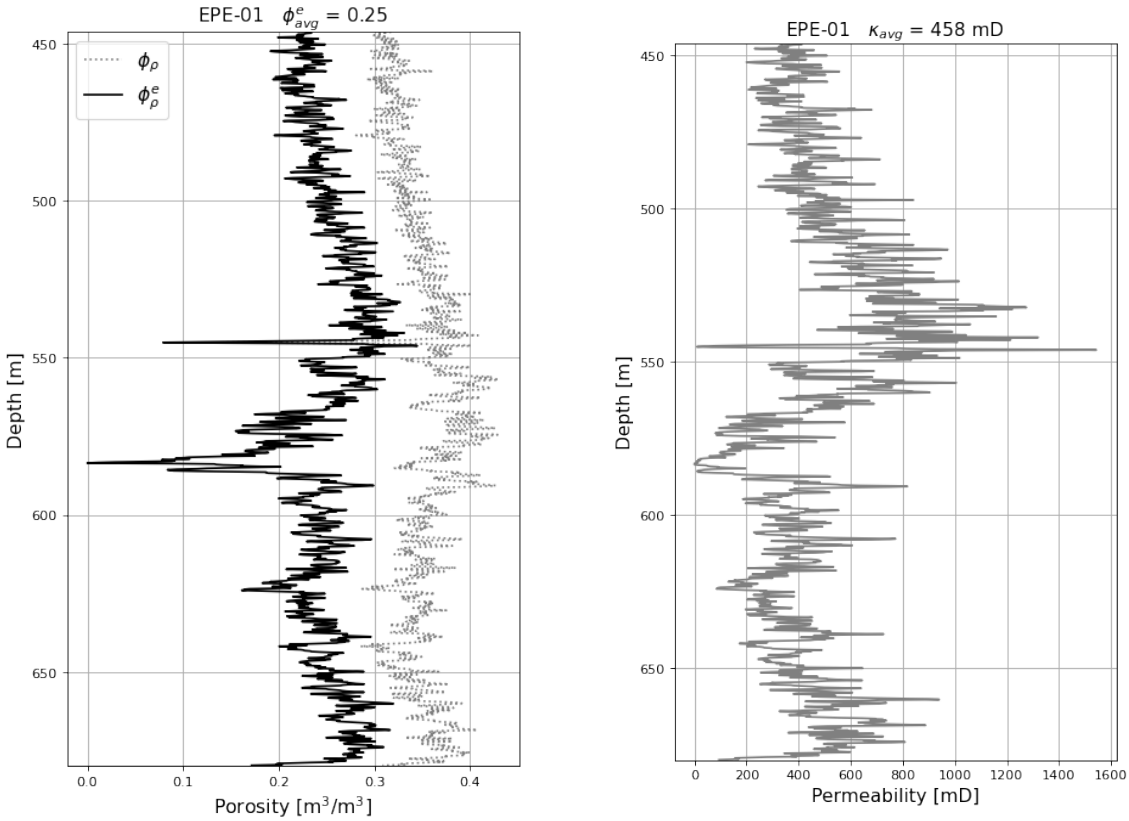

(a) Porosity from density log

(b) Permeability derived from porosity

Fig. 2.33: Calculated poro/perm logs in the EPE-01 well

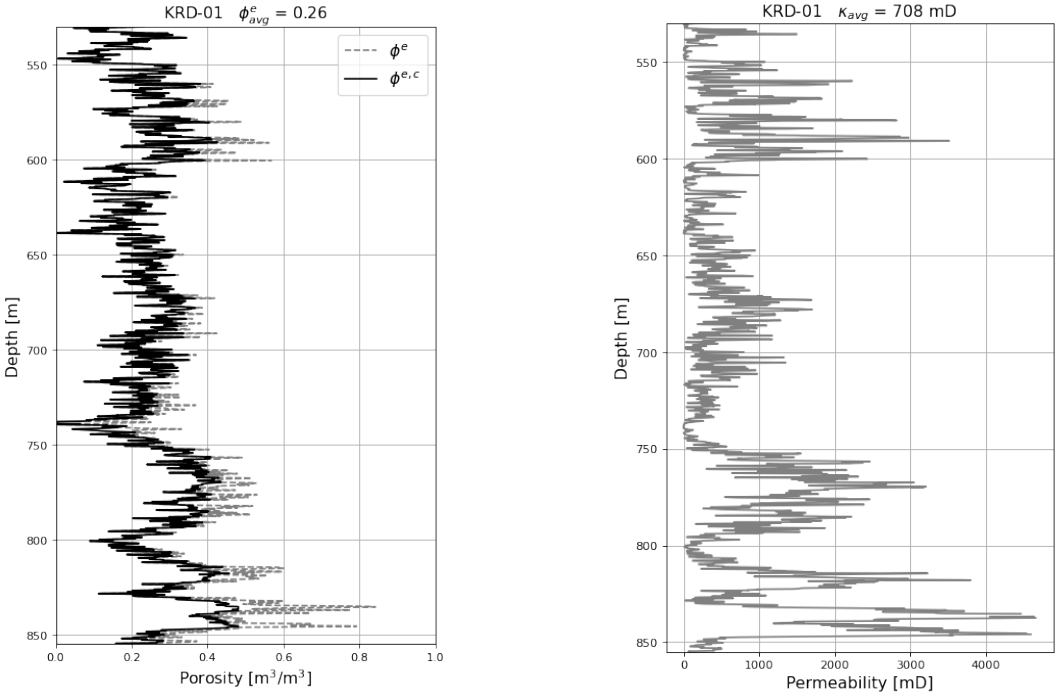

(a) Porosity from density-neutron log pair **(b)** Permeability derived from porosity

Fig. 2.34: Calculated poro/perm logs in the KRD-01 well

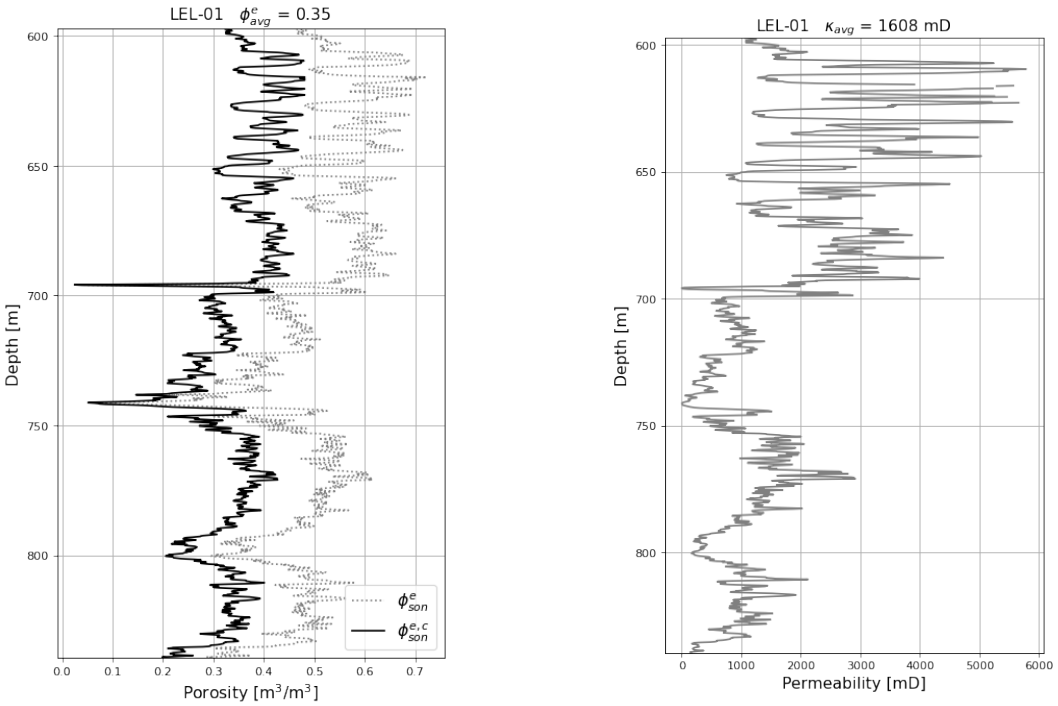

(a) Porosity from sonic log **(b)** Permeability derived from porosity

Fig. 2.35: Calculated poro/perm logs in the LEL-01 well

In the RST-01 well, both the sonic and density log were available. For this well, the two resulting effective porosities are shown together below for comparison. The permeability is calculated from the combined density and sonic porosity.

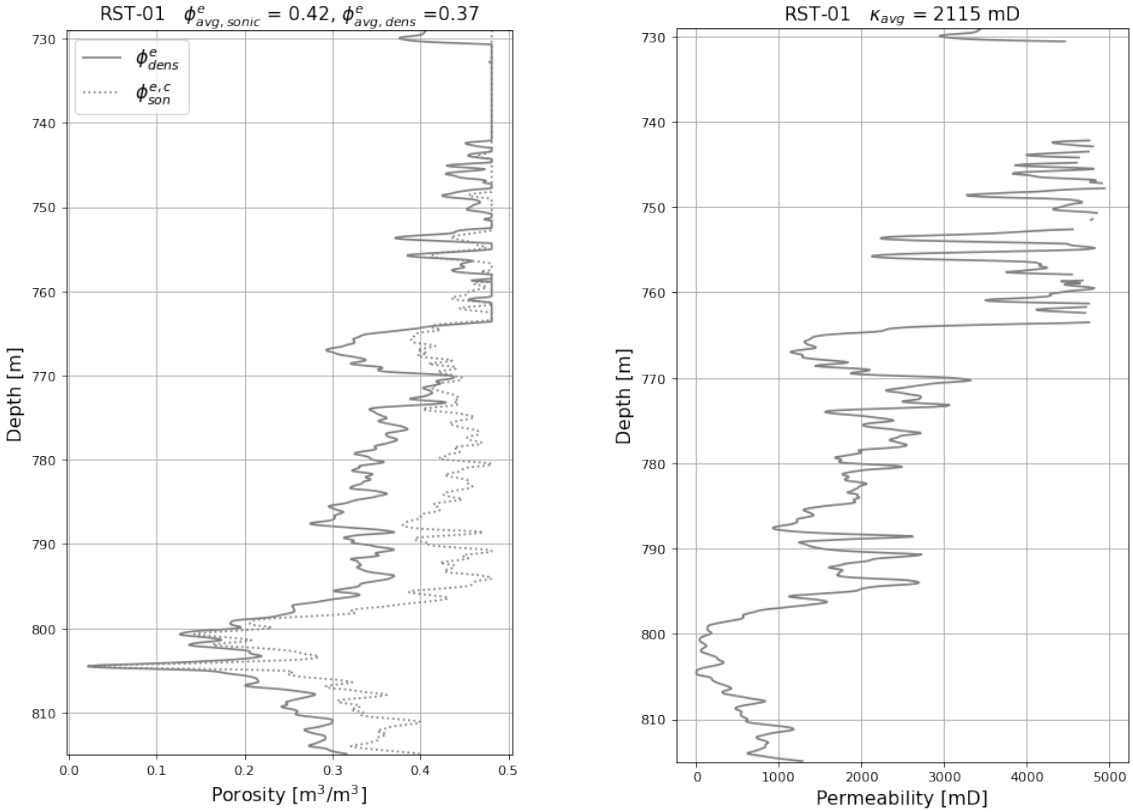

(a) Porosity calculated from density/sonic log **(b)** Permeability derived from density porosity

Fig. 2.36: Calculated poro/perm logs in the RST-01 well

The net sand value is calculated in every well with a porosity log in the ZZL (15 wells). The average calculated net sand value is 0.82, with V_{cl} and porosity cutoffs of 35 and 15%, respectively. The result is graphically displayed for four wells.

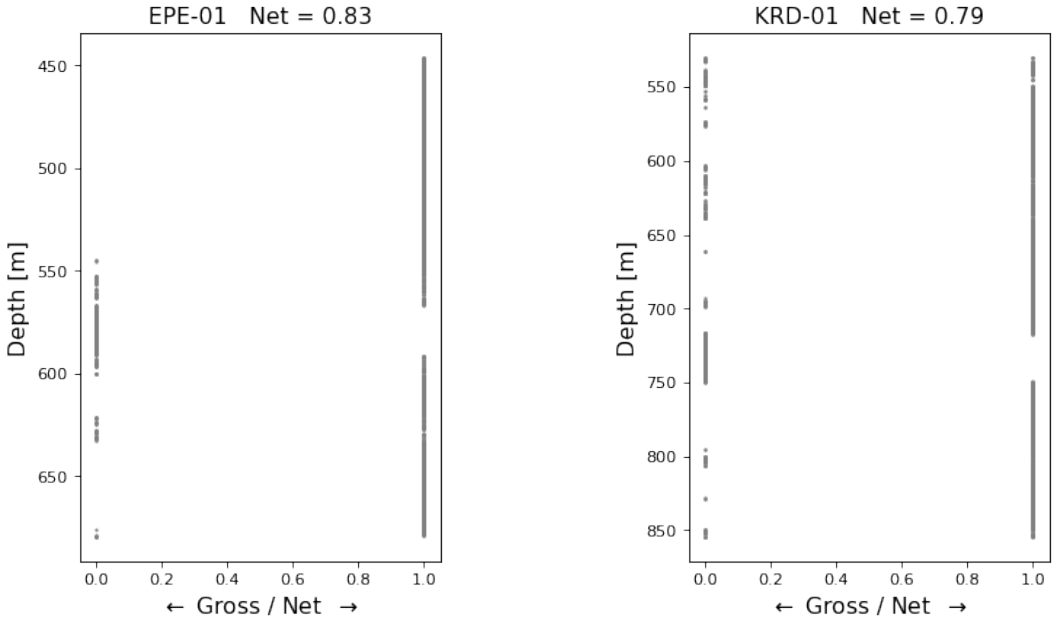

(a) N/G per depth in EPE-01 **(b)** N/G per depth in KRD-01

Fig. 2.37: N/G in EPE-01 and KRD-01

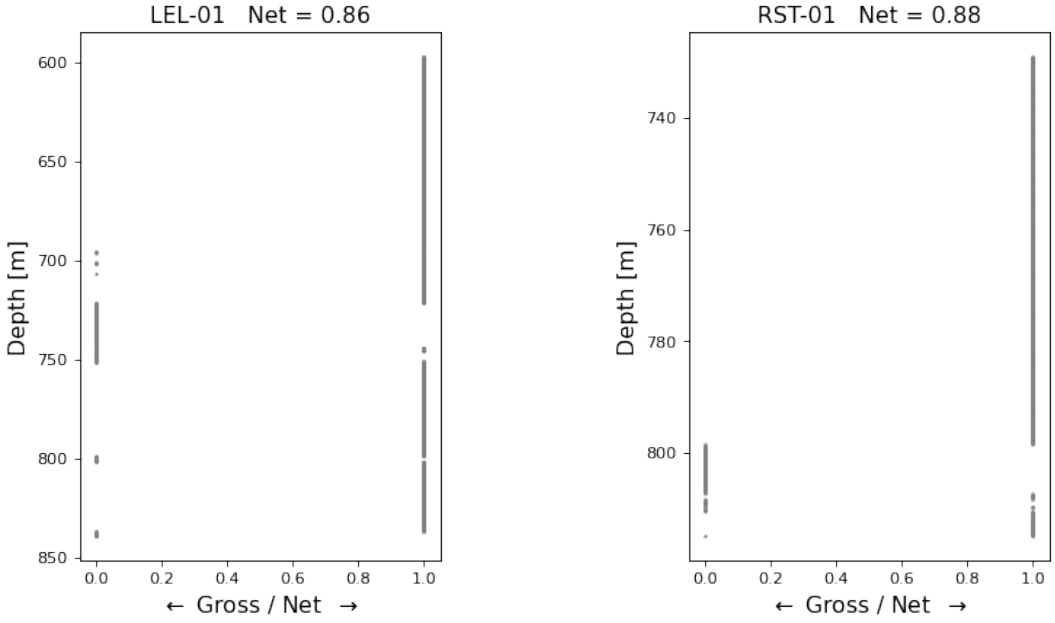

(a) N/G per depth in LEL-01 **(b)** N/G per depth in RST-01

Fig. 2.38: N/G in LEL-01 and RST-01

By multiplying the reservoir thickness with upscaled permeability and net sand, a 2D transmissivity map can be created for the entire ZZL area. The figure below shows the resulting map.

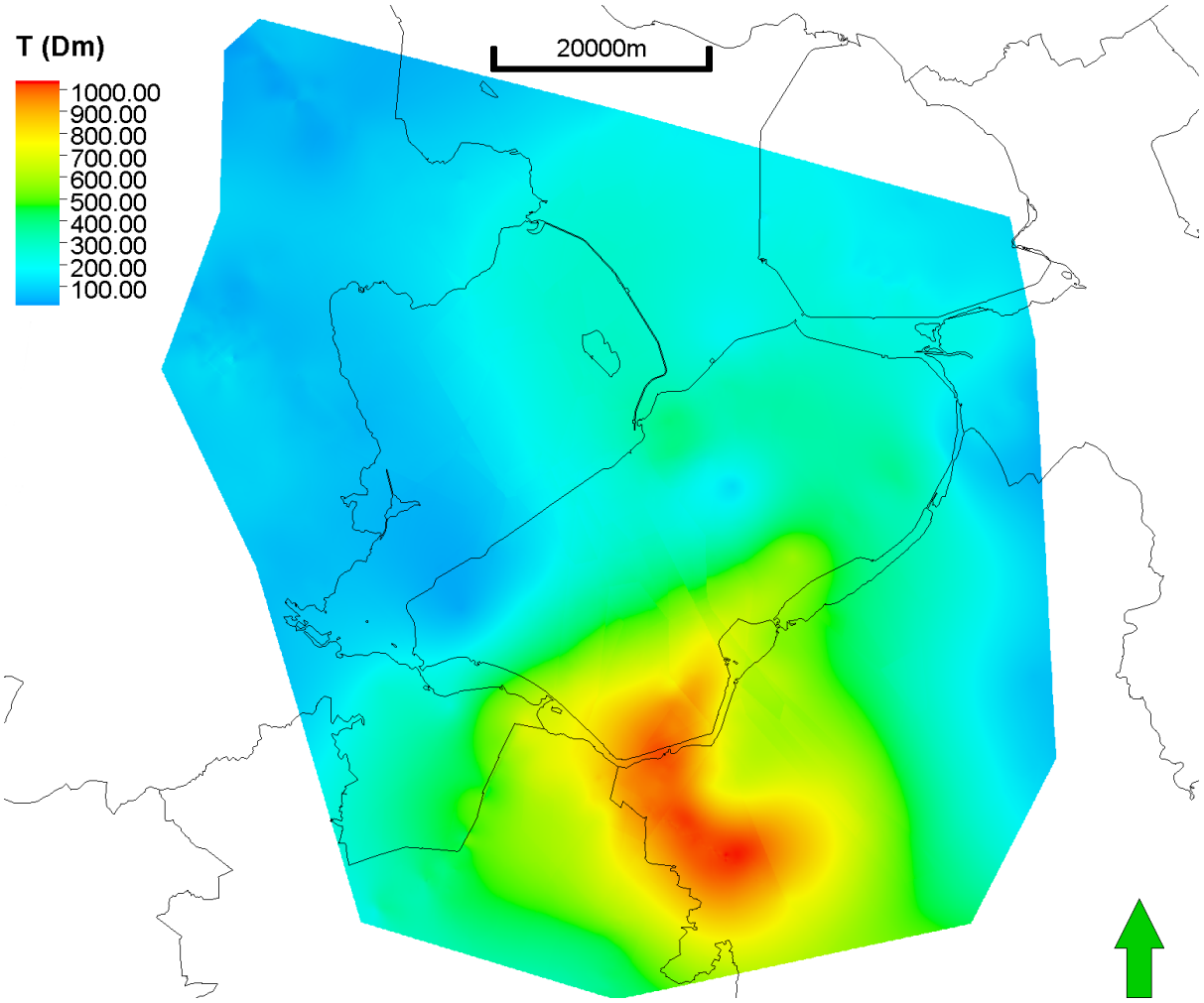

Fig. 2.39: Transmissivity distribution in the ZZL Breda Formation

2.3 Discussion

The results from this chapter show new maps for various reservoir characteristics. The data and methods used to generate these maps have been extensively elaborated in the previous sections. The porosity and permeability have been validated within the possibilities. Still there are some discussion points that arose while conducting this research. These points are worked out in detail in this section.

The uncertainty in the generated EMU, MMU and LMU surfaces is twofold. The first component is the interpretation uncertainty. In some location the seismic data are quite noisy, which made it hard to follow certain reflectors, especially the LMU (as shown in Figure 2.10). This induces some uncertainty in the interpreted reflectors, which have a direct effect on the generated surfaces. The second component is the interpolation uncertainty. The generated surfaces for the EMU, MMU and LMU are the result of interpolation between the interpretations on seismic lines and cubes. In locations where no seismic data are available, the convergent algorithm within Petrel creates spatial interpolations. This algorithm is relatively simple in the sense that a straight plane is fitted between two interpretations. The uncertainty therefore increases away from the seismic data.

The presence of glauconite has been proven in section 2.1.2 in the ADK-GT-01 well. However, the high GR interval could not be directly related to a sharp increase in glauconite content. As stated before, glauconite minerals have a certain influence on the gamma ray log. In general, more glauconite will result in a higher API reading on the GR log. Quantifying this effect is extremely difficult, because GR influences could originate not only from glauconite content (which is usually not known) but also on volumetric presence of other GR-emitting minerals (such as clay) and influence of drilling mud or logging method. On top of that, glauconite minerals can contain varying proportions of potassium (Kennedy, 2015), which is the element emitting the gamma rays, while variations can occur vertically and laterally. Cuttings or core samples would have to be analysed with specialized tools (for example with XRD) to know the exact chemical composition of the glauconite at a certain location. This process is, however, very time consuming and could not be fitted into the time frame of this thesis.

Furthermore, gamma ray corrections are applied on the logs where the drilling mud had demonstrable effects. The disturbed values are calibrated towards a trusted well. To what extent these 'trusted' wells actually show a completely undisturbed log pattern is uncertain, since glauconite or other factors could have had a certain influence here as well. Also, the correction process itself induces uncertainty since the assumption is made that the sand and shale line in the disturbed well is equal to the trusted well, while in fact this cannot be known for sure. Again the consequential uncertainty is undeniably present but hard to quantify.

The permeability is assumed to be isotropic, and therefore equal in all directions. This assumption is made since no evidence was encountered which suggests laminated clay layers

or impermeable horizontal streaks, such as found in the BSM, to be present. Moreover, the permeability values calculated in the Breda Formation present in the ZZL are relatively high, compared to other (shallow) formations. As reference, the permeability in the BSM ranges roughly from 200 to 1000 mD (TNO, 2022d), while the average permeability recorded in the ZZL Breda Formation is about 1300 mD. The difference could be attributed to the low permeable streaks present in the BSM, which form barriers to vertical flow (Geel & Foeken, 2021). Currently, there is no evidence of similar barriers in the Breda Formation.

2.4 Sub-conclusion

Cutting analysis

Figure 2.16 shows a gradual increase in glauconite content towards the high GR interval. Right above the interval, even higher glauconite content is observed. The impression arises that the high GR interval is not solely caused by glauconite, since a sharp increase in glauconite content would be expected at the top of the interval as well as a sharp decrease at the bottom. Moreover, some clay was observed in the KRD-01 cuttings alongside a silty sand fraction within the high GR interval. Therefore, from the cutting analyses the notion arises that the high GR interval can not be exclusively allocated to either a high clay or high glauconite interval. The interval might still be clay rich and low permeable, but is unlikely to be a homogeneous clay package.

Figure 2.17 shows the grain size distribution in the ADK-GT-01 well. An average increase in grain size towards the top of the formation can be noticed. This coarsening upwards sequence is also reflected by an average increase in permeability towards the top of the formation, for example shown in Figure 2.36b.

In the geologic background section (section 1.4.1) it's mentioned that the transition into the overlying Oosterhout formation should see an increase in shell content. This concept is invigorated by the observations made from the ADK-GT-01 cuttings, where the shell content increases towards the top (see Figure 2.16). This implies that the placement of the LMU at 710 m MD in the ADK-GT-01 well (see Figure 2.5) is conceivable.

Seismic interpretation

The results from the seismic interpretation in this chapter are placed next to the currently present interpretations from REGIS. The base Breda in REGIS is comparable to the EMU interpretation from this study. The MMU and LMU interpretations show larger differences when comparing them to the mid and top Breda in REGIS. For example, the deepest part of the mid Breda (southern Flevoland and Markermeer) in REGIS is somewhere between 600 - 700 m depth, while the MMU from this study is between 850 and 950 m deep in this area. Moreover, the top Breda in REGIS is situated at maximum 600 m depth in Noord-Holland, while the LMU from this study goes up to 850 m depth in this location. Lastly, the thickness maps show a roughly comparable distribution of high and low thickness areas, however the REGIS map shows a thicker succession in southern Flevoland (500 - 600 m thick) compared to the map from this study (400 - 500 m thick). Since the maps from this study are generated using much more (types) of data, the new maps can be considered as (slight) improvements.

Petrophysics

Clay volume, porosity, permeability and net sand could be calculated for 15 wells with a porosity log. Reasonable cutoff values for the clay volume and porosity could also be determined. The Stieber model together with the Kozeny-Carman equation showed the best results when comparing it to the well test permeability from the NDN-120 well. By multiplying the petrophysically derived permeability and net sand with the total thickness, and interpolating between the wells, a transmissivity map could be created for the entire ZZL area (see Figure 2.39). As shown on the figure, the highest geothermal potential of the Breda Formation in the ZZL, when purely considering geological parameters, is found in southeast Flevoland, northwest Gelderland and northeast Utrecht.

Chapter 3

Dynamic simulation

Two of the objectives of this thesis are to predict the potential geothermal energy output from the Breda Formation in the ZZL, and to verify the optimal well design. These are important steps, because they provide more insight in the geothermal potential specifically for the Breda Formation and for medium deep geothermal in general. In this chapter, the methodology and results of simple dynamic simulations for the Harderwijk area are shown and discussed.

3.1 Method

In this section, the methods used to obtain possible doublet lifetimes and flow rates are discussed. The static model described in the previous chapter is used as input for the dynamic simulations. The ECLIPSE reservoir simulator (Schlumberger, 2022) is used for this purpose. Multiple scenarios with different well trajectories and reservoir geometries are considered.

3.1.1 Case study area: Harderwijk

To still get an insight in the reservoir capabilities of the Breda Formation in the ZZL, a high potential case study area is selected. A region of 10x8 km around Harderwijk is picked for this purpose (see Figure 3.1). The area is chosen for the case study based on a combination of geological properties and surface conditions:

Geological properties:
- Relatively high transmissivity averaging 500 Dm (see Figure 3.1)
- Base of the formation up to 1000 m depth (see Figure 3.2), thus relatively high expected reservoir temperature

'Surface' conditions:
- Area available without drilling-free zones, drinking water locations or other restriction (see Appendix C)
- Residential area with a municipal energy consumption of 1033 GWh in 2019 (Rijkswaterstaat, 2019)

– Current heat demand is primarily met by natural gas, while the municipality has the ambition to move to sustainable alternatives
– Small scale heat network is being realized for the 'Waterfront' district.

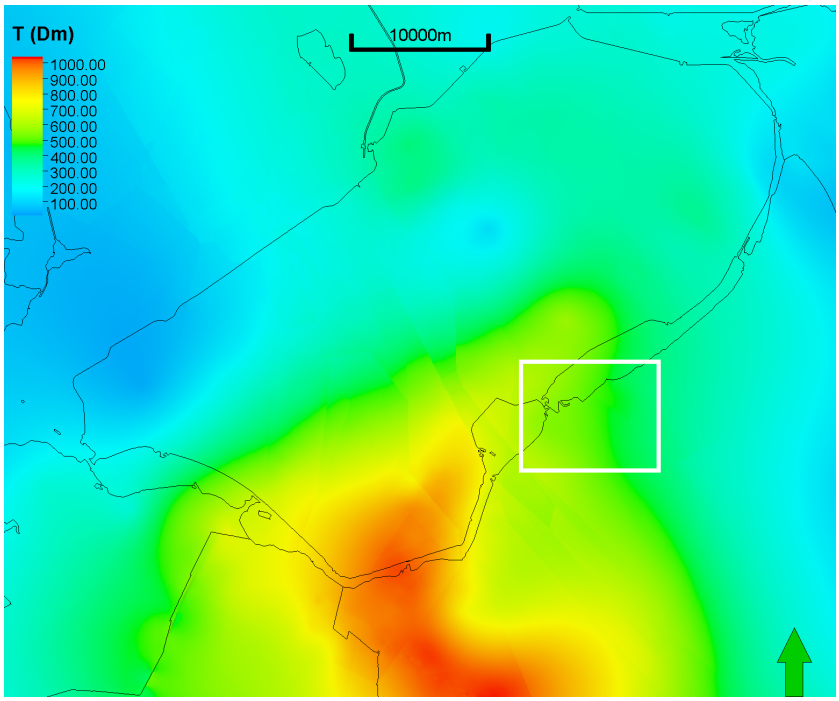

Fig. 3.1: Map showing the case study area around Harderwijk. Transmissivity is displayed in the background

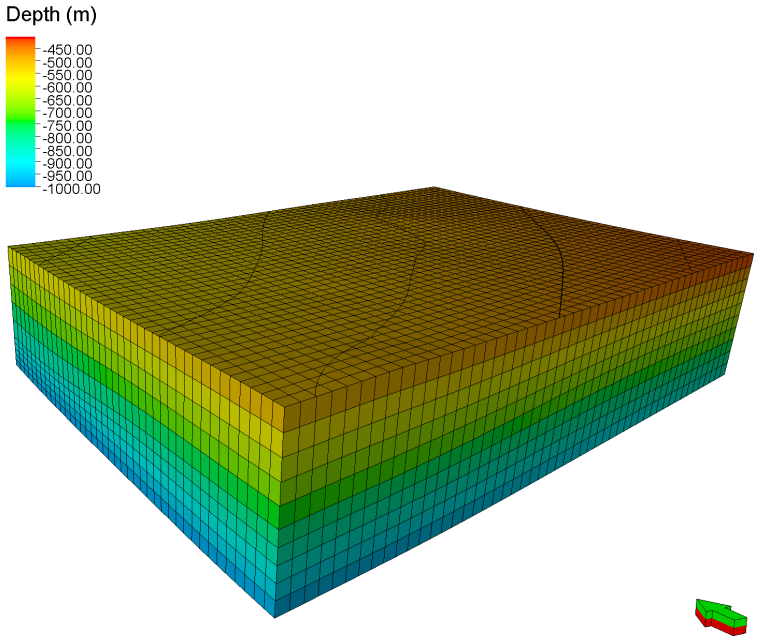

Fig. 3.2: 3D geometric cube of the case study area underneath Harderwijk

3.1.2 Boundary conditions

The bottom and top of the cube shown in Figure 3.2 act as perfectly sealing boundaries in the dynamic model. As discussed in section 1.4.1, this assumption is quite accurate for the bottom boundary, however disputable for the top boundary. The local composition of the overlying Oosterhout Formation is relatively unknown, since the lateral extent of the sealing layers found in NDN-120 and WSP-01 is uncertain (Coenen, 1974). A scenario where the top boundary is not sealing could be possible.

An alternative scenario is defined as follows. As shown in Figure 2.5, there is a continuous trending 'high gamma ray interval' observed above the MMU in every well located in the ZZL area. As discussed in section 2.4, it is uncertain to what extend this layer is sealing. It does however likely represent a low-permeable zone. With this assumption, a second scenario is considered where the reservoir consists of only the GH Formation below the high GR interval, with the high GR interval acting as sealing top layer. Figure 3.3 depicts the grid for this scenario.

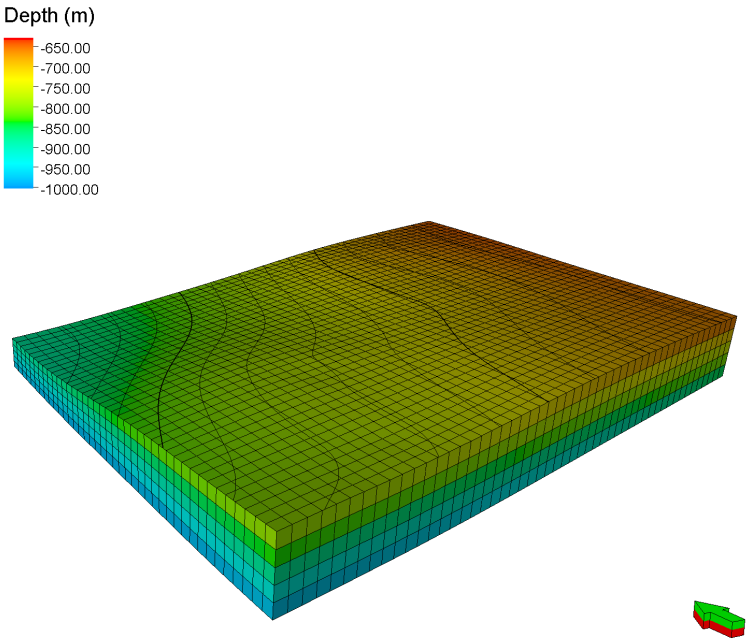

Fig. 3.3: 3D geometric cube of the case study area underneath Harderwijk, only showing the GH Formation

3.1.3 Input parameters

The petrophysically derived values for permeability, porosity and net sand are used as input for the dynamic model. Furthermore, fluid properties, rock properties and initial conditions have to be determined accurately. Also, well specifications are important, such as well design, configuration and spacing, as well as bottom hole pressure in the injection and production well. In this section, the choices and reasoning behind all input parameters are elaborated.

Fluid & rock properties

The fluid properties define the density, viscosity, formation volume factor and compressibility of the reservoir fluid. These properties are important to know. High density and viscosity have a negative effect on the flow rate, and vice versa. The formation volume factor is used to translate the fluid volume at reservoir conditions to the volume at surface conditions. The fluid compressibility is a measure of the fluid's capability to change volume and consequently change density when pressure is applied.

The fluid properties are all directly related to the water salinity. If the water salinity is known, the fluid properties can be derived. Unfortunately, no direct salinity measurements from the Breda Formation in the ZZL exist. To still obtain a relatively accurate estimation, two salinity data sets are combined, shown in Figure 3.8. The first set originates from a paper by Griffioen et al. (2016) on the composition of groundwater in Palaeogene formations in the Netherlands. Their paper includes several salinity measurements taken in different wells at different depths. Secondly, the Pressure Southern North Sea (PSNS) database contains many salinity measurements in different wells both offshore and onshore (TNO, 2015), from which data points up to 1700 m depth are included here. The data points show the chloride concentration at a specific depth. While theoretically the salinity is defined as the concentration of all dissolved salts, in practise chloride makes up for more than 90% of the salt composition. Therefore the salinity is assumed to be directly related to the chloride concentration. After combining and plotting the two databases, polynomial least-squares lines are fitted through the data, as shown in the figure. At a reference depth of 800 m TVD, the salinity is roughly 30,000 ppm. This leads to a fluid density of 1020.35 kg/m^3, viscosity of 0.73 cP, formation volume factor of virtually 1.0 and fluid compressibility of 4.14 x 10^{-5} bar^{-1}. These values are used as input for the dynamic simulations.

Rock compressibility is a measure of how much a formation could compact when pressure changes. Several authors have tried to relate rock compressibility to various parameters. Hall (1953) composed a simple formula deriving rock compressibility from porosity via the following relationship:

$$c_f = \frac{1.782}{\phi^{0.438}} \times 10^{-6} \tag{3.1}$$

where c_f = formation compressibility (psi^{-1}) and ϕ = porosity. The average porosity in the full reservoir is equal to 0.35 and equal to 0.33 in the GH Formation. This leads to a rock compressibility of 2.82 x 10^{-6} psi^{-1} or 1.95 x 10^{-7} bar^{-1} in the full reservoir and 2.90 x 10^{-6} psi^{-1} or 2.00 x 10^{-7} bar^{-1} in the GH reservoir.

A material's capacity to transport heat is determined by its thermal conductivity. A larger thermal conductivity coefficient causes faster heat transport and therefore more rapid thermal recharge of the system. Different facies have varying values for thermal conductivity. Since it is assumed that the Breda Formation is fully saturated with water, the combined thermal conductivity of the rock and fluid must be considered. Eppelbaum et al. (2014) report a thermal conductivity of 2.5 W/(mK) for sandstone and 1.1 - 2.1 W/(mK) for shale. Dafalla and Samman (2016) state combined thermal conductivities for saturated sand between 2 - 4 W/(mK) and 0.6 - 2.5 W/(mK) for saturated clay. The average value from these authors is about 2.1 W/(mK), which is considered sufficiently accurate as dynamic model input since the Breda Formation is composed of a mixture of sand, clay and water particles. For simplicity a constant value is assumed in the entire grid.

Initial conditions

Temperature, pressure and saturation are the initial conditions in the reservoir. Temperature and pressure generally increase with depth. Bonté et al. (2012) proposed the well known average thermal gradient of 31.3 °C per km in the Netherlands, with a surface temperature of 10.1 °C. This gradient became the standard method for estimating the reservoir temperature for geothermal exploitation. However, in many geothermal projects since then the actual produced temperatures were higher than predicted. Therefore Békési et al. (2020) and consecutively Gies et al. (2021) created an updated model based on inversion of temperature data. The result from their work is shown in Figure 3.4 at every 200 m depth increase. From the figure it can be determined that in the ZZL, at a reference depth of 800 m TVD, the initial reservoir temperature is 37.5 °C. This value is used as input for the dynamic model.

The PSNS database includes many pressure measurements in the Dutch onshore and offshore (TNO, 2015). In the accessory report it is concluded that for all tested onshore basins, the pressure gradient is close to normal. This implies that pressure increases with 10 bar every 100 m TVD. At a reference depth of 800 m TVD, the initial pressure is therefore 80 bar.

The initial saturation is assumed to be 100% of pore volume. Also, saturation is assumed to be single phase water with no hydrocarbons.

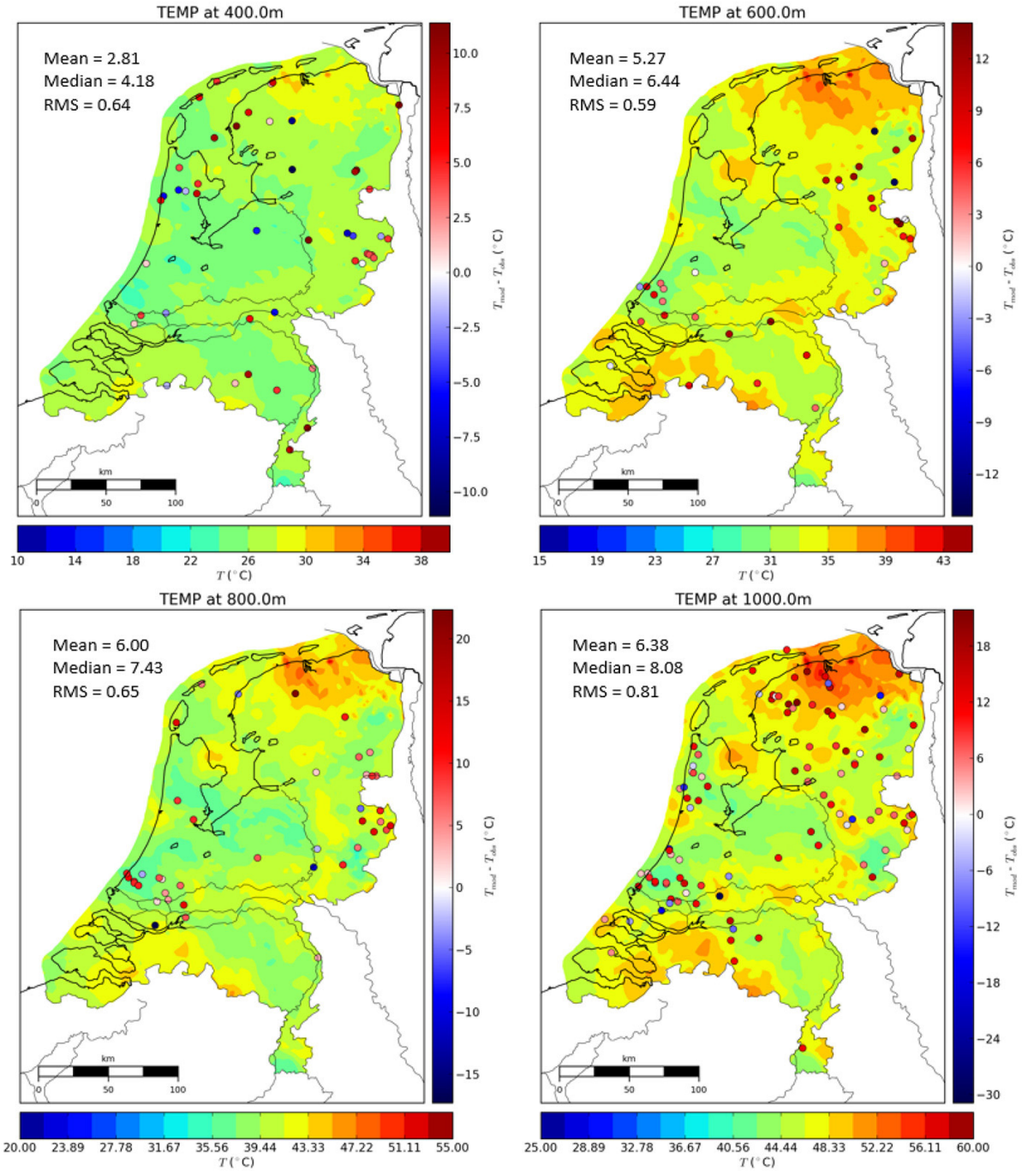

Fig. 3.4: Isodepth temperature maps of the Netherlands from 400 to 1000 m depth. The circles represent the difference between modelled and observed temperatures, with corresponding scale bar on the y-axis (Gies et al., 2021)

Well design

A doublet configuration with one production and one injection well is chosen, because of its simplicity and because this is currently the most used configuration in the Netherlands. Average spacing is maintained at 800 m for all scenarios. Three different well trajectories are considered: vertical, horizontal and inclined. Different well trajectories have a significant influence on a doublet's lifetime (Blinovs & Van Og, 2022), so it is worth evaluating. A vertical trajectory is easiest to drill, but expensive because two drilling locations are needed. Also, the flow rate might be limited in a relatively thin reservoir. Horizontal trajectories are more difficult to drill, but are generally cheaper compared to vertical wells since only one drilling location is needed. Also, longer screen lengths are possible in thin reservoirs. Inclined trajectories are somewhat in between vertical and horizontal when it comes to difficulty and screen length. Like horizontal wells, a single location is needed when drilling inclined. Inclined wells are generally cheaper than horizontal wells since the total well path is much shorter. Combinations of horizontal, inclined and vertical wells are possible, but for this thesis study the production and injection well are mirrored for simplicity.

A kick-off point at 270 m TVD is maintained for the horizontal and inclined wells. The kick-off is defined as the point from where the well starts deviating. The first 270 m must be drilled vertically to prevent bending stresses on the ESP and to ensure sufficient weight to drill and complete the well (Blinovs & Van Og, 2022).

As mentioned in section 3.1.2, two scenarios are considered. In the first scenario, production from the full reservoir is assumed, while in the second scenario only the GH Formation is considered. Due to the difference in thickness and depth, well trajectories and screen lengths have to be adjusted to fit each reservoir. In Figure 3.5 and Figure 3.6 the trajectories and screen lengths are shown for both scenarios. Within each scenario, screen lengths are kept roughly the same for vertical, inclined and horizontal wells. The depth of the screens is chosen such that the initial plateau production temperature is similar, such that the different trajectories can be compared (see section 3.2). The maximum depths are determined after a few simulation and well path adjustment iterations.

Flow rates of 4800, 8400 and 12000 m^3/day are simulated in the full reservoir in order to observe the differences and compare the results. 4800 m^3/day is on the low side, while 12000 m^3/day is considered very high (Blinovs & Van Og, 2022). In the GH reservoir, simulations with 4800 and 8400 m^3/day are performed, since a flow rate of 12000 m^3/day resulted in very short lifetimes. The produced water volume is kept equal to the injected volume. Injection temperature is assumed to be constant at 10 °C.

SodM (2013) composed a mandatory guideline for the maximum allowed injection pressure. This is defined as 0.135 times the depth of the reservoir. The top of the full reservoir is situated at roughly 500 m depth, while the top GH is located at about 700 m depth. This means that the maximum injection pressure for the reservoirs is respectively 67.5 and 94.5 bar.

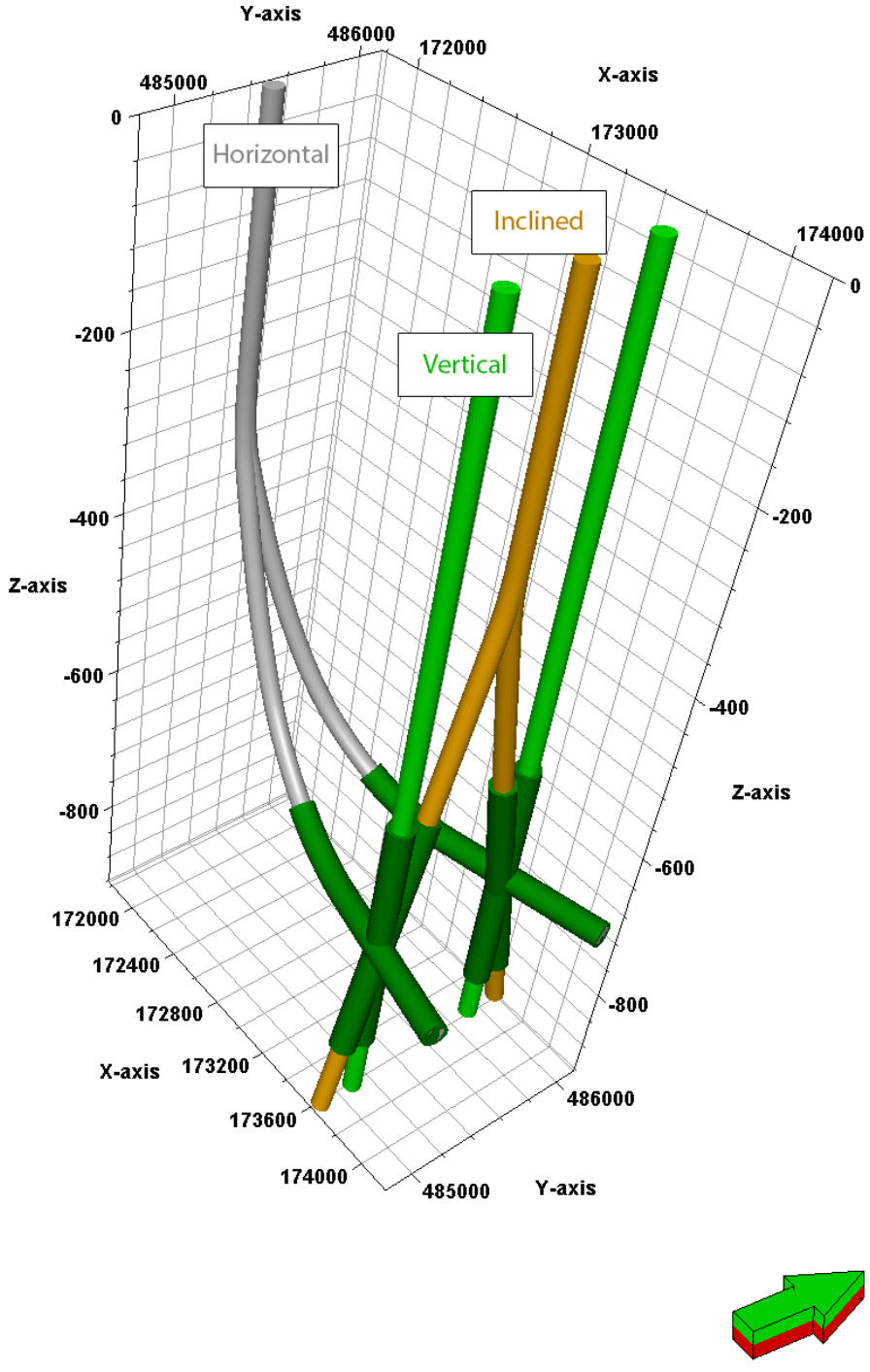

Fig. 3.5: Well trajectory scenarios in the full reservoir. Vertical, inclined and horizontal wells are shown. Screens are indicated as dark green sleeves. Production and injection wells are mirrored. Units on the axis are in meters

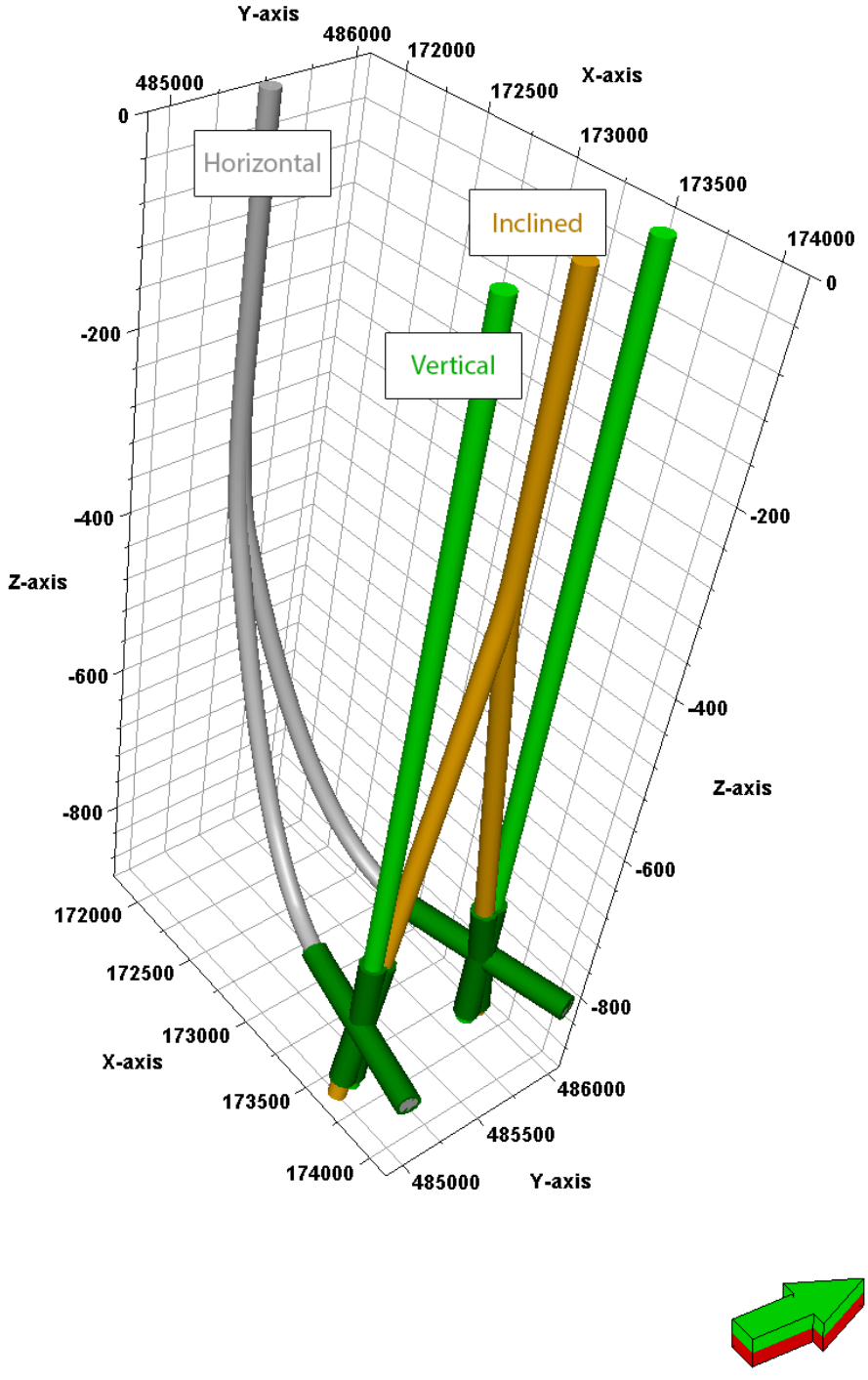

Fig. 3.6: Well trajectories scenarios in the GH Formation. Vertical, inclined and horizontal wells are shown. Screens are indicated as dark green sleeves. Well head locations are the same as for the full reservoir, however notice that the screens are situated deeper compared to the full reservoir wells in Figure 3.5. Screens are also shorter because the GH reservoir is less thick. Units on the axis are in meters

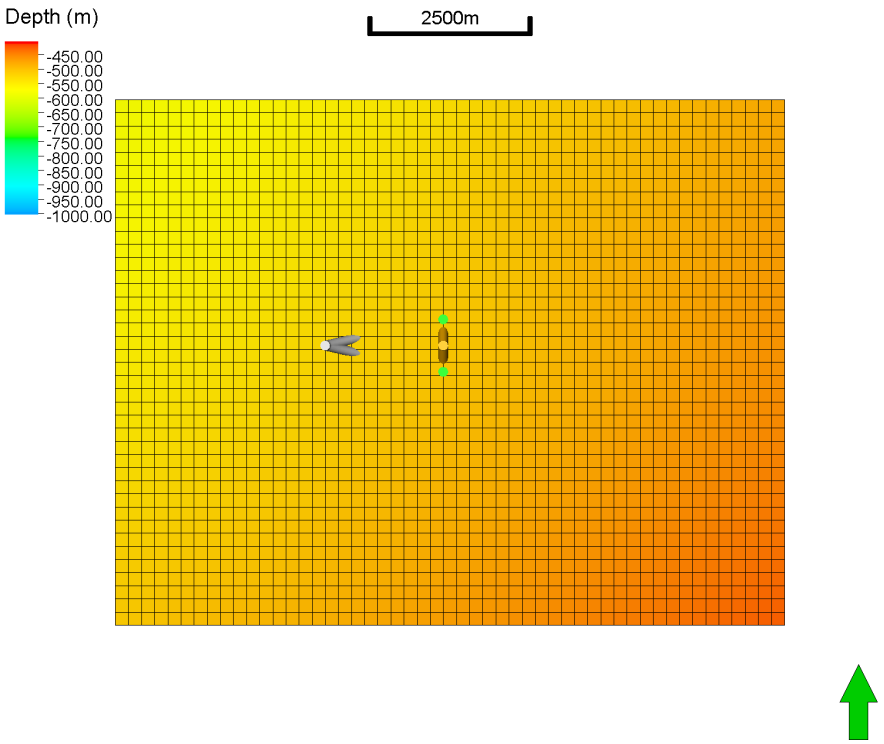

Fig. 3.7: Wellhead locations. Top depth of full reservoir is displayed in the background

Tab. 3.1: Well and screen geometries of wells in the full reservoir (Figure 3.5). Production and injection wells are mirrored thus have the same depth, trajectory length and inclination

Well type	Maximum depth (m-TVD)	Trajectory length (m-MD)	Inclination (degrees)	Screen interval prod. well (m-MD)	Screen interval inj. well (m-MD)
Vertical	910	910	0	550 - 850	540 - 840
Inclined	910	1150	45	650 - 1060	640 - 1050
Horizontal	672	2800	60 - 90	1500 - 2800	1500 - 2800

Tab. 3.2: Well and screen geometries of wells in the GH reservoir (Figure 3.6). Production and injection wells are mirrored thus have the same depth, trajectory length and inclination

Well type	Maximum depth (m-TVD)	Trajectory length (m-MD)	Inclination (degrees)	Screen interval prod. well (m-MD)	Screen interval inj. well (m-MD)
Vertical	910	910	0	730 - 900	720 - 890
Inclined	910	1080	39	850 - 1060	840 - 1050
Horizontal	810	2800	60 - 90	1800 - 2800	1800 - 2800

3.2 Results

In this section, the results from the dynamic simulation study in the Harderwijk case study area can be found, shown as plots, images and tables. Additionally, the salinity data from Griffioen et al. (2016) and TNO (2015) are combined and plotted. A best fit line is found through the data, which is used as input for the dynamic model.

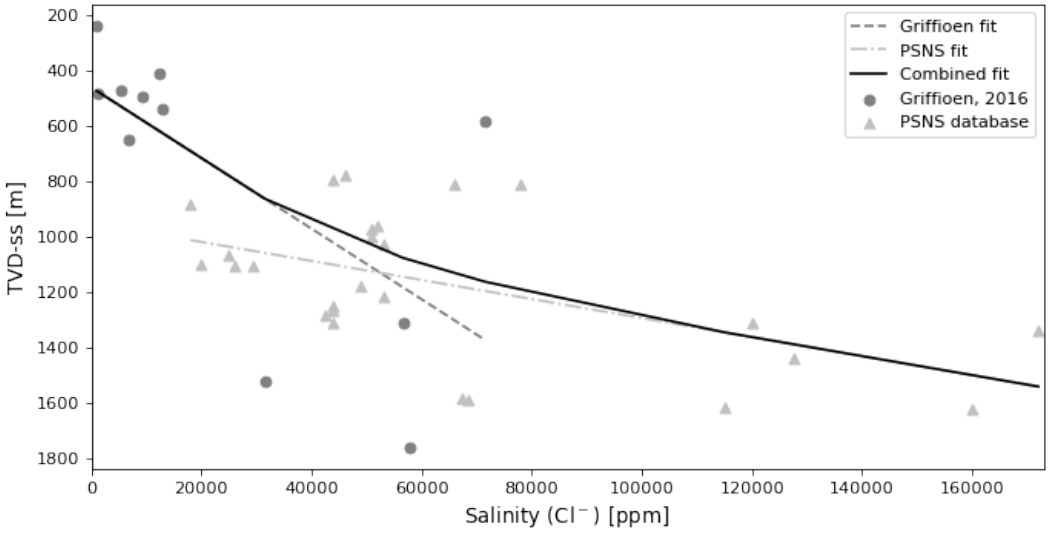

Fig. 3.8: Salinity (expressed in Cl^- concentration) at different depths. Two data sets are used (Griffioen et al., 2016 & TNO, 2015). The combined fit is used as input for deriving fluid properties at a certain depth

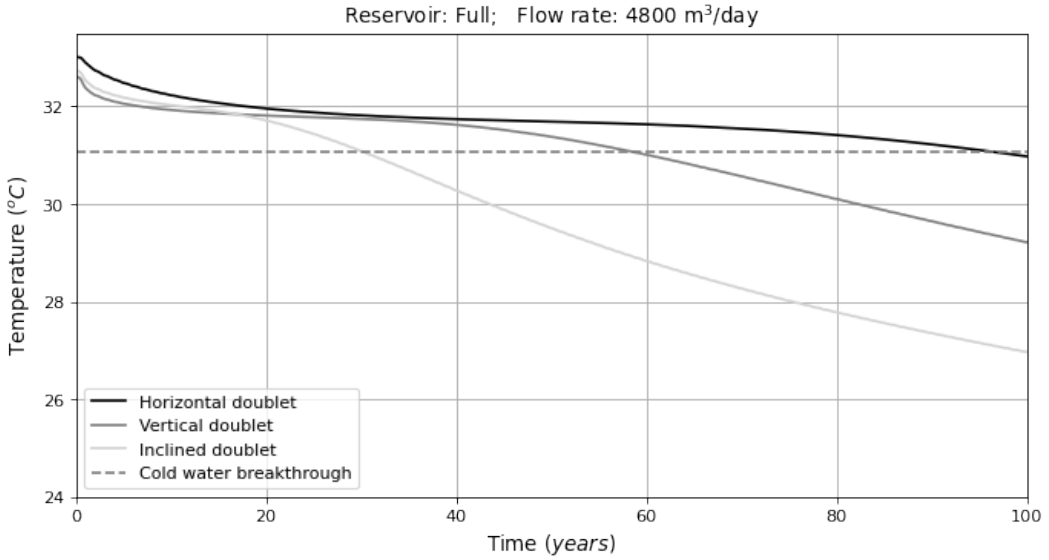

Fig. 3.9: Production temperature change in the full reservoir over 100 years of production with 4800 m^3/day flow rate for every doublet. The cold water break through is indicated when 2% decrease in plateau temperature is reached

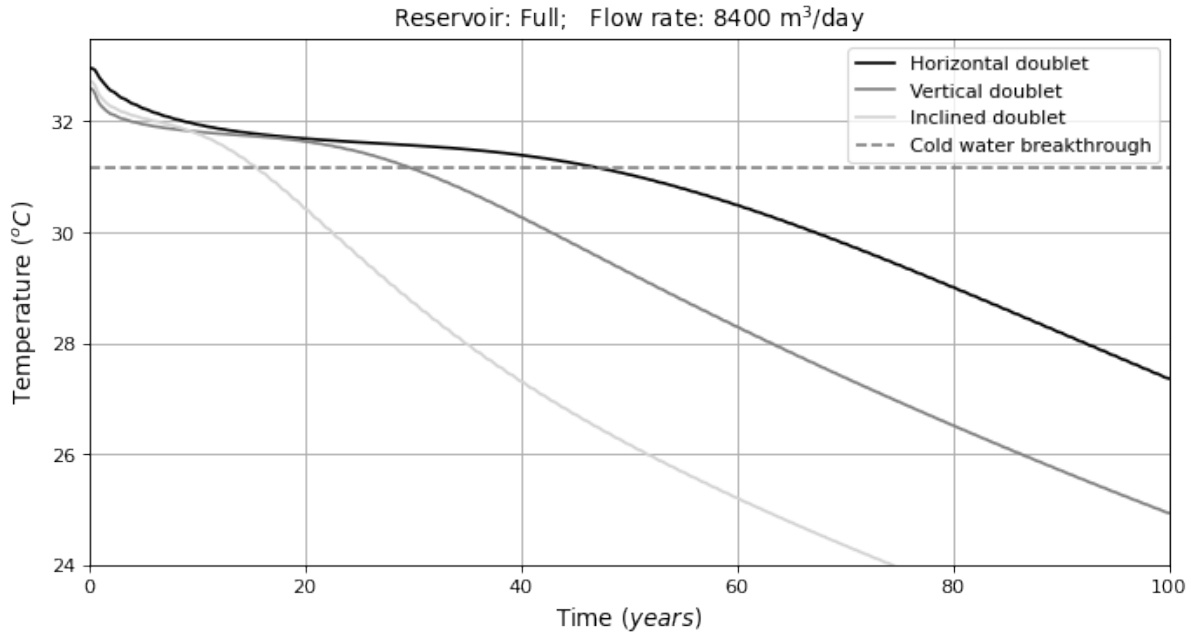

Fig. 3.10: Production temperature change in the full reservoir over 100 years of production with 8400 m^3/day flow rate for every doublet. The cold water break through is indicated when 2% decrease in plateau temperature is reached

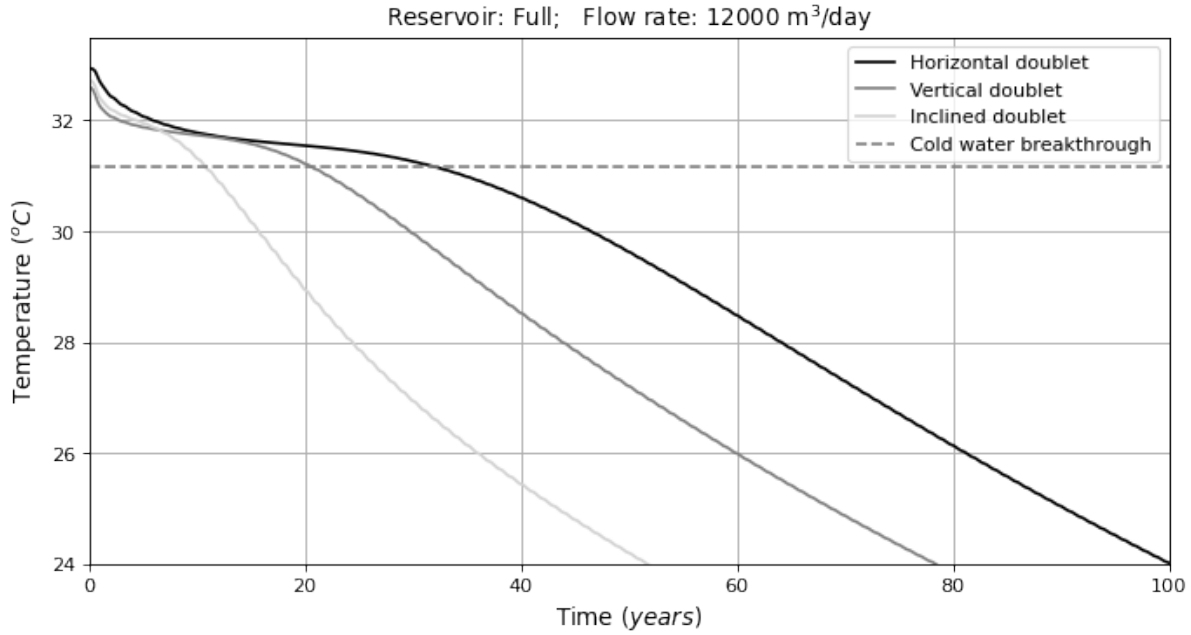

Fig. 3.11: Production temperature change in the full reservoir over 100 years of production with 12000 m^3/day flow rate for every doublet. The cold water break through is indicated when 2% decrease in plateau temperature is reached

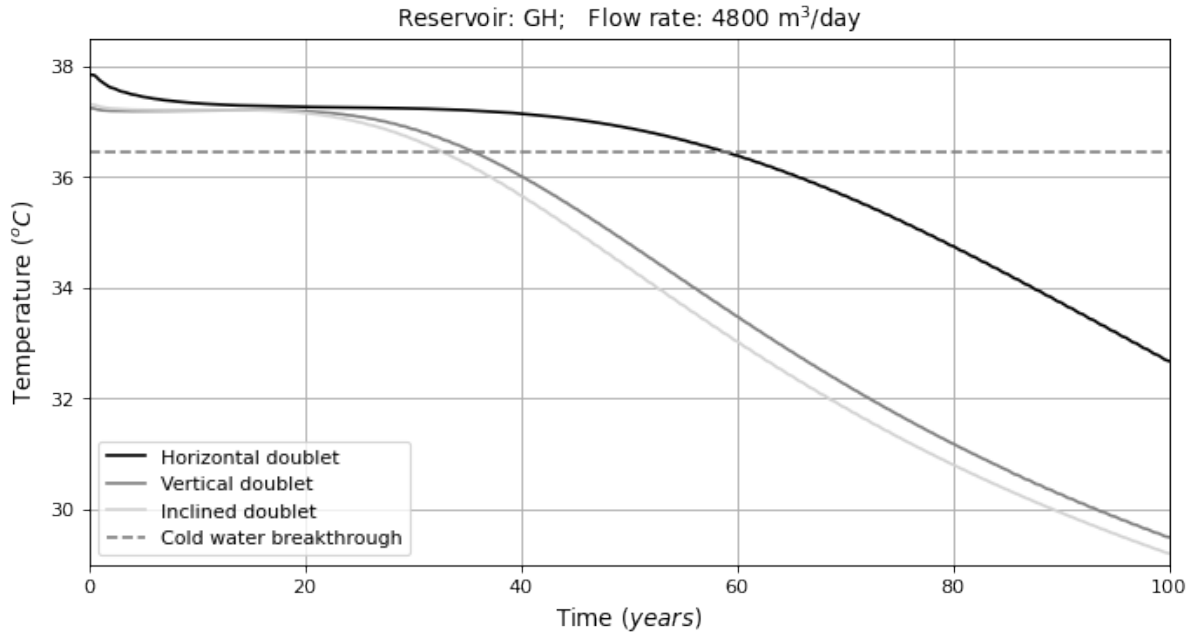

Fig. 3.12: Production temperature change in the GH reservoir over 100 years of production with 4800 m^3/day flow rate for every doublet. The cold water break through is indicated when 2% decrease in plateau temperature is reached

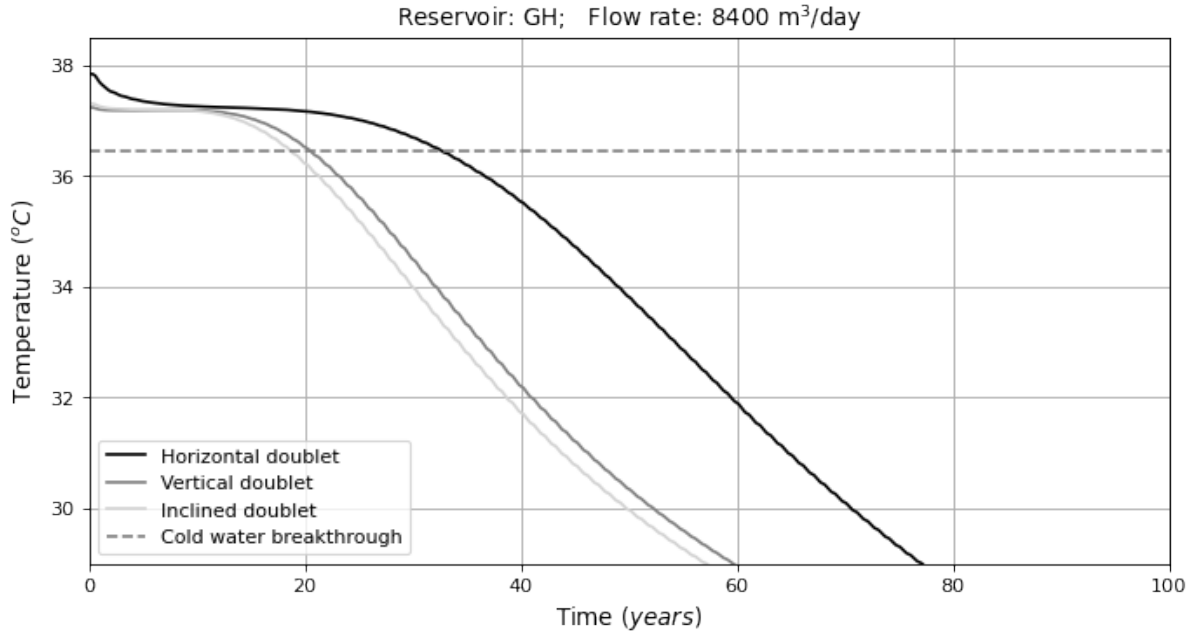

Fig. 3.13: Production temperature change in the GH reservoir over 100 years of production with 8400 m^3/day flow rate for every doublet. The cold water break through is indicated when 2% decrease in plateau temperature is reached

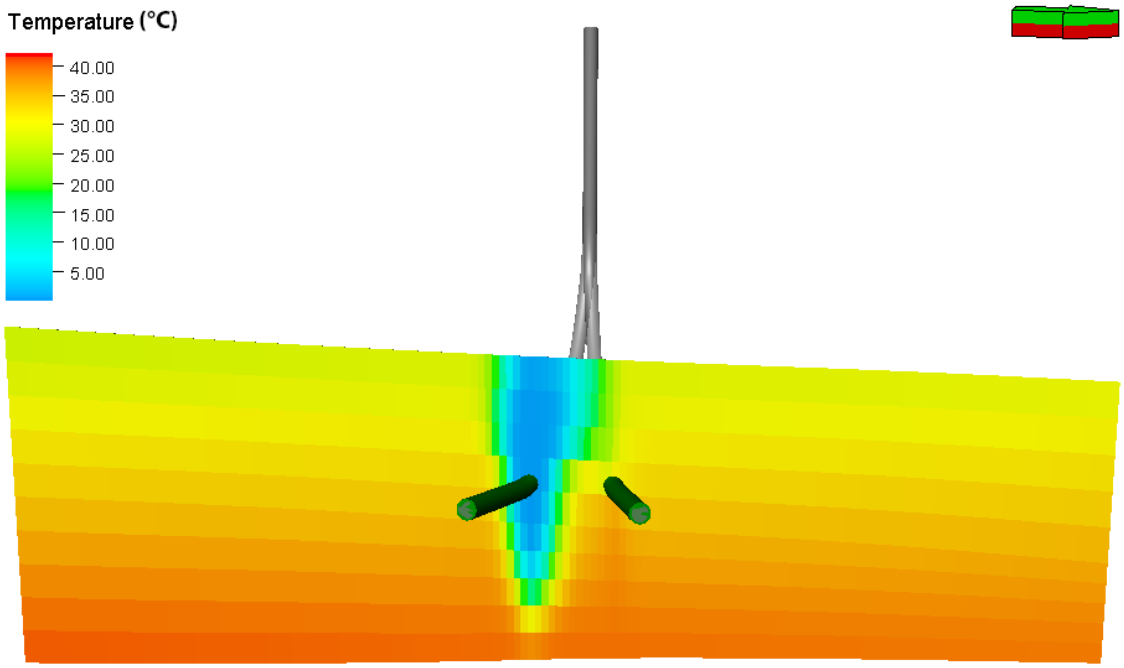

Fig. 3.14: Cold water plume for horizontal well configuration in the full reservoir. The figure shows the plume at the cold water breakthrough moment. The view is south - north

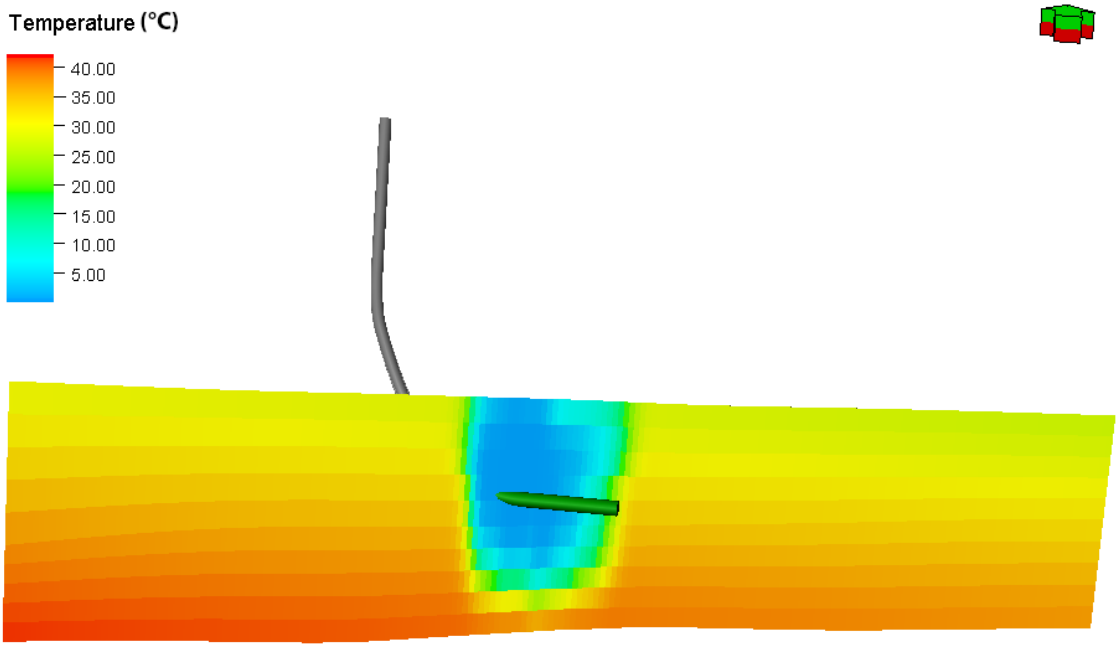

Fig. 3.15: Cold water plume for horizontal well configuration in the full reservoir. The figure shows the plume at the cold water breakthrough moment. The view is east - west

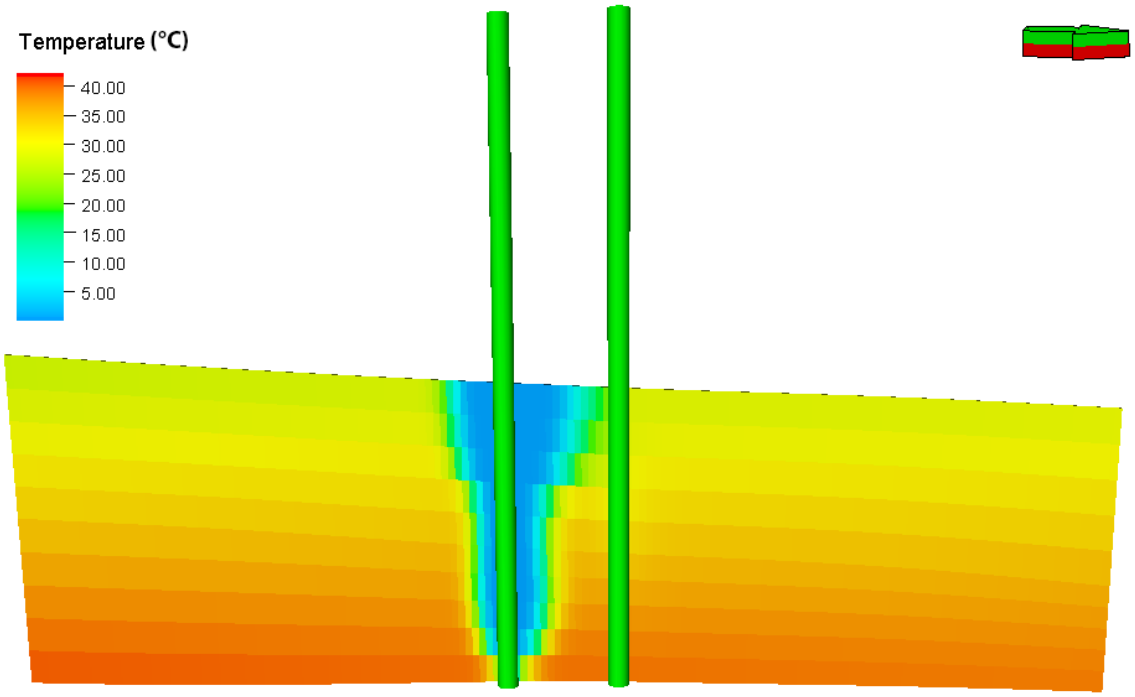

Fig. 3.16: Cold water plume for vertical well configuration in the full reservoir. The figure shows the plume at the cold water breakthrough moment.

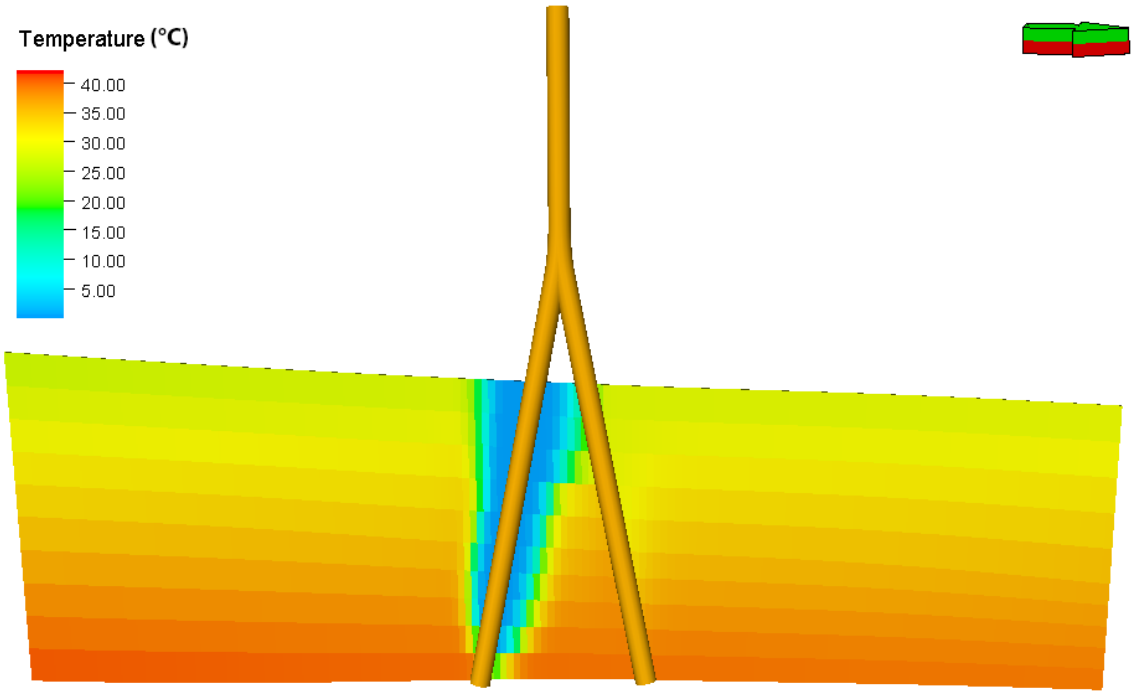

Fig. 3.17: Cold water plume for inclined well configuration in the full reservoir. The figure shows the plume at the cold water breakthrough moment.

Tab. 3.3: Results from **full reservoir** simulation for different well trajectories and various flow rates. The cold water breakthrough is defined as the year when production temperature has decreased with 2% relative to the plateau production temperature

Well type	Production / injection rate (m^3/day)	Plateau production temperature (°C)	Cold water breakthrough (years)	Injection temperature (°C)
Horizontal	4800	31.9	97	10
Vertical	4800	31.9	59	10
Inclined	4800	31.9	30	10
Horizontal	8400	31.8	52	10
Vertical	8400	31.8	30	10
Inclined	8400	31.8	16	10
Horizontal	12000	31.7	36	10
Vertical	12000	31.7	21	10
Inclined	12000	31.7	11	10

Tab. 3.4: Results from **GH reservoir** simulation for different well trajectories. The cold water breakthrough is defined as the year when production temperature has decreased with 2% relative to the plateau production temperature

Well type	Production / injection rate (m^3/day)	Plateau production temperature (°C)	Cold water breakthrough (years)	Injection temperature (°C)
Horizontal	4800	37.2	59	10
Vertical	4800	37.2	36	10
Inclined	4800	37.2	33	10
Horizontal	8400	37.1	34	10
Vertical	8400	37.1	21	10
Inclined	8400	37.1	20	10

3.3 Discussion

The results from this chapter show predicted flow rates and doublet lifetimes for the two reservoir scenarios, considering three different well trajectories and varying flow rates. The results give valuable insights into the geothermal potential of the Breda Formation and optimal well design. Still, certain assumptions and simplifications had to be made in order remain within the scope of this thesis. These assumptions and simplifications will be discussed in detail in this section.

Flow rates

Very high production rates can be sustained by the full reservoir at Harderwijk, due to the large thickness and high permeability. Simulated flow rates of up to 12000 m^3/day are recorded, maintainable in both the injection and production wells. The limiting factor in this scenario will be the erosional effects on the well barriers and in the ESP. It is debatable whether such flow rates could be sustained by the ESP. The highest fluid velocity is recorded at the small pump annulus (Blinovs & Van Og, 2022), which would erode very quickly under high flow rates. ESP selection and corresponding rate control is left outside the scope of this study.

Doublet lifetimes

The simulated doublet lifetimes are relatively long, especially for 4800 m^3/day flow rate in both reservoir scenarios (Figure 3.9; Figure 3.12) and for 8400 m^3/day flow rate in the full reservoir scenario (Figure 3.10), while the well spacing is on the short side at 800 m horizontal distance. This might be explained by the large reservoir thicknesses, being roughly 350 and 550 m in the thickest parts of the GH and full reservoir, respectively. For the full reservoir it is, however, uncertain to what extend the full 550 m thickness can be regarded as a single reservoir, especially when considering the 'high GR interval' in the middle of the cube (as discussed earlier). Moreover, the under- and overburden are not included in the static and dynamic model, but are replaced by 2D impermeable boundaries instead. Incorporating the underlying Veldhoven Formation and overlying Oosterhout Formation allows for modelling the conductive heat flow from these formations into the Breda aquifer, which should lead to even longer doublet lifetimes due to enhanced thermal recharge.

The horizontal configurations show the longest doublet lifetimes in both reservoir scenarios. This is likely due to the cold water flowing into the reservoir at roughly the same rate all along the well screen (see Figure 3.15), whereas the main flow in the vertical and inclined wells is happening at the top of the reservoir, between the top inlets of the injection and production screens (see Figures 3.16 & 3.17). This causes the cold water

to spread over a larger area when injecting horizontally compared to the other well scenarios, which means that the cold front takes longer to reach the production well. A downside to this is that the horizontal wells have a larger radius of influence, so less projects can be fitted in and this can be an environmental concern. Moreover, horizontal wells are more costly to drill compared to inclined wells, due to the longer well path and the additional tools needed to drill horizontally. Vertical wells are likely even more expensive since two drilling locations are requiered. A rigorous financial comparison was left outside the scope of this thesis project, but is essential when determining the final design of a doublet system. Before a certain configuration can be selected, it should be known whether or not potential increased flow rates result in enough additional revenue to compensate for higher investment costs.

The lifetime result from the inclined doublet in the full reservoir is an outlier, since it shows an earlier cold water breakthrough for 4800 and 8400 m^3/day flow rates compared to the same flow rates in the GH reservoir. This is unexpected since in general a larger reservoir should sustain a longer lifetime, as is observed for the other configurations. Why this doesn't apply for the inclined configuration in these cases could be due to the chosen screen interval. As can be seen in Figure 3.17, the top of the screens in the production and injection wells are relatively close horizontally, while the bottom end of the screens are relatively far apart. The early break through is caused by cold water reaching the top of the production screen after 30 years for the 4800 m^3/day case (Figure 3.9). Lifetime could be increased if the top inlet were lowered to the point where it matches the horizontal spacing of the vertical doublet. By doing so, the total screen length would shorten, decreasing the potential maximum flow rate. However, this might not be a problem for the full reservoir scenario since very high flow rates can be sustained anyway, as discussed above. Lowering the screens will also result in higher production temperatures. In this study the screens are configured such that the initial plateau production temperatures are similar, to be able to compare the lifetimes.

In the GH reservoir, the inclined doublet lifetime is only a few years earlier compared to the vertical doublet lifetime. In this case, the operator could choose the inclined configuration over the vertical one despite the negligible shorter lifetime, due to much lower CAPEX for drilling inclined wells from a single location compared to drilling two vertical wells from different locations.

Permeability

The horizontal and vertical permeability are assumed to be equal (isotropic permeability), as mentioned in the Discussion section in the previous chapter (section 2.3). This assumption could turn out to be faulty however due to geological heterogeneities. Possible heterogeneities could be induced by deltaic structures such as switching delta lobes, cemented horizons or mud drapes (described in section 1.4.1). Other possible heterogeneities are laminated clay layers or impermeable horizontal streaks, such as found in the BSM, which could impede vertical flow. Generally, such heterogeneities obstruct

vertical flow more than horizontal flow due to their predominantly horizontal geometry. Therefore, the most probably alternative scenario is that the vertical permeability is lower than the horizontal permeability. Such a scenario won't have detrimental effects on the vertical and inclined wells, since most flow happens horizontally between the injection and production screens (see the cold water plumes in Figures 3.16 & 3.17). Moreover, if a low permeable zone is encountered somewhere along the well path, flow can still happen through other parts of the screen further down or up. On the other hand, limited vertical permeability can have a profound effect on the lifetime, flow rate and well spacing of horizontal configurations, since much of the flow happens not only horizontally, but vertically as well (as can be seen by the cold water plumes in Figures 3.14 & 3.15). Also, if a horizontal injection well happens to be drilled in a low permeable zone (through a horizontal clay layer for example), the well might not be able to inject water at all.

Injection temperature

The assumed constant injection temperature of 10 °C is not realistic due to fluctuating heat demand. During summer, the heat demand will be less and the return temperature will be higher. During winter, 10 °C return temperature is a fair assumption. For more accurate simulation results, the injection temperature should vary over time, which is not included in this study.

Application to other regions

The results from the dynamic study apply to the Harderwijk study area, and can also be extrapolated to the other regions with high transmissivity (>500 Dm) within the ZZL. The conditions in the Breda Formation outside the ZZL are however not part of this study and could be completely different. To illustrate this, look at the differences for transmissivity within the ZZL (Figure 2.39). Therefore one must be careful when trying to extrapolate the results from this area to other parts of the formation, or entirely different formations for that matter.

3.4 Sub-conclusion

The salinity of the formation water in the ZZL is not known, because no direct measurements are taken in this location. Therefore, the salinity is estimated by combining data from different locations in the Netherlands. Figure 3.8 shows the data points used and a general trend line which could be fitted through the points. In general, it can be concluded that the salinity increases with depth in the Netherlands.

The dynamic simulation results show that for most well configurations, the full reservoir has a longer lifetime compared to the smaller GH reservoir. This is to be expected, since the full reservoir is much thicker compared to the GH reservoir. In general, both the full and GH reservoirs are ideal reservoirs that can sustain high flow rates as well as long doublet lifetimes.

All well designs show good performance in terms of possible flow rates and lifetimes, however the horizontal trajectory is superior in terms of doublet lifetime in all scenarios over the vertical and inclined configurations. The horizontal configurations therefore seem to be the best option, however this is only valid if the permeability is indeed isotropic, as assumed in this project, and the increased flow rate provides enough revenue to compensate the high investment costs.

The results from this chapter can relatively safely be extrapolated to the other parts of the Breda Formation within the ZZL where there is a high (>500 Dm) transmissivity. In the parts with lower (<500 Dm) transmissivity, the horizontal trajectory is expected to be superior as well since horizontal wells are especially suitable for thin formations, due to the possibility of long screens. Outside the ZZL, more research is needed to confirm whether similar well designs are suitable. Still, it can be concluded that if a certain hypothetical reservoir has (roughly) isotropic permeability, a similar horizontal configuration as used in this thesis results in much longer doublet lifetimes compared to vertical and inclined configurations, no matter where this reservoir is situated. On the other hand, if the hypothetical reservoir has anisotropic permeability, a horizontal configuration is much less effective.

Chapter 4

Legal aspects

The final objective of this thesis is to analyse the Dutch legal framework regarding medium deep geothermal. A legal framework consists of a series of legal documents declaring the rules, rights and obligations of parties involved in a project. The aim of this section is to explore the Dutch legal framework on medium deep geothermal exploitation and how this compares to other EU countries regarding this topic, with the goal of obtaining a better insight into how the Dutch law accelerates or hampers medium deep geothermal growth. Other countries are evaluated in order to find out the differences and whether there are any lessons which can be learned from them.

4.1 Method

To determine the effect of legislation on medium deep geothermal development, literature and legislative documents are evaluated and summarized in this section. The relevant Dutch legislation is outlined first, followed by a selection of EU countries. This evaluation finally results in a graphical overview of the varying legislation per country shown in Figure 4.1.

4.1.1 Dutch law (Netherlands)

The Dutch law makes a distinction between projects above 500 m depth and those below. Any operations <500 m depth are subject to the Water Law (Waterwet), while projects >500 m must adhere to the Mining Law (Mijnbouwwet) (Van Beek et al., 2014).

The Dutch Water Law is under the authority of the province. It poses limited prerequisites for drilling shallower than 500 m. Standard water drilling techniques can be applied here (Hellebrand et al., 2012). Provincial policy states that current rules regarding WKO systems ('Warmte- koudeopslag', which roughly translates to Underground Heat Storage or UTES) apply to shallow geothermal as well (Van Beek et al., 2014).

The Dutch Mining Law is under the authority of the ministry of Economic Affairs and Climate (EZK). With depth, the risk of encountering oil and gas combined with regions of high pressure increases. Therefore, any drilling operation deeper than 500 m must

adhere to very strict regulations regarding well design and drilling method. Satisfying these regulations is quite costly (Hellebrand et al., 2012).

4.1.2 Other EU countries

The rules and regulations surrounding (low enthalpy) geothermal differ largely between EU countries. Some countries don't have specific laws regulating geothermal energy yet. Other countries do have laws, but don't distinguish between geothermal types in their legal framework or they are contradictory (EGEC, 2012). In this section, legislation and regulations which apply to the medium depth in several EU countries are listed per country.

Germany
In Germany, all activities above 100 m depth are regulated by the Water Law, authorized by the states. Therefore only very shallow geothermal applications, like ground source heat pumps (GSHP) fall under this law (EGEC, 2012). Below 100 m depth, a mining license must be obtained, according to the Federal Mining Act (Bundesberggesetz). Such a license gives the right to extract water from any depth below a given surface (EGEC, 2012).

Italy
Italy distinguishes geothermal sources not based on depth, but solely on enthalpy. All deposits with extracted water below 90 ^{o}C are considered low enthalpy. Those between 90-150 ^{o}C are categorized as medium enthalpy and above 150 ^{o}C as high enthalpy. Low enthalpy geothermal operations are exempted from national mining regulations. Instead, these are delegated to the regulations of the provinces (Somogyi et al., 2017).

France
France, like Italy, bases their definition on low and high enthalpy geothermal. Low enthalpy is characterized by those deposits with water surface temperature equal to or below 50 ^{o}C. High enthalpy deposits comprise all others (EGEC, 2012). Geothermal resources above 100 m depth and with $<$20 ^{o}C temperatures are exempted from declaration and authorisation. Low enthalpy deposits with drilling operations below 100 m depth are ruled by the Mining Code (prefect). Any operation which falls out of the scope of the Mining Code is ruled by the Environmental Code or Water Law (national government/prefect). An environmental impact study must be done before the project commences, however projects below 1 million € are granted a simplified procedure. Different taxation concepts apply to geothermal projects in the Paris and Aquitaine basin (EGEC, 2012).

Spain
Spain has four enthalpy based categories to distinguish between geothermal types: Very low ($<$25 ^{o}C), Low (25-100 ^{o}C), Medium (100-150 ^{o}C) and High ($>$150 ^{o}C). Any drilling operation below 20 m depth must obtain permission from the mining authorities. Additionally, a license is needed from the water authorities to be able to extract water

(Somogyi et al., 2017). Furthermore, all geothermal types are regulated by the Mines Act, which is under the authority of the national government (Garcia-Gil, 2019).

Ireland
Low temperature, shallow geothermal resources are defined up to a depth of 400 m, approximately (DECC, 2020). As stated by the EGEC (2012), there is no legal framework for shallow, medium and deep geothermal energy in Ireland. There are regulations for hydrocarbon and mineral exploration boreholes, although it's likely that geothermal exploration isn't affected by those. More recently, the Department of the Environment, Climate and Communications published a roadmap towards a policy and regulatory framework for geothermal energy in Ireland (DECC, 2020; updated in Jan 2021). Again this document states that Ireland currently has no specific legislation or regulatory framework covering geothermal and no process for licensing, exploration or development of geothermal resources. It does provide a strategy on the steps needed to realize new policy and regulatory framework for geothermal energy. Implementation of this framework is planned to start in 2022.

Hungary
According to the EGEC (2012), there are several laws covering geothermal energy in Hungary: The Mining Law (or Gas Law), Water Management Law and Concession Law. The legislation on Environment and Water states that water produced from an aquifer with a surface outflow temperature of more than 30 ^{o}C is characterized as 'thermal water'. The Mining Law covers the exploitation of these waters. Licensing is the authority of The Hungarian Bureau of Mines. Below 30 ^{o}C, no licensing is needed, making it easier to exploit these shallow geothermal resources. However much of the legislation covering geothermal energy are incomplete or contradicting. According to Toth (2015), calculated energy policy and a complementary legal and financial framework needs to be implemented in order for the geothermal industry to start developing.

Poland
In Poland, geothermal resources are classified within two categories: Low enthalpy ($<$150 ^{o}C at 1 km depth) and High enthalpy ($>$150 ^{o}C at 1 km depth) (Sowiżdżał et al., 2019). Before 2012, no specific regulations regarding geothermal heat production were present, only general acts referring to numerous aspects of geothermal exploitation were in place. The Geological and Mining Law wasn't adequate regarding geothermal. (EGEC, 2012). Since then, modifications to this law were adopted. Most importantly, acquiring a geothermal concession has been simplified from a 3-stage to a 1-stage process. Furthermore, the State Resources Policy has been composed which aims to bolster the geothermal industry in Poland (Sowiżdżał et al., 2019).

4.2 Results

The results from the comparative legal study are graphically shown in the figure below.

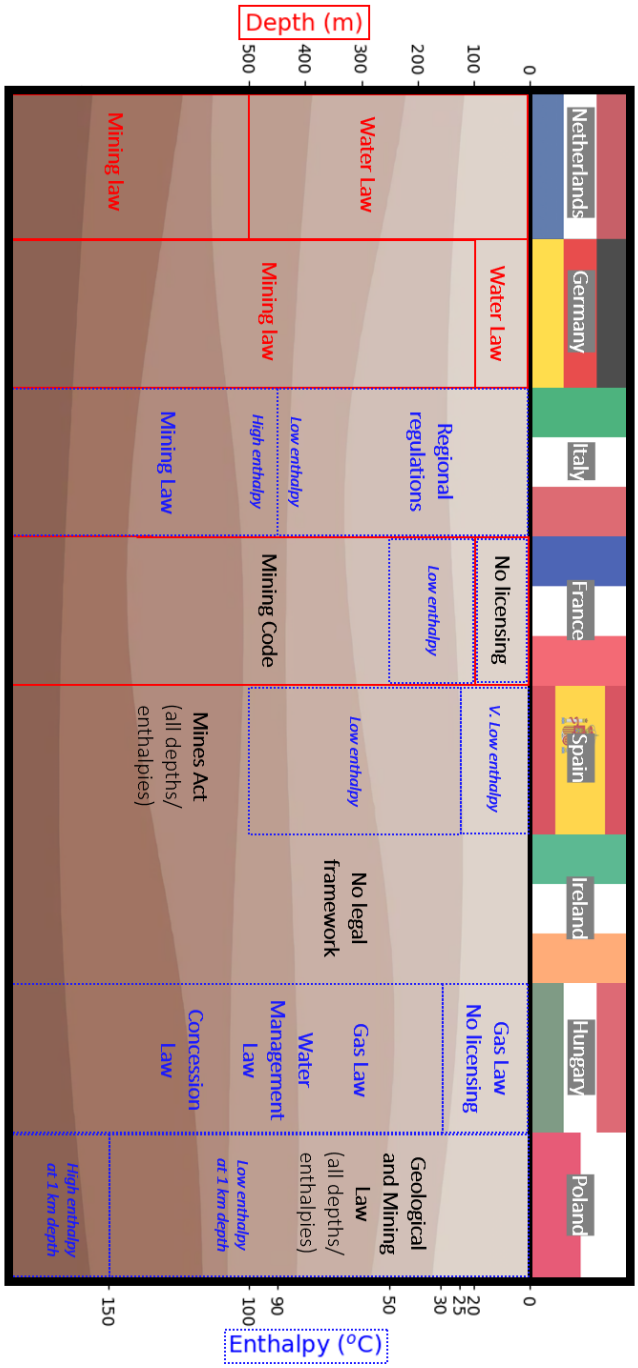

Fig. 4.1: Comparison between the analysed EU countries regarding their subsurface legislation which apply to the medium depth, shown graphically. The red, solid boxes represent depth-based legislation, while the blue, dotted boxes represent enthalpy-based legislation

4.3 Sub-conclusion

The current Dutch legal framework surrounding medium deep geothermal is divided into two separate laws, the Water and Mining Law. The application of these laws are limited by depth: all operations above 500 m depth are subject to the Water Law, while projects below 500 m depth are governed by the Mining Law. As mentioned in the problem statement (section 1.2), this rigid boundary could pose problems for aquifers crossing this boundary, such as the BSM shown in Figure 1.2, since two different laws will apply within the same aquifer. Both laws pose different rules for for the well design. The Breda Formation in the ZZL also crosses this boundary, as shown on the depth maps in section 2.2. This is also applies in the Harderwijk case study area. The top of the full reservoir is situated between 405 in the SE and 550 m TVD in the NW (see Figure 3.2). Therefore, it intersects with the 500 m boundary, which means that both the Mining and Water Law apply within this reservoir. This could pose problems since the operator must adhere to both laws, which implies that setting up a geothermal project in the Harderwijk area is, in practice, not feasible. It can therefore be concluded that in this regard, the current Dutch legislation does not enable, let alone accelerate medium deep geothermal development. If the full potential of the medium depth is to be accessed, a revision of the legislative 500 m depth boundary should be considered.

The comparative study, graphically shown in Figure 4.1, shows that EU countries define their subsurface legislation differently with little to no consensus. Some use a depth based, some an enthalpy based, and some have no legal framework for geothermal exploitation at all. The country which seems to have the most sophisticated framework is France. France defines its geothermal deposits not based on depth, but on enthalpy. Additionally, projects above 100 m depth and below 20 ^{o}C temperatures are exempted from declaration and authorisation. Those below 100 m depth are ruled by the Mining Code. Implementing a similar framework in the Netherlands would already lift the most pressing issue for medium deep geothermal projects by moving the 500 m boundary to 100 m. Another interesting feature of the French legislation is the different taxation concepts for geothermal projects in certain basins. Legislation per basin is rarely used in the EU, however from a geological point of view it makes more sense to define legislation per basin instead of implementing a rigid horizontal boundary for the entire country.

Chapter 5

Final conclusion

The research questions posed at the start of this thesis were defined as follows:

1. What are the reservoir characteristics of the Breda Formation
    - Where are the high potential areas?
    - How good are the current (seismic) interpretations of the bounding surfaces of the Breda Formation, and can these be improved using new/old (seismic) data?
    - Are the existing well log data within the Breda Formation sufficient for creating a static reservoir model?
    - If a static model can be created, what are the potential production rates from the reservoir?
2. What is the optimal well design for medium deep wells?
    - What are the optimal well configurations for the Breda Formation specifically and medium deep geothermal in general?
    - What is salinity of the formation water in the Breda Formation?
3. How is the current Dutch legislation for medium deep geothermal defined and how does this enable or limit medium geothermal development?
    - How do the Dutch rules compare with other EU countries?

Question 1: Breda reservoir characteristics and potential production rates
The results from this thesis show that the Breda Formation in the ZZL is a very promising medium deep reservoir. The geological potential is especially well-developed in south-east Flevoland, northwest Gelderland and northeast Utrecht, where the transmissivity is highest. In this region, attention must be paid to drilling-free zones, drinking water and preserved nature areas (see Appendix C). Still, this formation can become a realistic target for geothermal exploitation.

Prior to this study, the only spatial interpretation of the Breda Formation was present in the REGIS model, based on interpolations between shallow wells. Most shallow wells have a TD between 200 to 300 m TVD, and never deeper than 500 m due to Mining Law legislation. Moreover, the spread of the shallow wells is highly anisotropic due to variations in the top depth of the formation. This makes the interpreted Breda Formation in REGIS questionable. The only previously existing seismic interpretation is included in the DGM Deep model, being the base of the Upper North Sea Group corresponding to the EMU. The results from the seismic interpretation in this study can be compared to the

currently present interpretations from REGIS. The base Breda in REGIS is comparable to the EMU interpretation from this study. The MMU and LMU interpretations show larger differences when comparing them to the mid and top Breda in REGIS. For example, the deepest part of the mid Breda (southern Flevoland and Markermeer) in REGIS is somewhere between 600 - 700 m depth, while the MMU from this study is between 850 and 950 m deep in this area. Moreover, the top Breda in REGIS is situated at maximum 600 m depth in Noord-Holland, while the LMU from this study goes up to 850 m depth in this location. Lastly, the thickness maps show a roughly comparable distribution of high and low thickness areas, however the REGIS map shows a thicker succession in southern Flevoland (500 - 600 m thick) compared to the map from this study (400 - 500 m thick). Since the maps from this study are generated using much more (types) of data, the new maps can be considered as (slight) improvements.

A static reservoir model of the Breda Formation could be created from the available well logs in the ZZL. The results give a good impression on the distribution of high and low potential areas and the reservoir capabilities of this formation. However, large uncertainties are embedded in the well log analysis, since no permeability measurements from cores or cuttings are present. The calculated permeability is relatively high, reaching up to 4-5 Darcy in some locations. Only the NDN-120 well test provides some degree of calibration value, albeit this well only penetrates the top part of the formation. Additional data are needed to verify and calibrate the petrophysically derived values, preferably data from cores.

Another source of uncertainty on petrophysically derived values is the glauconite content in the Breda Formation. It is evident that glauconite causes some degree of uncertainty to the calculated V_{cl} values, however quantifying this uncertainty is very hard and not feasible within the scope of this thesis. What can be concluded from the analysis of the cuttings is that while being present in quantities of up to 8%, glauconite influence in the ADK-GT-01 well is not that significant and it is overshadowed by other factors influencing the API response.

The dynamic simulation results show that both the full and GH reservoirs are ideal reservoirs that can sustain high flow rates as well as long doublet lifetimes. Production rates of 4800 and 8400 m^3/day can be sustained by either reservoir. 12000 m^3/day can be produced from the full reservoir from a geological point of view, however its disputable whether the ESP could handle correspondingly high fluid velocities.

Question 2: Optimal well design for medium deep wells
All well designs show good performance in terms of possible flow rates and lifetimes, however the horizontal trajectory is superior in terms of doublet lifetime in all scenarios over the vertical and inclined configurations. The horizontal configurations therefore seem to be the best option, however this is only valid if the permeability is indeed isotropic, as assumed in this project, and the increased flow rate provides enough revenue to compensate the high investment costs.

The results from the dynamic simulation chapter can relatively safely be extrapolated

to the other parts of the Breda Formation within the ZZL where there is a high (>500 Dm) transmissivity. In the parts with lower (<500 Dm) transmissivity, the horizontal trajectory is expected to be superior as well since horizontal wells are especially suitable for thin formations, due to the possibility of long screens. Outside the ZZL, more research is needed to confirm whether similar well designs are suitable. Still, it can be concluded that if a certain hypothetical reservoir has (roughly) isotropic permeability, a similar horizontal configuration as used in this thesis results in much longer doublet lifetimes compared to vertical and inclined configurations, no matter where this reservoir is situated. On the other hand, if the hypothetical reservoir has anisotropic permeability, a horizontal configuration is much less effective.

The salinity of the formation water in the ZZL is not known, because no direct measurements are taken in this region. Therefore, the salinity is estimated by combining data from different locations in the Netherlands. Figure 3.8 shows the data points used and a general trend line which could be fitted through the points. In general, it can be concluded that the salinity increases with depth in the Netherlands.

Question 3: Legislation
The current Dutch legal framework surrounding medium deep geothermal is divided into two separate laws, the Water and Mining Law. The application of these laws are limited by depth: all operations above 500 m depth are subject to the Water Law, while projects below 500 m depth are governed by the Mining Law. This rigid boundary could pose problems for aquifers crossing the boundary, such as the BSM shown in Figure 1.2, since two different laws will apply within the same aquifer. Both laws have different rules on well design. The Breda Formation in the ZZL also crosses the boundary, as is the case in the Harderwijk case study area. The top of the full reservoir is situated above 500 m TVD (see Figure 3.2), which means that both the Mining and Water Law apply within this reservoir. It can therefore be concluded that in this regard, the current Dutch legislation does not enable, let alone accelerate medium deep geothermal development. If the full potential of the medium depth is to be accessed, a revision of the legislative 500 m depth boundary should be considered.

The comparative study, graphically shown in Figure 4.1, shows that EU countries define their subsurface legislation differently with little to no consensus. Some use a depth based, some an enthalpy based, and some have no legal framework for geothermal exploitation at all. The country which seems to have the most sophisticated framework is France. France defines its geothermal deposits not based on depth, but on enthalpy. Additionally, projects above 100 m depth and below 20 ^{o}C temperatures are exempted from declaration and authorisation. Those below 100 m depth are ruled by the Mining Code. Implementing a similar framework in the Netherlands would already lift the most pressing issue for medium deep geothermal projects by moving the 500 m boundary to 100 m. Another interesting feature of the French legislation is the different taxation concepts for geothermal projects in certain basins. Legislation per basin is rarely used in the EU, however from a geological point of view it makes more sense to define legislation per basin instead of implementing a rigid horizontal boundary for the entire country.

Chapter 6

Recommendations for future research

In some cases, certain topics encountered during the project can not be investigated due to lacking time or data. In this chapter, such subjects which were found during this thesis are listed and discussed for future research.

Seismics

Seismic lines in the ZZL and LZT could be reprocessed which would make the interpretation of the shallow reflectors much more accurate. This is especially vital for the Breda Formation in the LZT. The entire volume of this basin is covered by 3D seismic cubes, however the shallow data quality is generally poor. Furthermore, if the LZT is to be interpreted, biostratigraphy needs to be done in order to verify the presence or absence of the GH and/or Diessen formations.

The southeastern extent (towards Apeldoorn) of the Breda Formation in the ZZL basin is left outside the area of interest because of limited seismic data in this region. The generated thickness maps, however, suggest that the formation could have a significant thickness around Apeldoorn as well. When more seismic data become available in this region, the area of interest could be enlarged to incorporate the region around Apeldoorn.

Geological aspects

There is uncertainty on the the extent of the sealing layer on top of the Breda Formation. The overlying Oosterhout Formation is very much underexplored. Only Coenen (1974) has determined that there is a sealing top layer within the Oosterhout Formation in the NDN-120 well, extending at least up to the WSP-01 well. Future research should focus on improving the interpretation of the thickness, composition and sealing capability of the Oosterhout and other overlying formations.

More research is needed on possible heterogeneities in the ZZL Breda Formation. No significant signs of heterogeneities were encountered during this research, however as described in section 1.4.1, the ZZL was part of a deltaic coast line which could have led to the deposition of large and small scale heterogeneities. Thin heterolithic layers can only be identified by high resolution methods, such as (high res.) well logs or cores. Currently, such data are scarce or not available in the Breda Formation.

Petrophysics

In order to improve knowledge on the effect of glauconite on the gamma ray log, more research is needed. From this study it could be concluded that glauconite did not have a profound effect on the gamma ray log in the ADK-GT-01 well, however the potassium concentration in the mineral structure was not determined. Future research could focus on directly relating potassium-glauconite content with gamma ray response, in order to quantify the 'clay effect'.

Once more porosity and permeability measurements from cores and/or cuttings become available, the porosity and permeability from the petrophysical analysis must be revisited for calibration, since currently no porosity calibration is possible and permeability calibration is only possible in well NDN-120 via well test permeability.

Surface conditions

In order to determine the ultimate potential of the Breda Formation in the ZZL, the geologic high potential areas must be compared to the surface heat demand, as well as any surface restrictions (as shown in Appendix C). Furthermore, the heat must be distributed by heat networks. New heat networks must be realised and integrated with already existing smaller scale networks. Building on this is the concept of a smart thermal grid, as described by (Schepers et al., 2018). Low temperature heat networks could directly be supplied with heat from medium deep formations, as well as a large variety of waste heat. Within the smart thermal grid concept, the heat source, being the Breda Formation in this case, can eventually be converted from a mere heat source into a high temperature aquifer thermal energy storage (HT-ATES), meaning that during summer, the reservoir can act as storage for heat as well. Shallow to medium deep aquifers are perfectly suited for this application, since the OPEX is lower compared to deeper aquifers, while the insulating capabilities are equal. In order to work out whether the Breda Formation would be suitable for this application, more studies are needed on local conditions and geological composition.

Dynamic simulation

An additional scenario could be possible where both the Oosterhout Formation and the 'high GR interval' are sealing boundaries. In this case, additional model runs could be conducted on the Diessen Formation separately. The Diessen Formation is generally thicker and has a higher permeability compared to the underlying GH Formation, so this could be an interesting reservoir under these assumptions.

In this thesis, only geological and technical factors (related to the geothermal doublets) are incorporated in the dynamic analysis. A financial evaluation could be included complementary to the dynamic part. The CAPEX and OPEX for the different well configurations are important in order to determine which system to choose. Moreover, many

more well scenarios could be simulated with more trajectory variations, varying screen length, spacing and configurations.

Legal aspects

The current horizontal legislative boundary at 500 m depth forms a barrier to medium deep geothermal development. The boundary could be replaced by a legislative framework specified laterally per basin and vertically by geologic group, subgroup or formation. This could be expanded by incorporating 'no BOP zones' in areas where no shallow gas is present, to lower CAPEX costs for drilling medium deep wells. A premise for this is that more knowledge on shallow gas presence must be acquired. A future study could focus on mapping all onshore shallow gas pockets, from which a no BOP zone map could be derived.

References

Akinsete, O. O., & Adekoya, D. A. (2016). Effects of Mud Filtrate Invasion on Well Log Measurements. *All Days*. https://doi.org/10.2118/184308-MS

Arntz, J., Oerlemans, P., Dinkelman, D., Zaadnoordijk, J. W., Koenen, M., Valstar, J., Beernink, S., & Schout, G. (2020). *Verkenning HTO* (tech. rep.). IF Technology, TNO, Deltares, KWR.

Asquith, G., Krygowski, D., Henderson, S., & Hurley, N. (2004). Gamma Ray Log. *Basic well log analysis*. American Association of Petroleum Geologists. https://doi.org/10.1306/Mth16823C3

Békési, E., Struijk, M., Bonté, D., Veldkamp, H., Limberger, J., Fokker, P. A., Vrijlandt, M., & van Wees, J.-D. (2020). An updated geothermal model of the Dutch subsurface based on inversion of temperature data. *Geothermics*, *88*, 101880. https://doi.org/10.1016/j.geothermics.2020.101880

Benedictus, T. (2007). *Determination of petrophysical properties from well logs of the offshore Terschelling Basin and southern Central North Sea Graben region (NCP-2A) of the Netherlands* (tech. rep.). TNO.

Blinovs, A., & Van Og, G. (2022). *Brussels Sand Feasibility Study WarmingUP Doublet* (tech. rep.). Well Engineering Partners.

Bokarev, A. Y., Yezersky, D. M., Filimonov, A. Y., Dubnitsky, I. R., & Vorobiev, V. V. (2021). An Example of Building a Petrophysical Model of Unconsolidated Gas-Saturated Laminated Sediments Using Advanced Wireline and Logging While Drilling Services. *Day 1 Tue, October 12, 2021*. https://doi.org/10.2118/206620-MS

Bond, L. J., Denslow, K. M., Griffin, J. W., Dale, G. E., Harris, R. V., Moran, T. L., Sheen, D. M., & Schenkel, T. (2010). *Evaluation of Non-Nuclear Techniques for Well Logging: Technology Evaluation* (tech. rep.). Pacific Northwest National Laboratory (PNNL). Richland, WA (United States). https://doi.org/10.2172/1006309

Bonté, D., Van Wees, J.-D., & Verweij, J. (2012). Subsurface temperature of the onshore Netherlands: new temperature dataset and modelling. *Netherlands Journal of Geosciences*, *94*(4), 491–515. https://doi.org/10.1017/S0016774600000354

Buckley, F. A., & Cottee, L. (2017). A petrophysical approach to the investigation of shallow marine geology. *Near Surface Geophysics*, *15*(4), 367–385. https://doi.org/10.3997/1873-0604.2017031

Carmichael, R. (1982). *Handbook of Physical Properties of Rocks* (Vol. 2). CRC Press Inc.

Coenen, M. (1974). *De in de "Naarden" 500 m Boring Aangetroffen Geologische Situatie* (tech. rep.). Rijks Geologische Dienst. https://www.nlog.nl/brh-web/rest/brh/document/974568270

Cox, J., & Raymer, L. (1977). The Effect Of Potassium-Salt Muds On Gamma Ray, And Spontaneous Potential Measurements. *All Days*. https://doi.org/10.2118/6540-MS

Dafalla, M., & Samman, A. (2016). Soil And Backfill Material Of Environmental Friendly Thermal Properties. *International Journal of GEOMATE*, *10*(22), 2083–2087.

De Haan, H., Ten Veen, J., Houben, S., & Kruisselbrink, A. (2020). *Mapping of the Brussels Sand Member in the Netherlands* (tech. rep.). TNO.

De Kruijf, M. (2019). *Quickscan geothermie Energielandgoed Wells Meer* (tech. rep.). IF Technology.

DECC. (2020). Geothermal Energy in Ireland - A roadmap for a policy and regulatory framework. www.decc.gov.ie

EGEC. (2012). Regulations For Geothermal Energy.

Eppelbaum, L., Kutasov, I., & Pilchin, A. (2014). Thermal Properties of Rocks and Density of Fluids. *Applied geothermics* (pp. 99–149).

Garcia-Gil, A. (2019). Current Legal Framework on Shallow Geothermal Energy Use in Spain. https://doi.org/10.20900/jsr20200005

Geel, C., De Haan, H., & Peters, E. (2022). *Characterisation and production of the Brussels Sand Member near Zwijndrecht Zuid* (tech. rep.).

Geel, C., & Foeken, J. (2021). *Formation Evaluation of the Brussels Sand Member in the Netherlands* (tech. rep.). TNO.

Geluk, M., Duin, E., Dusar, M., Rijkers, R. H. B., van den Berg, M. W., & van Rooijen, P. (1994). Stratigraphy and tectonics of the Roer Valley Graben. *Geologie en Mijnbouw*, *73*, 129–141.

Geoloil. (2012). How to calculate Petrophysicals Cutoffs. https://geoloil.com/petroCutoffs.php

Geothermie NL. (2020). *Industriestandaard duurzaam putontwerp voor aardwarmteputten* (tech. rep.). GNL, EBN.

Geothermie NL. (2022). Duurzaamheid en omvang. https://geothermie.nl/index.php/nl/geothermie-aardwarmte/geothermie-in-nederland/duurzaamheid-en-omvang

Gibbard, P., & Lewin, J. (2016). Filling the North Sea Basin: Cenozoic sediment sources and river styles. *Geologica Belgica*, *19*(3-4), 201–217. https://doi.org/10.20341/gb.2015.017

Gies, C., Struijk, M., Békési, E., Veldkamp, H., & van Wees, J.-D. (2021). An effective method for paleo-temperature correction of 3D thermal models: A demonstration based on high resolution datasets in the Netherlands. *Global and Planetary Change*. https://doi.org/10.1016/j.gloplacha.2021.103445

Griffioen, J., Verweij, H., & Stuurman, R. (2016). The composition of groundwater in Palaeogene and older formations in the Netherlands. A synthesis. *Netherlands Journal of Geosciences - Geologie en Mijnbouw*, *95*(3), 349–372. https://doi.org/10.1017/njg.2016.19

Hall, H. N. (1953). Compressibility of Reservoir Rocks. *Journal of Petroleum Technology*, *5*(01), 17–19. https://doi.org/10.2118/953309-G

Hellebrand, K., In 't Groen, B., & Post, R. J. (2012). *Kansen voor Ondiepe Geothermie voor de glastuinbouw* (tech. rep.). KEMA, DLV, IF. Arnhem. www.kema.com

Herngreen, G. F. W., & Wong, T. E. (2007). Geology of the Netherlands - Cretaceous. *Geology of the netherlands*.

Heslop, A. (1974). Gamma-ray Log Response Of Shaly Sandstones. *The Log Analyst*, *15*(05).

Hesse, R., & Schacht, U. (2011). Early Diagenesis of Deep-Sea Sediments. https://doi.org/10.1016/B978-0-444-53000-4.00009-3

Houben, A. (2022). *(Draft) Oligocene – Miocene palynostratigraphy of three wells in the Zuiderzee Low area: updating the stratigraphy of the Middle North Sea Group* (tech. rep.). TNO.

Kennedy, M. (2015). Petrophysical Properties. https://doi.org/10.1016/B978-0-444-63270-8.00002-5

Kuanyu Lin, R. (2021). *Comparative analysis of methods to determine permeability* (Doctoral dissertation).

Kurtz, A. D. (2013). *Determining Mineralogy from Traditional Well Log Data* (Doctoral dissertation). Marietta College. Marietta, Ohio.

Lucas, S. G. (2021). Biostratigraphy. *Encyclopedia of Geology*, 89–95. https://doi.org/10.1016/B978-0-08-102908-4.00076-X

Lyons, W. C. (2010). Formation Evaluation. *Working Guide to Reservoir Engineering*, 97–232. https://doi.org/10.1016/B978-1-85617-824-2.00002-2

Mahmoudi, M., Fattahpour, V., Nouri, A., Yao, T., Baudet, B. A., & Leitch, M. (2015). Oil Sand Characterization for Standalone Screen Design and Large-Scale Laboratory Testing for Thermal Operations. *Day 3 Wed, November 25, 2015*. https://doi.org/10.2118/178470-MS

Martinius, A. W. (2017). Multiscale Gilbert-type delta lobe architecture and heterogeneities: The case of the Roda Sandstone Member. *AAPG Bulletin*, *101*(04), 453–463. https://doi.org/10.1306/011817DIG17024

Munsterman, D. K., & Brinkhuis, H. (2004). A southern North Sea Miocene dinoflagellate cyst zonation. *Netherlands Journal of Geosciences / Geologie en Mijnbouw*, *83*(4), 267–285.

Munsterman, D. K., & Deckers, J. (2022). Biostratigraphic ages and depositional environments of the upper Oligocene to lower Miocene Veldhoven Formation in the central Roer Valley Rift System (SE Netherlands-NE Belgium). *Netherlands Journal of Geosciences*, *101*, e6. https://doi.org/10.1017/njg.2022.3

Munsterman, D. K., Ten Veen, J. H., Menkovic, A., Deckers, J., Witmans, N., Verhaegen, J., Kerstholt-Boegehold, S. J., Van De Ven, T., & Busschers, F. S. (2020). An updated and revised stratigraphic framework for the Miocene and earliest Pliocene strata of the Roer Valley Graben and adjacent blocks. *Netherlands Journal of Geosciences - Geologie en Mijnbouw*, *98*. https://doi.org/10.1017/njg.2019.10

Nimmo, J. (2013). Porosity and Pore Size Distribution. *Reference module in earth systems and environmental sciences*. Elsevier. https://doi.org/10.1016/B978-0-12-409548-9.05265-9

RGD. (1974). *Lithologic descriptions NDN-120 well* (tech. rep.). Rijks Geologische Dienst, Rijksinstituut voor Drinkwatervoorziening. NLOG.nl

Rijkswaterstaat. (2019). De Klimaatmonitor.

Rorato, R., Arroyo, M., Andò, E., & Gens, A. (2019). Sphericity measures of sand grains. *Engineering Geology*, *254*, 43–53. https://doi.org/10.1016/j.enggeo.2019.04.006

RVO. (2022). WKO-bodemenergietool. https://wkotool.nl/

Schepers, B., Scholten, T., Willemsen, G., Koenders, M., & de Zwart, B. (2018). *Weg van gas. Kansen voor de nieuwe concepten LageTemperatuurAardwarmte en Mijnwater* (tech. rep.). CE Delft, IF Technology. www.ce.nl

Schlumberger. (1989). *Schlumberger log interpretation principles* (Vol. 1). Schlumberger Educational Services.

Schlumberger. (2022). ECLIPSE Industry Reference Reservoir Simulator.

Scott, G. D. (1960). Packing of Spheres: Packing of Equal Spheres. *Nature*, *188*(4754), 908–909. https://doi.org/10.1038/188908a0

Sens, E. (2010). *Shallow Gas in the Dutch part of the Miocene Eridanos Delta* (tech. rep.). EBN, Utrecht University.

Slupik, A., & Janse, A. (2008). The geological record of the Breda Formation in the subsurface of the Island of Noord-Beveland (Province of Zeeland, The Netherlands) from the Colijnsplaat borehole (42G24-1): A sequence-stratigraphic approach. *Deinsea*, *2*.

SodM. (2013). Protocol bepaling maximale injectiedrukken bij aardwarmtewinning.

Soille, P., & Vincent, L. M. (1990). Determining watersheds in digital pictures via flooding simulations. In M. Kunt (Ed.). https://doi.org/10.1117/12.24211

Somogyi, V., Sebestyén, V., & Nagy, G. (2017). Scientific achievements and regulation of shallow geothermal systems in six European countries - A review. https://doi.org/10.1016/j.rser.2016.02.014

Sowiżdżał, A., Tomaszewska, B., & Chmielowska, A. (2019). Development of the Polish geothermal sector in the light of current possibilities of financial support for a geothermal investment. *E3S Web of Conferences*, *86*. https://doi.org/10.1051/e3sconf/201

Taheri, S., Ghomeshi, S., & Kantzas, A. (2017). Permeability calculations in unconsolidated homogeneous sands. *Powder Technology*, *321*, 380–389. https://doi.org/10.1016/J.POWTEC.2017.08.014

Ten Veen, J., Verweij, H., Donders, K., Geel, C., De Bruin, G., Munsterman, D., Verreussel, R., Daza Cajigal, V., Harding, R., & Cremer, H. (2013). *Anatomy of the Cenozoic Eridanos Delta Hydrocarbon System* (tech. rep.). TNO.

TNO. (2015). *Integrated pressure information system for the onshore and offshore Netherlands* (tech. rep.).

TNO. (2019). Digitaal Geologisch Model: DGM-diep. https://www.dinoloket.nl/digitaal-geologisch-model-dgm-diep

TNO. (2022a). Breda Formation. *Stratigraphic nomenclature of the netherlands*. TNO – Geological Survey of the Netherlands. http://www.dinoloket.nl/en/stratigraphic-nomenclature/breda-formation

TNO. (2022b). NLOG. https://www.nlog.nl/

TNO. (2022c). REGIS II: het hydrogeologische model. https://www.dinoloket.nl/ondergrondmodellen

TNO. (2022d). ThermoGIS. https://www.thermogis.nl/

TNO-GDN. (2022a). Formatie van Veldhoven. *Stratigrafische nomenclator van nederland*. http://www.dinoloket.nl/stratigrafische-nomenclator/formatie-van-veldhoven

TNO-GDN. (2022b). Oosterhout Formation. *Stratigraphic nomenclature of the netherlands*. http://www.dinoloket.nl/en/stratigraphic-nomenclature/oosterhout-formation

TNO-GDN. (2022c). Rupel Formation. *Stratigraphic nomenclature of the netherlands*. TNO – Geological Survey of the Netherlands. http://www.dinoloket.nl/en/stratigraphic-nomenclature/rupel-formation.

Toth, A. N. (2015). Hungarian Country Update 2010-2014. *Proceedings World Geothermal Congress*. https://www.researchgate.net/publication/297369483

Ugborugbo, O., & Rao, T. (2009). Impact of Borehole Washout on Acoustic Logs and Well-to-Seismic Ties. *All Days*. https://doi.org/10.2118/128346-MS

Van Beek, D., De Boer, S., Braakhekke, M., & Buik, N. (2014). *Kansen voor Hogetemperatuuropslag en Geothermie* (tech. rep.). IF Technology. Assen, Drenthe.

Van den Boogaard, M., & Hoetz, G. (2012). Shallow Gas Play in The Netherlands Takes Off.

Van Lochem, H., Ter Borgh, M., & Mijnlieff, H. (2019a). *Geological evaluation for the seismic acquisition programme for SCAN areas A (Noord-Gelderland and Zuidoost Flevoland) and B (Achterhoek and Zuid-Twente)* (tech. rep.).

Van Lochem, H., Ter Borgh, M., & Mijnlieff, H. (2019b). *Geological evaluation for the seismic acquisition programme for SCAN areas H (West-Friesland) and I (Noordoostpolder)* (tech. rep.).

Van Vliet, E., De Keijzer, J., Slingerland, E., Van Tilburg, J., Hofsteenge, W., & Haaksma, V. (2016). *Collectieve warmte naar lage temperatuur. Een verkenning van mogelijkheden en routes* (tech. rep.). Ecofys, Greenvis. www.ecofys.com

Velde, B. (2014). Green Clay Minerals. *Treatise on geochemistry* (pp. 351–364). Elsevier. https://doi.org/10.1016/B978-0-08-095975-7.00712-9

Wong, T. E., De Lugt, I., Kuhlmann, G., & Overeem, I. (2007). Geology of the Netherlands - Tertiary. *Geology of the netherlands*.

Wyllie, M. R. J., Gregory, A. R., & Gardner, L. W. (1956). Elastic wave velocities in heterogeneous and porous media. *Geophysics*, *21*(1), 41–70. https://doi.org/10.1190/1.1438217

Zagwijn, W. H. (1989). The Netherlands during the Tertiary and the Quaternary: A case history of Coastal Lowland evolution. *Geologie en Mijnbouw*, *68*, 107–120.

Appendices

Appendix A

ADK-GT-01 cuttings

(a) Cutting samples from 640 to 795 m depth **(b)** Cutting samples from 800 to 955 m depth

Fig. A.1: Washed and sorted cuttings from the ADK-GT-01 well

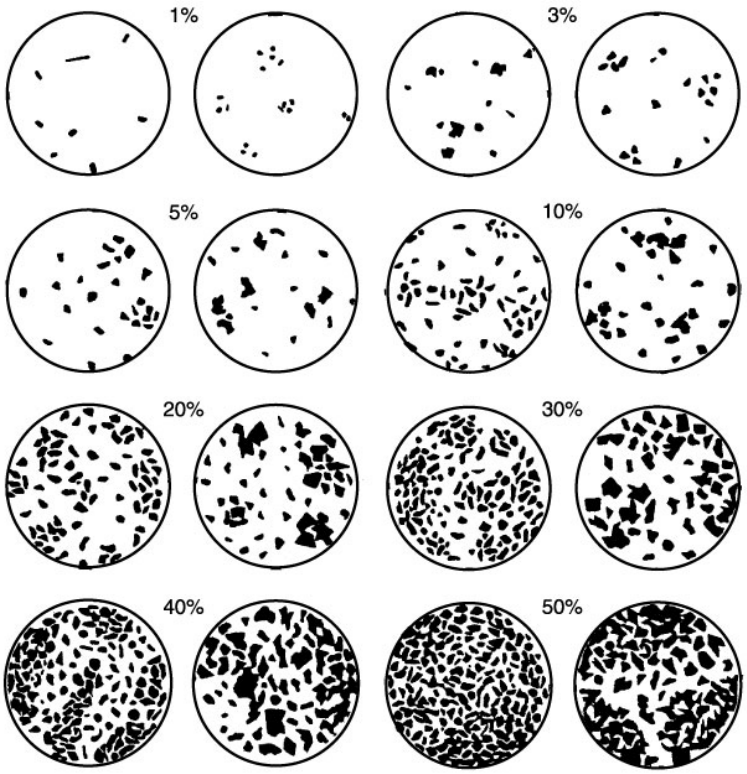

Fig. A.2: Chart for visually estimating the surface percentage of a mineral in a sample (after Terry and Chilingar, 1955)

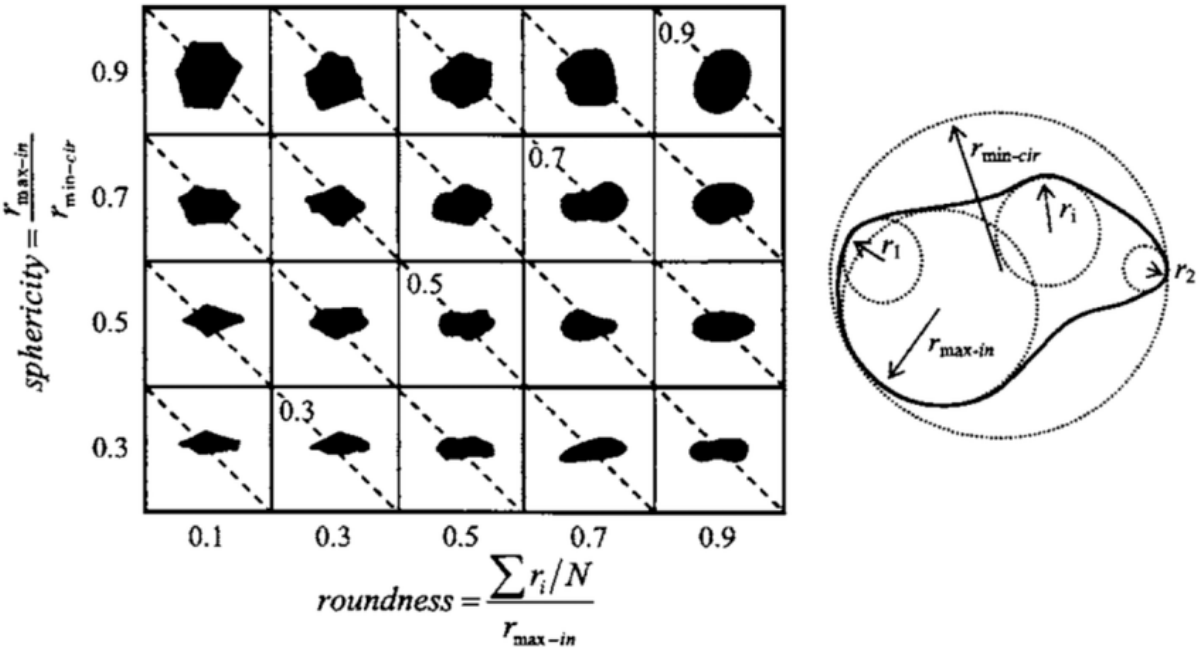

Fig. A.3: Chart for determining the sphericity and roundness of a grain (Mahmoudi et al., 2015)

Appendix B

KRD-01 cuttings

Fig. B.1: Cuttings from the KRD-01 well under the microscope. Scale is roughly 4x enlargement

Appendix C

Restricted or limited areas

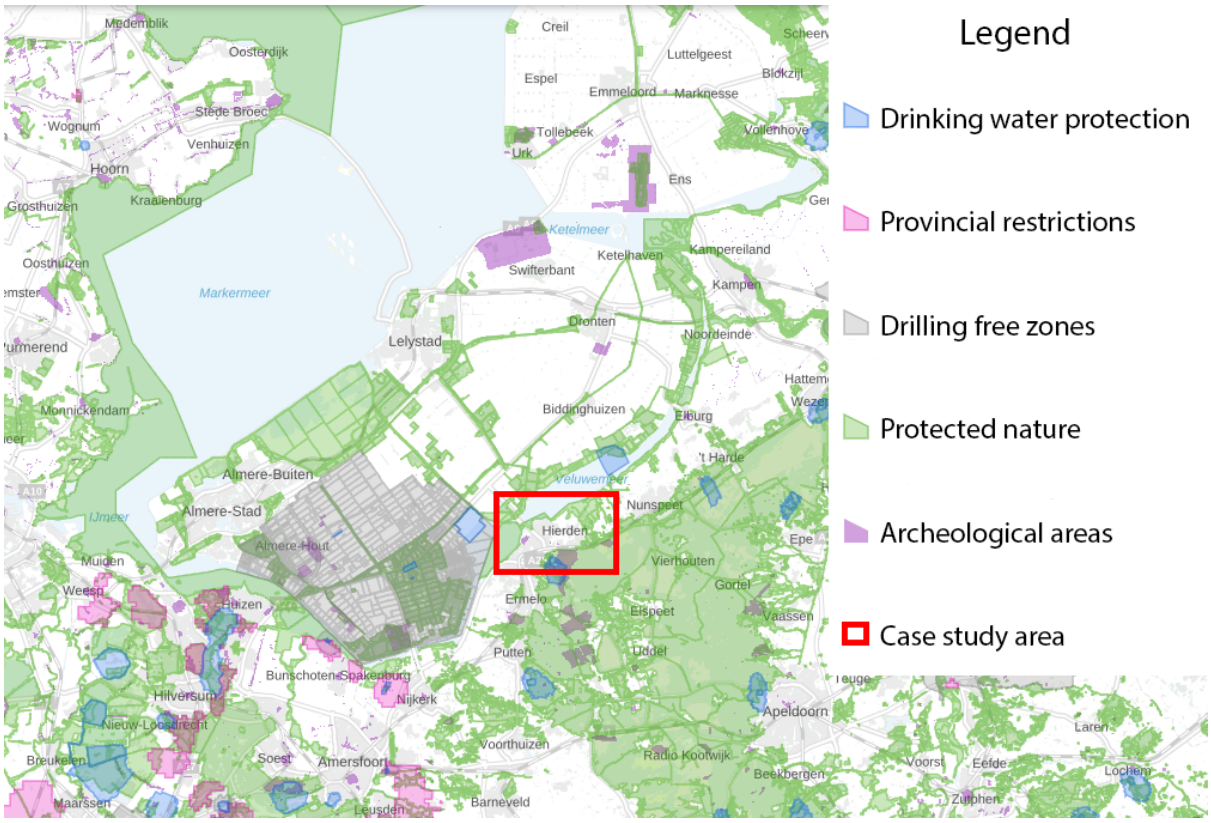

Fig. C.1: Map showing restricted or limited areas for geothermal exploitation. The case study area around Harderwijk is indicated by the red box (RVO, 2022)

Appendix D

Python petrophysics

The python code for the petrophysical analysis can be found on Github, via the following link: Github repository